ISSN 8755-6839

SCIENCE OF **TSUNAMI HAZARDS**

Journal of Tsunami Society International

Volume 31 **Number 3** **2012**

TSUNAMI SOCIETY INTERNATIONAL, 1741 Ala Moana Blvd. #70, Honolulu, HI 96815, USA.

SCIENCE OF TSUNAMI HAZARDS is a CERTIFIED OPEN ACCESS Journal included in the prestigious international academic journal database DOAJ, maintained by the University of Lund in Sweden with the support of the European Union. SCIENCE OF TSUNAMI HAZARDS is also preserved, archived and disseminated by the National Library, The Hague, NETHERLANDS, the Library of Congress, Washington D.C., USA, the Electronic Library of Los Alamos, National Laboratory, New Mexico, USA, the EBSCO Publishing databases and ELSEVIER Publishing in Amsterdam. The vast dissemination gives the journal additional global exposure and readership in 90% of the academic institutions worldwide, including nation-wide access to databases in more than 70 countries.

OBJECTIVE: Tsunami Society International publishes this interdisciplinary journal to increase and disseminate knowledge about tsunamis and their hazards.

DISCLAIMER: Although the articles in SCIENCE OF TSUNAMI HAZARDS have been technically reviewed by peers, Tsunami Society International is not responsible for the veracity of any statement, opinion or consequences.

Submit manuscripts of research papers, notes or letters to the Editor. If a research paper is accepted for publication the author(s) must submit a scan-ready manuscript, a Doc, TeX or a PDF file in the journal format. Issues of the journal are published electronically in PDF format. There is a minimal publication fee for authors who are members of Tsunami Society International for three years and slightly higher for non-members. Tsunami Society International members are notified by e-mail when a new issue is available. Permission to use figures, tables and brief excerpts from this journal in scientific and educational works is granted provided that the source is acknowledged.

Recent and all past journal issues are available at: http://www.TsunamiSociety.org CD-ROMs of past volumes may be purchased by contacting Tsunami Society International at postmaster@tsunamisociety.org Issues of the journal from 1982 thru 2005 are also available in PDF format at the Los Alamos National Laboratory Library http://epubs.lanl.gov/tsunami/

ISSN 8755-6839

SCIENCE OF **TSUNAMI HAZARDS**

Journal of Tsunami Society International

Volume 31 **Number 3** **2012**

TSUNAMI PROPAGATION OVER THE NORTH PACIFIC: DISPERSIVE AND NONDISPERSIVE MODELS

Juan Horrillo,
Texas A&M University at Galveston (TAMUG),

William Knight,
NOAA / West Coast & Alaska Tsunami Warning Center, Palmer, Alaska,

Zygmunt Kowalik,
Institute of Marine Science, University of Alaska Fairbanks, Fairbanks, AK. 99775, USA
(zkowalik@alaska.edu).

ABSTRACT

Hydrostatic (HY) and non-hydrostatic (NHY) tsunami physics is compared by application to the Kuril Island Tsunami (KIT) of November 2006 and the Japan Tsunami (JT) of March 2011. Our purpose is to study the significance of dispersive vs. non-dispersive long waves on global tsunami propagation. A tool which is well suited to revealing tsunami wave transformations is the energy flux. Expressions for dispersive and non-dispersive fluxes have been formulated. This provides an understanding of the role of dispersion in tsunami propagation and dissipation. Separating the pressure field into two parts i.e., HY and NHY shows that dispersive waves extract energy from the main wave, directing the dispersive energy flux away from the wave front. The major result of the application of the energy flux to non-dispersive waves is an enhanced understanding of later tsunami wave train arrivals at distant points – with arrivals sometimes occurring several hours after an initial forerunner wave. Computations show that strong differences between non-dispersive and dispersive waves develop along the length of the main energy beam. This has important consequences for accurate tsunami prediction and warnings.

Key Words: *Japan and Kuril tsunamis, hydrostatic and non-hydrostatic numerical modeling, dispersive and non-dispersive energy flux*

Science of Tsunami Hazards, Vol. 31, No. 3, page 154 (2012)

1. INTRODUCTION

Analysis of the data recorded during the Indian Ocean Tsunami of December 2004 demonstrated that the tsunami waves were noticeably dispersive (Kulikov 2005; Horrillo et al., 2006). Dispersion effects played a significant role in the JT event as described by Saito et al., (2011). In coastal regions, the dispersive wave trains interacted with the leading wave runups, drawdowns, and reflections from shelf and land, strongly modifying the leading waves. Sato (1996) investigated the role of dispersive wave trains generated during the 1993 Hokkaido earthquake around the southern part of Okushiri Island. Comparison of field data to numerical results demonstrated that it is the dispersion of the wave front which caused focusing of the wave energy at the narrow region along the lee side of the island, increasing the tsunami wave height. Ortiz et al., (2001) demonstrated that analytical and numerical solutions without dispersion, when compared to dispersive solutions, over-estimate the leading wave heights of medium and large tsunamis.

Tsunami models are usually based on the shallow water approximation which ignores the effects of wave dispersion. The main difficulty is properly accounting for the properties of shorter length scale dispersive waves. During initial propagation, wave separation into spectral components with different frequencies and amplitudes occurs. Thus the leading wave is followed by a train of waves formed in its tail. To follow the dispersion process, numerical models need to resolve these ever-shortening length scales. Due to model limitations however, only the first few waves are usually resolved. As early as 1974, Mader showed that the shallow water long-wave equations often failed to adequately resolve shorter wavelength tsunamis.

Dispersive effects in tsunami calculations are usually introduced through the Boussinesq equation, see Dunbar et al. (1991) or Madsen et al. (1999). Their numerical solutions require small spatial steps and use either implicit schemes to maintain numerical stability (Shigihara 2004) or explicit schemes which display strong numerical dispersion (Yoon et al. 2007). By applying various generating mechanisms (sea bottom uplift, currents generated by horizontal translation of bathymetric features) and the Boussinesq equation to the Indian Ocean Tsunami of 2004, Rivera (2006) demonstrated that their model accounted for most of the observed wave characteristics. Grilli et al. (2007) used the Boussinesq model FUNWAVE to quantify dispersive effects. This approach has been applied to the JT of 2011, with and without dispersion terms (Kirby et al. 2012).

As second order numerical schemes lead to an error term proportional to the third derivative, thus approximating the dispersive term in the Boussinesq equation, Imamura and Shuto (1989) constructed a numerical scheme which used numerical dispersion to mimic physical dispersion. The method proved to be effective in delineating the basic properties of the 1960 Chilean tsunami (Imamura et al. 1990). This scheme was further applied to propagation of tsunamis over slowly varying topography by Yoon et al. (2007), thus introducing the possibility of accounting for the dispersion of distant tsunamis.

This study aims to reproduce dispersive and non-dispersive tsunami wave propagation dynamics of

the KIT of 2006 and the JT of 2011. First we describe the depth integrated, NHY model, which is based on the assumption that the pressure can be split into a sum of hydrostatic and non-hydrostatic components (Stelling and Zijlema, 2003; Walters, 2005). Secondly, results of several numerical experiments are described for the KIT and JT that reveal the difference between transoceanic propagation with and without dispersion. To further differentiate the physics associated with HY and NHY components, the respective energy fluxes are introduced. Finally, to draw some conclusions about the importance of dispersion, observations are compared to model results at several locations.

2. BASIC EQUATIONS

In order to identify the important aspects of tsunami global propagation the equations of motion and continuity are formulated in spherical polar coordinates. Here λ, φ and R are defined as longitude, latitude and distance from the Earth's center. If the origin of the system is located on the ocean surface, it is more suitable to introduce a vertical coordinate $z=R-Ro$. Here Ro is the radius of Earth and is equal 6370km. If in the equations of motion in the spherical system of coordinates (see Gill, 1982) the pressure is set as a sum of a HY part ph, and a NHY part q as suggested by Stelling and Zijlema (2003),

$$p = \rho g(\zeta - z) + q = p_h + q \tag{1}$$

the following set will describe the dispersive wave propagation

$$\frac{\partial u}{\partial t} + \frac{u}{R_\circ \cos\phi}\frac{\partial u}{\partial \lambda} + \frac{v}{R_\circ}\frac{\partial u}{\partial \phi} + w\frac{\partial u}{\partial z} - (2\Omega + \frac{u}{R_\circ \cos\phi})(v\sin\phi - w\cos\phi) = -\frac{g}{R_\circ \cos\phi}\frac{\partial \zeta}{\partial \lambda} - \frac{1}{\rho R_\circ \cos\phi}\frac{\partial q}{\partial \lambda} + A_\lambda \tag{2}$$

$$\frac{\partial v}{\partial t} + \frac{u}{R_\circ \cos\phi}\frac{\partial v}{\partial \lambda} + \frac{v}{R_\circ}\frac{\partial v}{\partial \phi} + w\frac{\partial v}{\partial z} + \frac{wv}{R_\circ} + (2\Omega + \frac{u}{R_\circ \cos\phi})u\sin\phi = -\frac{g}{R_\circ}\frac{\partial \zeta}{\partial \phi} - \frac{1}{\rho R_\circ}\frac{\partial q}{\partial \phi} + A_\phi \tag{3}$$

$$\frac{\partial w}{\partial t} + \frac{u}{R_\circ \cos\phi}\frac{\partial w}{\partial \lambda} + \frac{v}{R_\circ}\frac{\partial w}{\partial \phi} + w\frac{\partial w}{\partial z} - \frac{v^2}{R_\circ} - (2\Omega + \frac{u}{R_\circ \cos\phi})u\cos\phi = -\frac{1}{\rho}\frac{\partial q}{\partial z} + A_z \tag{4}$$

$$\frac{1}{R_\circ \cos\phi}\frac{\partial u}{\partial \lambda} + \frac{1}{R_\circ \cos\phi}\frac{\partial}{\partial \phi}(v\cos\phi) + \frac{\partial w}{\partial z} = 0 \qquad (5)$$

It is interesting to notice that the *acceleration* along the vertical direction (eq. 4) is generated by the nonhydrostatic component of the pressure (q) which is a function of the vertical coordinate. In the above equations, u is the velocity in the λ (E-W) direction, v denotes the velocity in the φ (N-S) direction, w is the velocity in the z direction, p is the pressure, t is the time, g is the Earth's gravity acceleration $g=981\ cms{-}2$ and ρ is the water density. The Coriolis parameter will be taken as $f=2\Omega\sin\varphi$. It is a function of the Earth's angular velocity $\Omega=7.29\times10{-}5\ s{-}1$ and the latitude φ. $A\lambda$, $A\ \varphi$ and Az are components of the viscous force.

To the above set of equations the kinematic boundary conditions which define the vertical velocity w at the free surface ($z=\zeta$ (x,y,t)) and at the bottom are added. The depth in our consideration will be composed of two variables, thus $Hb=H\ x,y\ -\eta\ x,y,t$. Here $H(x,y)$ is the still water depth and η is the bottom deformation. The change in bottom shape may be introduced by bottom uplift or downdrop due to an earthquake or submarine landslide.

The total depth is defined as $D=H+\zeta-\eta$. The vertical velocity at the free surface reads,

$$w_\zeta = w_s = \frac{D\zeta}{Dt} = \frac{\partial \zeta}{\partial t} + \frac{u_s}{R_\circ \cos\phi}\frac{\partial \zeta}{\partial \lambda} + \frac{v_s}{R_\circ}\frac{\partial \zeta}{\partial \phi} \qquad (6)$$

and at the bottom,

$$w_{z=-H_b} = w_b = \frac{D(-H_b)}{Dt} = \frac{\partial \eta}{\partial t} - \frac{u_b}{R_\circ \cos\phi}\frac{\partial H}{\partial \lambda} - \frac{v_b}{R_\circ}\frac{\partial H}{\partial \phi} \qquad (7)$$

Assuming that the dispersive waves are long enough, we can still use the long wave approximation and vertically integrate the above system of equations. The vertically averaged equation of continuity is obtained by integrating eq. (5) from the free surface to the bottom and taking into account eqs. (6) and (7).

$$\frac{\partial \zeta}{\partial t} - \frac{\partial \eta}{\partial t} + \frac{1}{R_\circ \cos\phi}\frac{\partial U D}{\partial \lambda} + \frac{1}{R_\circ \cos\phi}\frac{\partial}{\partial \phi}(DV\cos\phi) = 0 \qquad (8)$$

Equations of motion along the horizontal directions (eqs. 2 and 3) can be averaged as well,

$$\frac{\partial U}{\partial t}+\frac{U}{R_\circ\cos\phi}\frac{\partial U}{\partial\lambda}+\frac{V}{R_\circ}\frac{\partial U}{\partial\phi}-(2\Omega+\frac{U}{R_\circ\cos\phi})V\sin\phi=$$

$$-\frac{g}{R_\circ\cos\phi}\frac{\partial\zeta}{\partial\lambda}-\frac{1}{D\rho R_\circ\cos\phi}\int_{-H_b}^{\zeta}\frac{\partial q}{\partial\lambda}dz-\frac{\tau_\lambda^b}{\rho D} \qquad (9)$$

$$\frac{\partial V}{\partial t}+\frac{U}{R_\circ\cos\phi}\frac{\partial V}{\partial\lambda}+\frac{V}{R_\circ}\frac{\partial V}{\partial\phi}+(2\Omega+\frac{U}{R_\circ\cos\phi})U\sin\phi=-\frac{g}{R_\circ}\frac{\partial\zeta}{\partial\phi}-\frac{1}{D\rho R_\circ}\int_{-H_b}^{\zeta}\frac{\partial q}{\partial\phi}dz-\frac{\tau_\phi^b}{\rho D} \qquad (10)$$

In the above equations, U is the vertically averaged velocity in the λ (E-W) direction, V denotes the vertically averaged velocity in the φ (N-S) direction. It is important to note that the bottom vertical velocity for a time dependent bottom profile differs from the case of constant bottom profile. In the latter case the expression for the vertical velocity at the bottom simplifies to

$$w_{-H_b}=w_b=-\frac{u_b}{R_\circ\cos\phi}\frac{\partial H}{\partial\lambda}-\frac{v_b}{R_\circ}\frac{\partial H}{\partial\phi} \qquad (7a)$$

This expression when introduced into the equation of continuity (eq. 8) yields,

$$\frac{\partial\zeta}{\partial t}+\frac{1}{R_\circ\cos\phi}\frac{\partial}{\partial\lambda}\int_{-H}^{\zeta}udz+\frac{1}{R_\circ\cos\phi}\frac{\partial}{\partial\phi}\int_{-H}^{\zeta}(v\cos\phi)dz=0 \qquad (8a)$$

The equation of motion along the vertical direction (eq. 4) will require the strongest simplification so that the vertical integration can be applied. First, it can be written in the following transparent form

$$\frac{\partial w}{\partial t}+w_n=-\frac{1}{\rho}\frac{\partial q}{\partial z}+A_z \qquad (4a)$$

We simplify the above equation by assuming the vertical velocity is linear in z (Walters, 2005; Proudman, 1953) and the nonlinear wn and viscous Az terms can be neglected. Integrating along the vertical direction we arrive at

$$D\frac{\partial}{\partial t}[\frac{w_s+w_b}{2}]=-\frac{q_s-q_b}{\rho}$$

$$\frac{\partial}{\partial t}[\frac{w_s+w_b}{2}]=-\frac{q_s-q_b}{\rho D}=\frac{q_b}{\rho D} \qquad (11)$$

Due to the linear variation the vertical velocity is taken to be the average of its value at the free surface *ws* and at the sea bottom *w b*. Had the actual nonlinear profile of velocity been retained, the complicated multilayered flow would have been considered.

2. AN APPROACH TO SOLUTION

In order to identify important steps in the construction of a general numerical code we shall simplify problem to the *x-z* crossection. In the vertically integrated equation of motion (eq. 9) the unknown term is related to the NHY pressure (*q*),

$$-\frac{1}{D\rho R_\circ \cos\phi}\int_{-H_b}^{\zeta}\frac{\partial q}{\partial\lambda}dz$$

The expression under integral can be rewritten as

$$\frac{\partial}{\partial\lambda}\int_{-H_b}^{\zeta} q dz = \int_{-H_b}^{\zeta}\frac{\partial q}{\partial\lambda}dz + q_s\frac{\partial\zeta}{\partial\lambda} - q_b\frac{\partial(-H_b)}{\partial\lambda}$$

The integral at the left-hand-side is approximated as

$$\frac{\partial}{\partial\lambda}\int_{-H_b}^{\zeta} q dz \approx \frac{\partial}{\partial\lambda}[0.5D(q_s+q_b)]$$

Since the total pressure vanishes at the free surface, therefore *qs* =0, and we can write,

$$\int_{-H_b}^{\zeta}\frac{\partial q}{\partial\lambda}dz = 0.5\frac{\partial}{\partial\lambda}[Dq_b] - q_b\frac{\partial(H_b)}{\partial\lambda} =$$

$$0.5q_b\frac{\partial}{\partial\lambda}(\zeta+\eta-H) + 0.5D\frac{\partial q_b}{\partial\lambda} \qquad (12)$$

Introducing eq. (12) into eq. (9) results in the following:

$$\frac{\partial U}{\partial t} + \frac{U}{R_\circ\cos\phi}\frac{\partial U}{\partial\lambda} = -\frac{g}{R_\circ\cos\phi}\frac{\partial\zeta}{\partial\lambda} - \frac{1}{D\rho R_\circ\cos\phi}[0.5q_b\frac{\partial}{\partial\lambda}(\zeta+\eta-H)+0.5D\frac{\partial q_b}{\partial\lambda}] - \frac{\tau_\lambda^b}{\rho D} \quad (13)$$

As motion is imparted by both hydrostatic and non-hydrostatic forcing, the equation of motion is split

into two parts. Provisional horizontal velocities are obtained with the hydrostatic pressure alone. The final velocities at the next time step are obtained by advancing the provisional values with *q b*. To achieve numerical solution while stepping in time with the time step *T* we split solution of the above equation into two subsets to be solved on the *T/2* time step as,

$$\frac{1}{2}\frac{\partial U}{\partial t} + \frac{U}{R_\circ \cos\phi}\frac{\partial U}{\partial \lambda} = -\frac{g}{R_\circ \cos\phi}\frac{\partial \zeta}{\partial \lambda} - \frac{\tau_\lambda^b}{\rho D} \qquad (14a)$$

$$\frac{1}{2}\frac{\partial U}{\partial t} = -\frac{1}{D\rho R_\circ \cos\phi}[0.5 q_b \frac{\partial}{\partial \lambda}(\zeta + \eta - H) + 0.5 D \frac{\partial q_b}{\partial \lambda}] \qquad (14b)$$

Or using time stepping index m

$$\frac{1}{2}\frac{(U^{m+1/2} - U^m)}{T/2} + \frac{U}{R_\circ \cos\phi}\frac{\partial U}{\partial \lambda} = -\frac{g}{R_\circ \cos\phi}\frac{\partial \zeta}{\partial \lambda} - \frac{\tau_\lambda^b}{\rho D} \qquad (15a)$$

$$\frac{1}{2}\frac{(U^{m+1} - U^{m+1/2})}{T/2} = -\frac{1}{D\rho R_\circ \cos\phi}[0.5 q_b \frac{\partial}{\partial \lambda}(\zeta + \eta - H) + 0.5 D \frac{\partial q_b}{\partial \lambda}] \qquad (15b)$$

The solution of eq (15a) is usually advanced in time by the two-time-level numerical scheme (Kowalik and Murty, 1993; Imamura, 1996). Eq. (15a) is easily solved based on the old values (at the time step *m*) of the velocity and sea level. The new (provisional) velocity *U(m+ 12)* is introduced into (eq. 15b) to further advance the solution. Unfortunately, the solution of the second equation cannot proceed in time until the new value of *qb* is found. For this purpose we combine the equation of motion along the vertical direction (eq.11), the equation of continuity and (eq. 15b). Consider again equation of continuity (eq.5), which upon vertical integration gives,

$$\frac{1}{R_\circ \cos\phi}\frac{\partial U^{m+1}}{\partial \lambda} + \frac{(w_s^{m+1} - w_b^{m+1})}{D} = 0 \qquad (16)$$

Introducing *Um+1* from eq.(15b) into the above equation, *wsm+1* from eq.(11) and *wbm+1* from eq.(7a) we arrive at equation for the unknown pressure *qb*. The detail of numerical solution for this problem is given in Yamazaki et al.,(2008).

4. MAXIMUM AMPLITUDE

Figure 1 describes the bathymetry of the North Pacific used in our computation (based on work by British Oceanographic Data Centre, 2003). Because numerical results will be compared to sea level data collected by Pacific DART buoys, several of these buoy locations are selected. The tsunami signal will be analyzed in a few points located either in the main energy lobe of the tsunami or in the location with the strong dispersive signal.

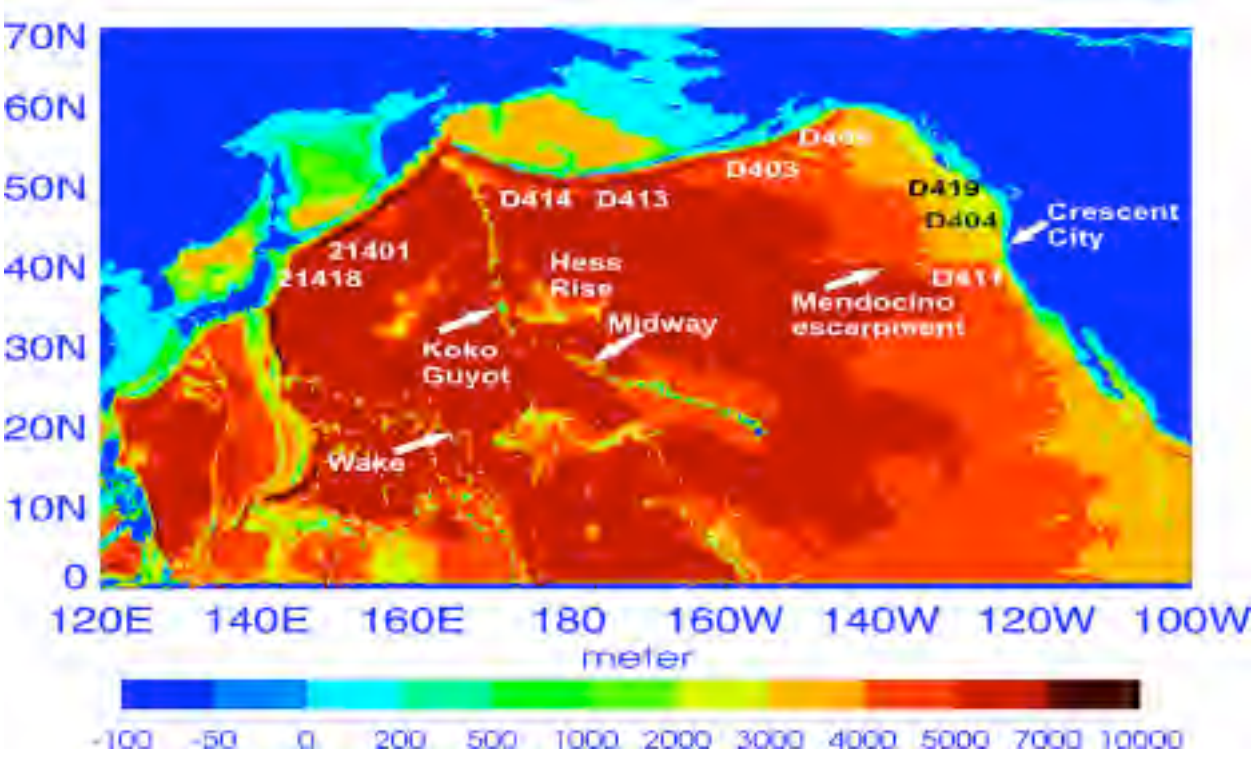

Figure 1. One-minute resolution bathymetry based on the GEBCO Atlas (British Oceanographic Data Centre, 2003). Shown are DART buoys used in comparison with model and some important bathymetric features.

Bathymetric features important in scattering and refocusing tsunami signal are also shown in Figure 1. Primary sources for the tsunami scattering are interactions with Koko Guyot and Hess Rise located at the southern flank of the Emperor Seamount Chain. The regions of the amplified energy flux are usually elongated ridges and fracture zones where tsunami wave energy is concentrated owing to refraction over stepwise topography. An example of such an interaction is the strong tsunami scattering towards Northern California by the Hess Rise and Koko Guyot and later amplified by the Mendocino Escarpment during its approach towards Crescent City (Kowalik et al., 2008). The source for the KIT is described in Kowalik et al. (2008). The JT source is arrived at through the use of Okada's (1985) formulae using fault parameters in Table 1.

Table 1. Fault parameters for Japan earthquake of 11 March 2011.

Fault Parameter	Parameter value
Strike	193°
Dip	19°
Slip	90°
Length	250 km
Width	120 km
Depth	15 km
SW corner Latitude	34.33N
SW corner Longitude	139.33E
Moment	3.0×10^{29}dyne-cm
Rigidity	4.2×10^{11}dyne cm^{-2}

Model computations using the above source were made for 10 hrs of propagation, allowing the tsunami signal to travel over the entire North Pacific. During this computation the maximum tsunami sea surface height (ssh) in every grid point was recorded. The wave height here is defined as positive sea-level change from the mean sea level to the wave crest. The plot of maximum ssh in the North Pacific domain is shown in Fig. 2 for the KIT event and in Fig. 3 for the JT event.

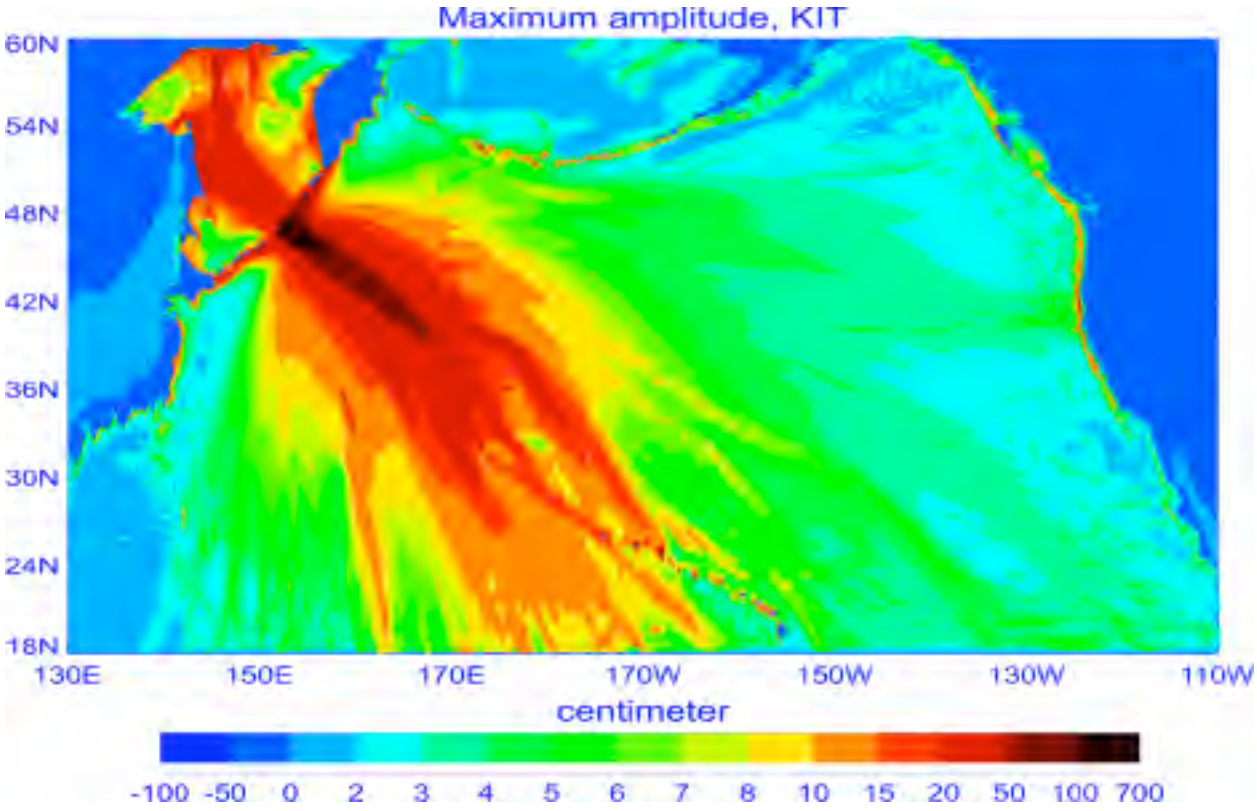

Figure 2. North Pacific, maximum modeled sea surface height, Kurile Island Tsunami, 2006.

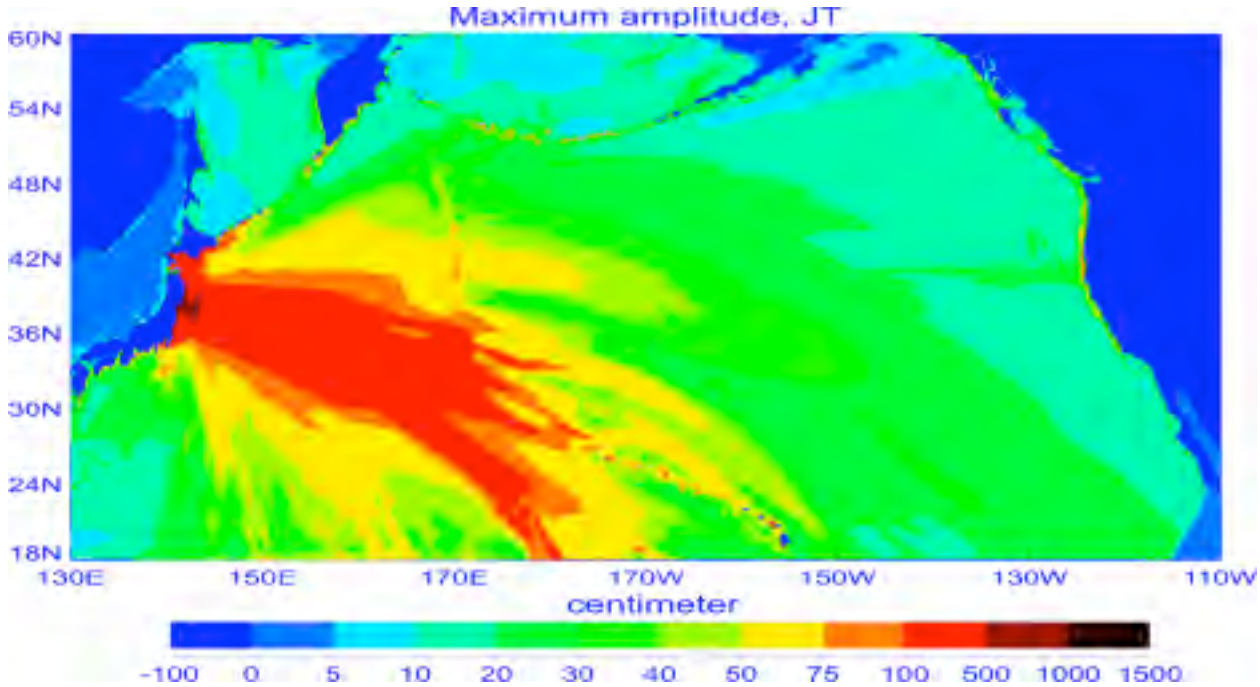

Figure 3. North Pacific, maximum modeled sea surface height, Japan Tsunami 2011.

Computations presented in these figures were carried out using the HY model, therefore NHY pressure q and vertical velocity w are set to zero, and the problem is solved by the set of explicit equations (Kowalik et al., 2005). The signals generated by the source in Kurile Islands Chain and in proximity to Japan are traveling as a positive wave toward the southeast Pacific. Some of the tsunami energy propagates in a finger-like pattern, a product of wave refraction and focusing around islands, seamounts, passages, and chain systems. Closer examination shows that although the signals are dominated by directionality arising from the elongated KIT and JT sources, they also show strong local maxima resulting from interactions with bathymetry. The details of such interactions have been clearly shown by Kowalik et al. (2008). The finger-like patterns of the energy lobes in Figures 2 and 3 can be easily associated with major bathymetric features. The energy lobe resulted from interaction with the Emperor Seamount Chain and especially with two bathymetric features namely Koko Guyot and Hess Rise located at the southern tip of the chain is redirecting energy towards the Crescent City for both KIT and JT events.

The addition of the dispersive wave component to the solution produces a distribution of maximum ssh quite similar to the one from Figures 2 and 3, although the area of the maximum seems to be smaller than that for the non-dispersive propagation. To compare the results for the nondispersive and dispersive wave propagation (notice that we compare only positive ssh) the maximum ssh for the dispersive waves is subtracted from the maximum ssh for the non-dispersive waves. The differences are given in Fig. 4 and Fig. 5. Both figures show a repeatable pattern: in the main energy lobe the hydrostatic solution dominates strongly while at the side lobes, elongated domains dominated by dispersive waves are generated.

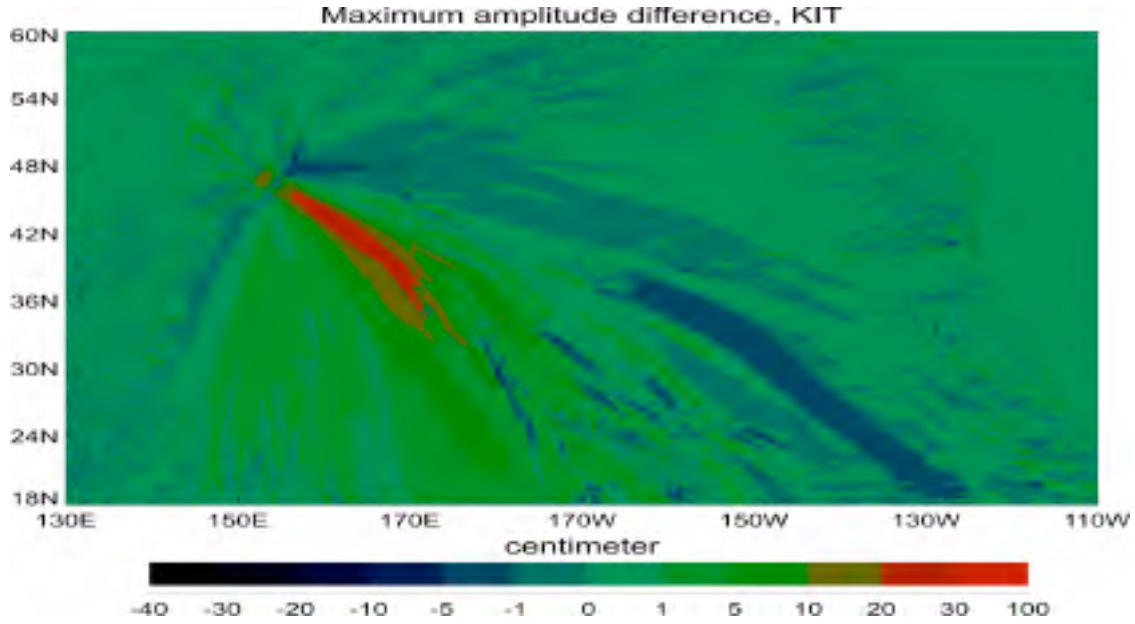

Figure 4. Difference between nondispersive and dispersive maximum ssh, for KIT. Red-green: the nondispersive waves dominate; blue: the dispersive waves dominate.

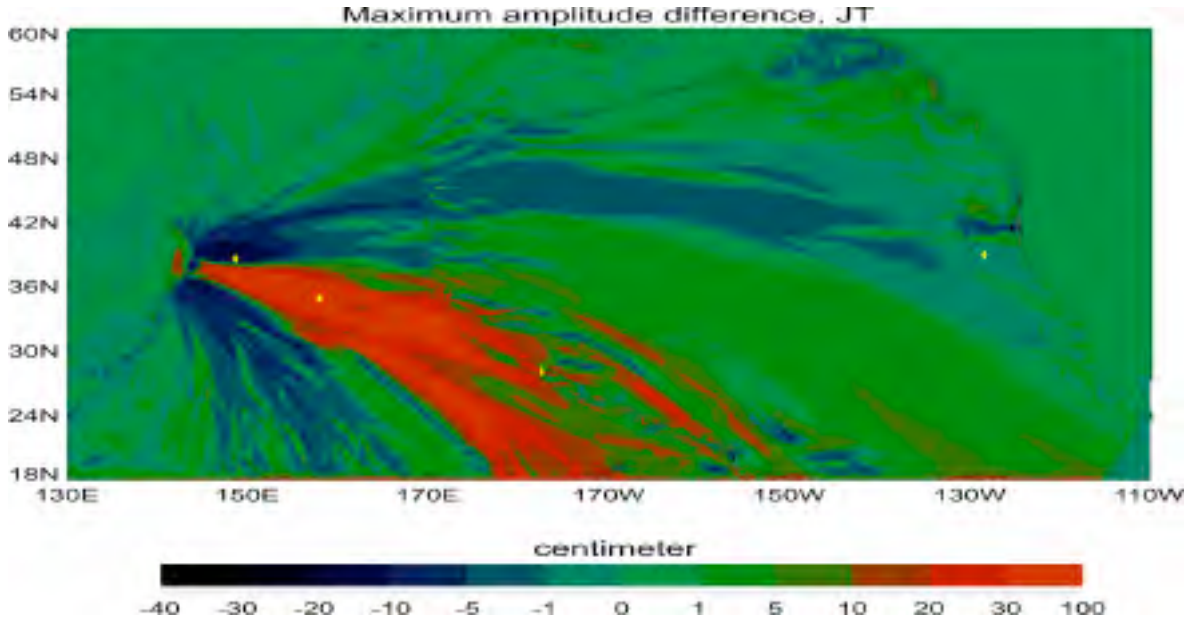

Figure 5. Difference between non-dispersive and dispersive maximum ssh, for JT. Red-green: the nondispersive waves dominate; blue: the dispersive waves dominate. Yellow plus markers indicate: Dart Buoy 21418 (148.694 E,38.711 N), numerical gauge located in main lobe of energy (158.00E, 35.00N), Midway Island tide gauge(177.36 W, 28.212 N) and Dart Buoy 46411 (127 W, 39.94 N).

This pattern confirms previous computations by Kirby et al. (2012) using Boussinesq wave model for propagation of the weakly dispersive surface gravity waves. While comparisons of the dispersive and non-dispersive computations for the same source suggest that the dispersive wave amplitude is typically smaller than the non-dispersive amplitude (Mader, 2004; Horrillo et al, 2006), the above results suggest that over large regions, the opposite situation may occur. The strongest differences for both KIT and JT occur along the main energy lobe where the largest ssh occurs. According to eq. 15b the generation of the dispersive component is connected to the areas where either strong gradients of depth or sea level occur. It points to the regions of the maximum ssh in Figs. 2 and 3 as the area where the strong dispersive effect are generated as depicted in Figs. 4 and 5.

5. ENERGY FLUX

We have used energy fluxes to elucidate the amplification processes during the KIT propagation towards Crescent City (Kowalik et al., 2008). The energy fluxes have been also applied for identification of the sources of the high amplitude secondary signals and to define time delays between initial tsunami wave and secondary signals. Two types of energy fluxes directed in the horizontal plane will be used in the present investigations (see Appendix).

The components of the energy flux vector for the hydrostatic vertically integrated equations

$$\vec{e}_{f,h} = \{UD[\rho(U^2 + V^2)/2 + \rho g\zeta]; DV[\rho(U^2 + V^2)/2 + \rho g\zeta]\} \qquad (17a)$$

and the components of the energy flux generated by the non-hydrostatic pressure q

$$\vec{e}_{f,nh} = \{UDq_b/2; DVq_b/2\} \qquad (17b)$$

We start by plotting distribution of energy flux vectors for the KIT in the North Pacific for the region extending from the Okhotsk Sea to the Emperor Seamount Chain (Fig. 6). The energy flux vectors have the same length but the colors indicate intensity: the red indicates highest, the green is intermediate and the blue is the lowest intensity. The plot captures energy flux vectors at the time of 84 min from the tsunami onset. The upper panel defines the energy flux due to the non-dispersive waves (eq. 17a) and the lower panel identifies the energy flux pattern for the dispersive waves (eq. 17b). The practical application of the energy flux is related to the fact that it delineates the pathways that couple tsunami energy sources with distant location. As can be gleaned from Fig 6 (upper and lower panel) only in one respect are dispersive and non-dispersive energy fluxes similar, namely both energy vector fields at the tsunami wavefront point in the direction of propagation.

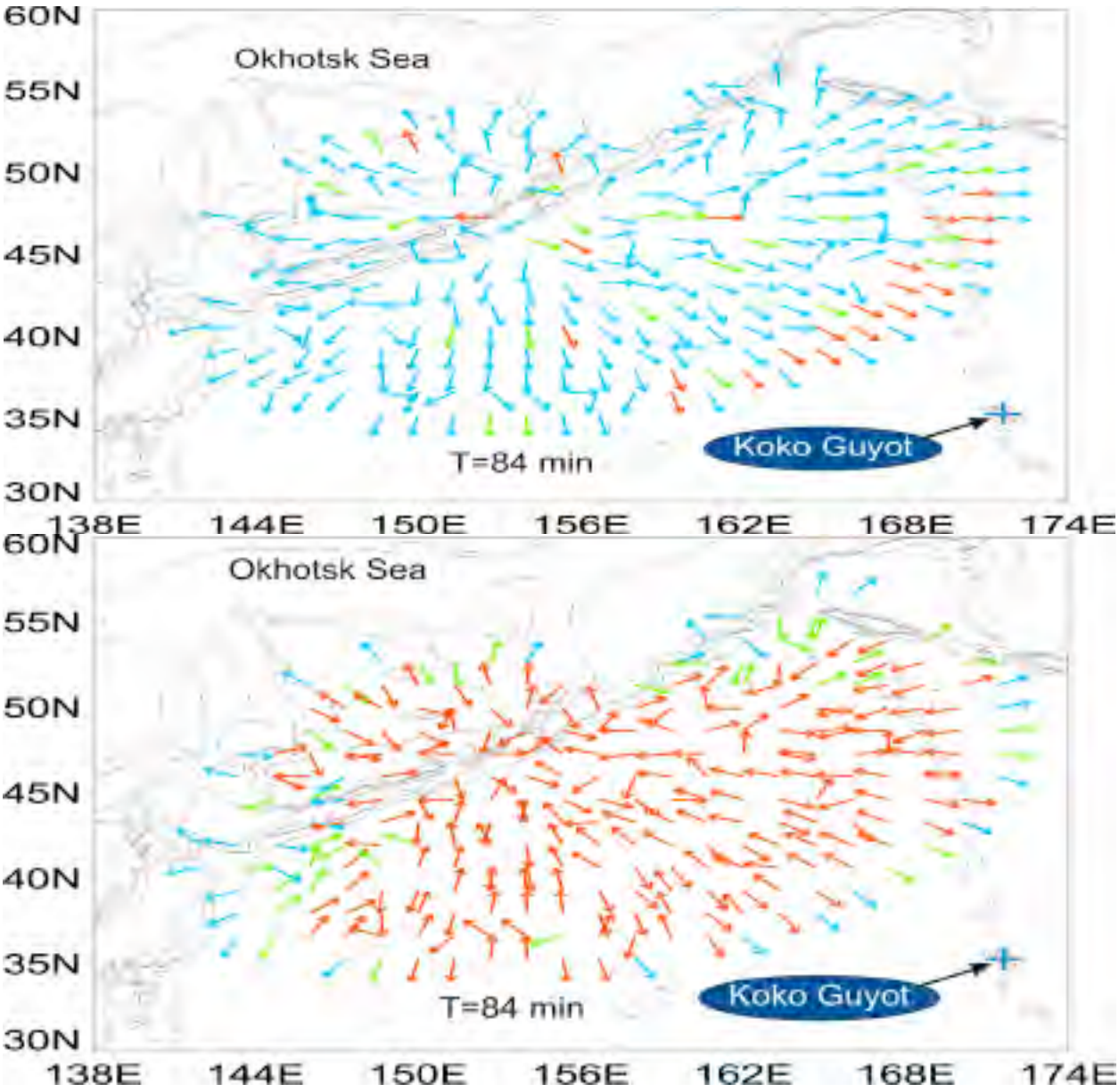

Figure 6. Energy flux vectors over the North-East Pacific at 84 min from KIT onset. Upper panel: nondispersive energy flux; Lower panel dispersive energy flux. Colors define intensity, blue - lowest, green- intermediate, red - highest.

The lower panel of Fig. 6 indicates that as soon as the initial tsunami signal begins to grow at a distant location, dispersive energy is generated and re-directed from the wave front back into the propagation domain. Secondary waves propagating within the domain will receive this additional energy. This "strange" behavior is easily understood if we notice that the non-hydrostatic pressure (q) in the energy

flux eq. 17b is a function of the vertical velocity. According to eq. 11 the pressure (q) is a function of the vertical velocity at the surface and at the bottom.

The generation of surface velocity starts when the tsunami impinges on the new location, increasing the sea level amplitude and causing strong vertical acceleration. Consequently, dispersive waves will be generated and their energy amplified. We can conclude that the largest tsunami wave amplitude (which usually is located just behind the wave front) is the main energy source for the non-dispersive energy flux.

The lower panel in Fig. 6 shows that the energy flux of the dispersive wave is not uniform, although, generally the flow is directed backward towards the Kurile Islands where the tsunami originated. The energy flux vectors depict small-scale variations due to either bottom velocity or to diffraction. A very different pattern of energy flux is displayed for the non-dispersive waves in the upper panel, Figure 6. The energy flux is directed away from the source function (located in the Kurile Islands) with distinctive regions of higher and lower energy fluxes.

As the above analysis identifies the sources of the non-dispersive and dispersive energy fluxes, the next step is to use the fluxes to describe the energy pathways. The source for the non-dispersive waves is well defined in space; on the other hand the source area of the dispersive waves increases at every time step while the intensity of the generation rapidly diminishes.

To further study the KIT and JT development in time the energy flux contours can be used. The contours are given by

$$E_h = \sqrt{e_{f,hx}^2 + e_{f,hy}^2} \quad \text{for eq. 17a} \quad \text{and} \quad E_{nh} = \sqrt{e_{f,nhx}^2 + e_{f,nhy}^2} \quad \text{for the eq. 17b} \quad (18)$$

The energy flux contours for the non-dispersive wave are given in Fig. 7. The well-defined energy flux contours at the front display two closely spaced maxima which are related to the initial wave's positive and negative amplitude. These initial two maxima can be easily tracked (Fig. 7). Moreover when the initial wave impinges on an important bathymetric feature (e.g. Koko Guyot) it goes through complicated processes of tsunami energy scattering and trapping.

To identify the Koko Guyot as an important bathymetric feature, we plot in Fig. 7 the energy flux contours immediately following passage of the main energy lobe past Koko, during KIT (upper panel) and during JT (lower panel).

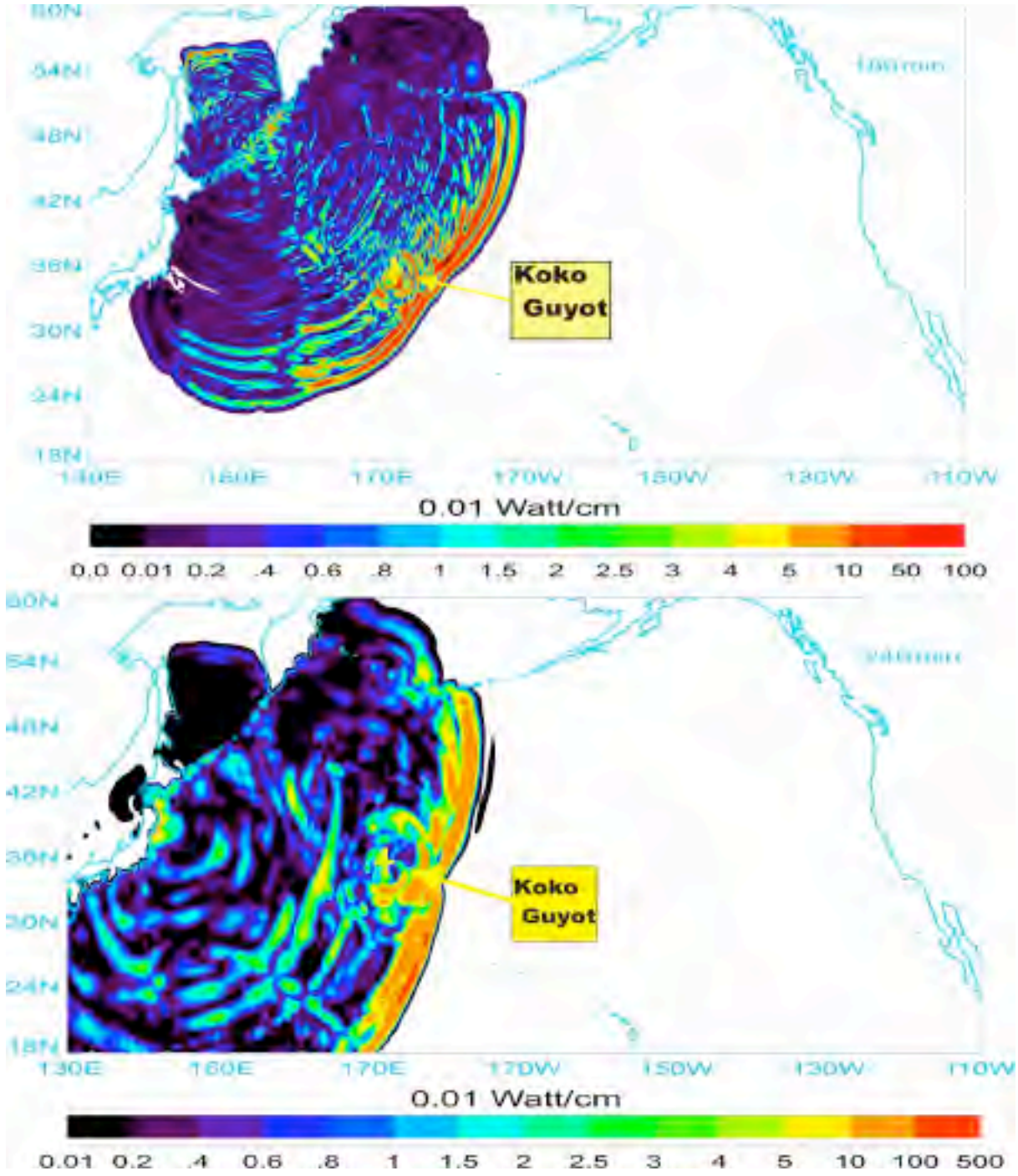

Figure 7. Energy flux contours for the non-dispersive waves, Kurile Island Tsunami (upper panel) and Japan Tsunami (lower panel). The signals of higher energy have been identified as scattered from the Koko Guyot, the Emperor Seamounts and Hess Rise. Yellow plus marker points to location of the Koko Guyot seamount.

Further time history for the KIT as discussed by Kowalik et al. (2008) shows that the wave scattered from the Koko Guyot was responsible for the maximum amplitude at Crescent City which occurred about two hours after the initial wave arrival. Very similar time-history took place during JT. In both events additional tsunami energy enhancement was caused by the Mendocino Escarpment and the local offshore bathymetry (Horrillo at al., 2008).

In conclusion, energy fluxes provide a tool which allows one to not only track the primary sources of energy, but to identify sources of the high amplitude secondary signals and to define the time delay between initial tsunami wave and secondary signals. Computational experiments using energy flux clearly identify the bathymetric features important in scattering tsunami energy towards distant locations. This is possible because the energy flux clearly connects specific bathymetric features such as Koko Guyot and the Hess Rise to impact locations thousands of kilometers away. Although this report is focused on the US West Coast, Koshimura et al. (2008) showed that the KIT energy was similarly scattered westward from the Emperor Seamounts, strongly affecting tsunami energy along Japan's Pacific coast.

6. TIME SERIES

To demonstrate the different behavior of the dispersive and nondispersive wave we consider a few time series of the sea level computed and recorded during JT event. The first point (Fig. 5, yellow cross) denotes location of the Dart Buoy 21418 (148.694E, 38.711N).

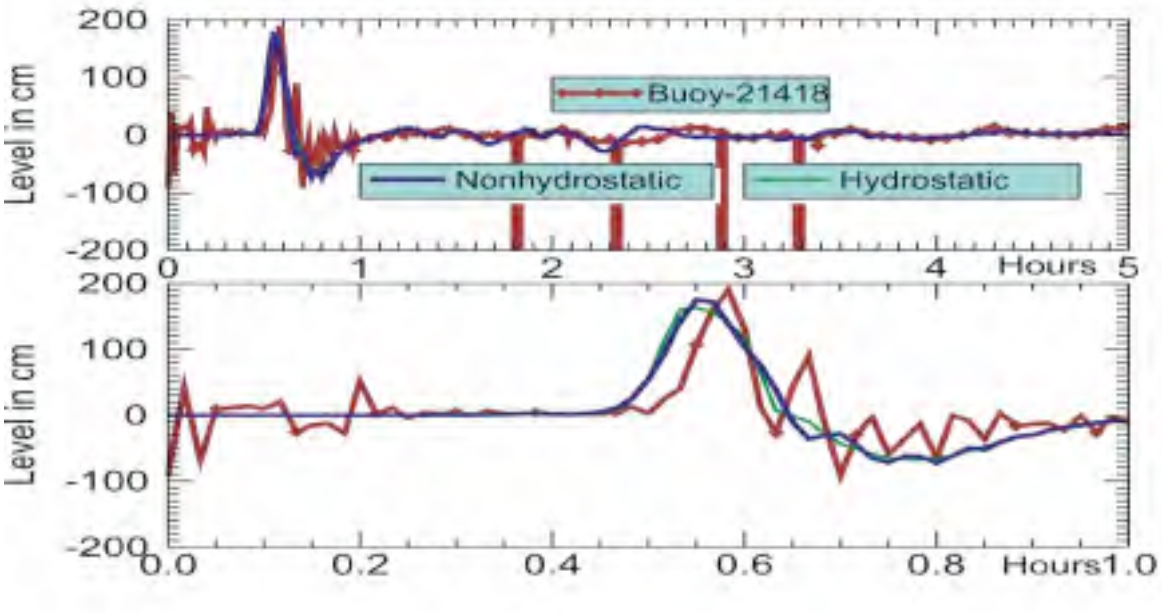

Figure 8. Sea level during Japan Tsunami of 11 March 2011. Red color denotes data recorded by DART buoy; blue denotes the dispersive computation and green non-dispersive. Time is given from the tsunami onset. Lower panel shows detail of the tsunami wave front.

The comparison of the tsunami signal recorded by DART buoys and calculated by the HY and NHY models show that both models reproduced the observed sea level variations. The signal zoom up given in the lower panel of Fig. 8 shows that dispersive wave is dominating and is slightly closer to observations.

The second point chosen for comparison is located in the main lobe of energy (158.00E, 35.00N).

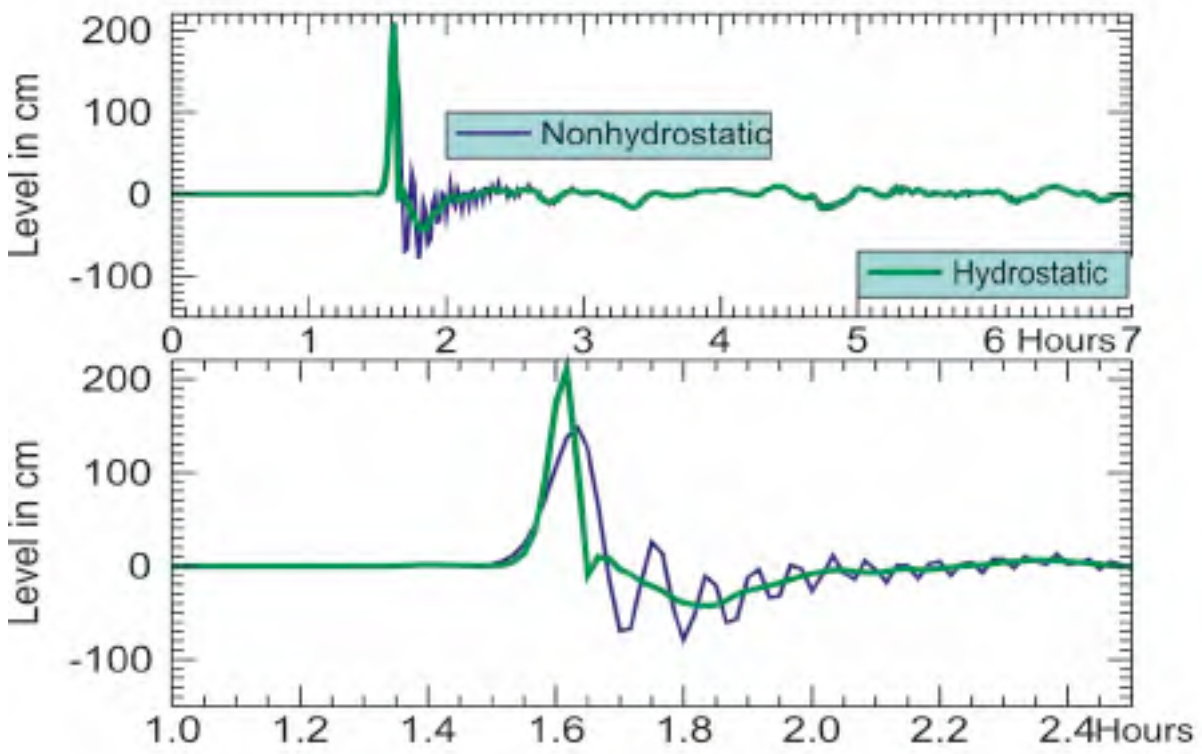

Figure 9. Sea level during the Japan Tsunami of 11 March 2011, calculated inside the main energy lobe (158.0E, 35.0N). Blue line denotes the dispersive computation and green nondispersive. Time is given from the tsunami onset. Lower panel shows detail of the tsunami wave front.

The dispersive versus non-dispersive computations given in Fig. 9 show distinctive features of tsunami wave: A) The amplitude of the first half- cycle for the long wave non-linear, non-dispersive model is much higher than for the dispersive wave (the difference is more than 60 cm); B) The dispersive wave travels slower and C) The train of dispersive waves develops behind the main wave. This train depicts both diminishing amplitude and shorter period. The latter feature, i.e. generation of the short period waves brings into focus the limitations of numerical modeling related to the simulation of short spatial and temporal scales. Simply speaking as the model does not resolve short length scales; the computation develops large numerical errors.

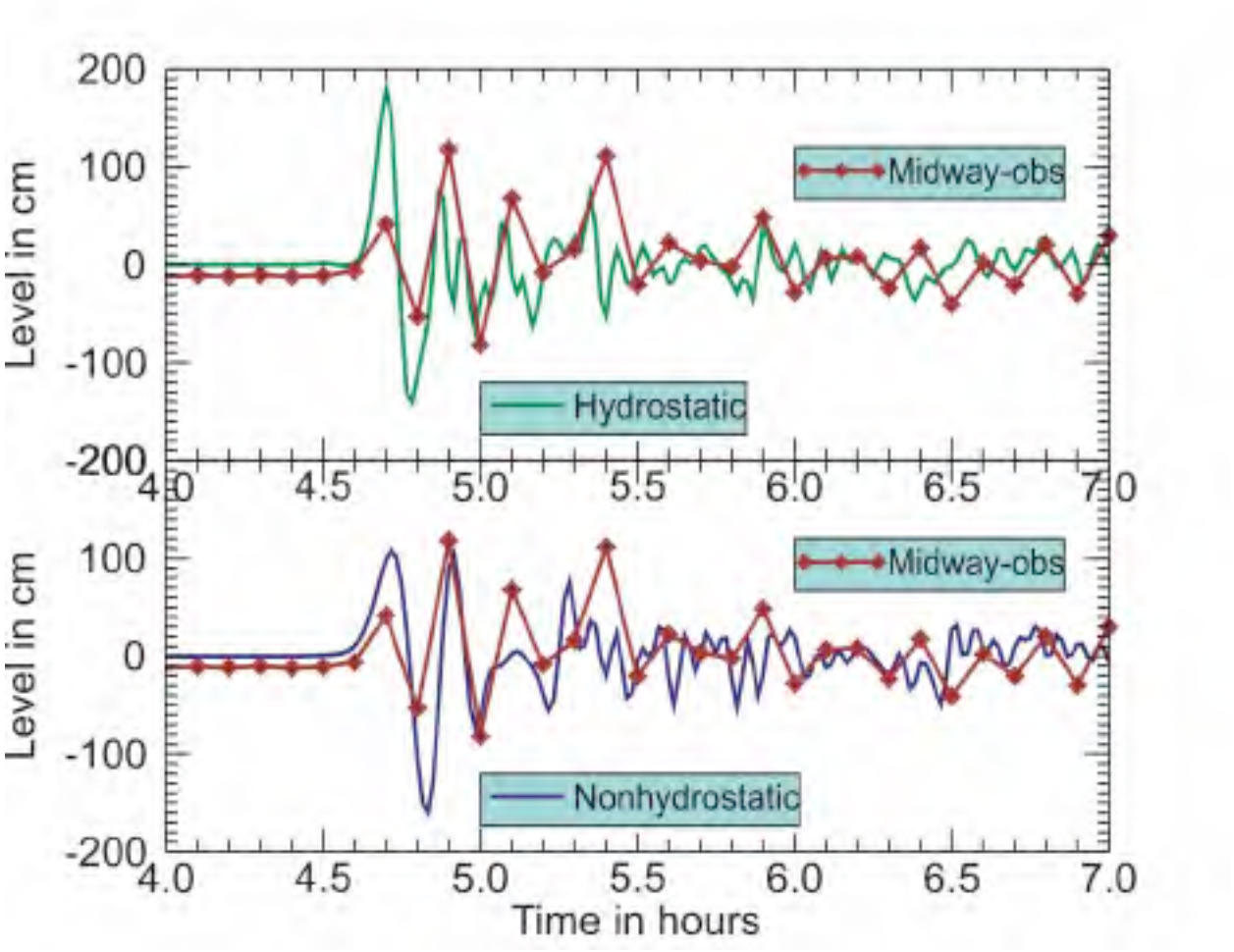

Figure 10. Sea level during Japan Tsunami of 11 March 2011 at Midway Island. Red color shows observation, blue denotes the dispersive and green non-dispersive computations. Time is given from the tsunami onset.

In Fig. 10 the sea level observations made at the Midway Island (177.36 W, 28.212 N) are compared against the nondispersive model (upper panel) and dispersive model (lower panel). Comparison shows that both models reproduce the first recorded waves rather poorly. The dispersive model did the better job when compared with nondispersive model by diminishing the first wave arrival by 70 cm.

Next we consider recording of the sea surface oscillations at the Dart Buoy 46411 (127 W, 39.94 N) located at the far field from tsunami generation function. Comparisons given in Fig. 11 show that both numerical models reproduce well the first waves. The differences between the dispersive and nondispersive models are small. We can conclude that at least for the first waves the dispersion does not change the tsunami wave in this region.

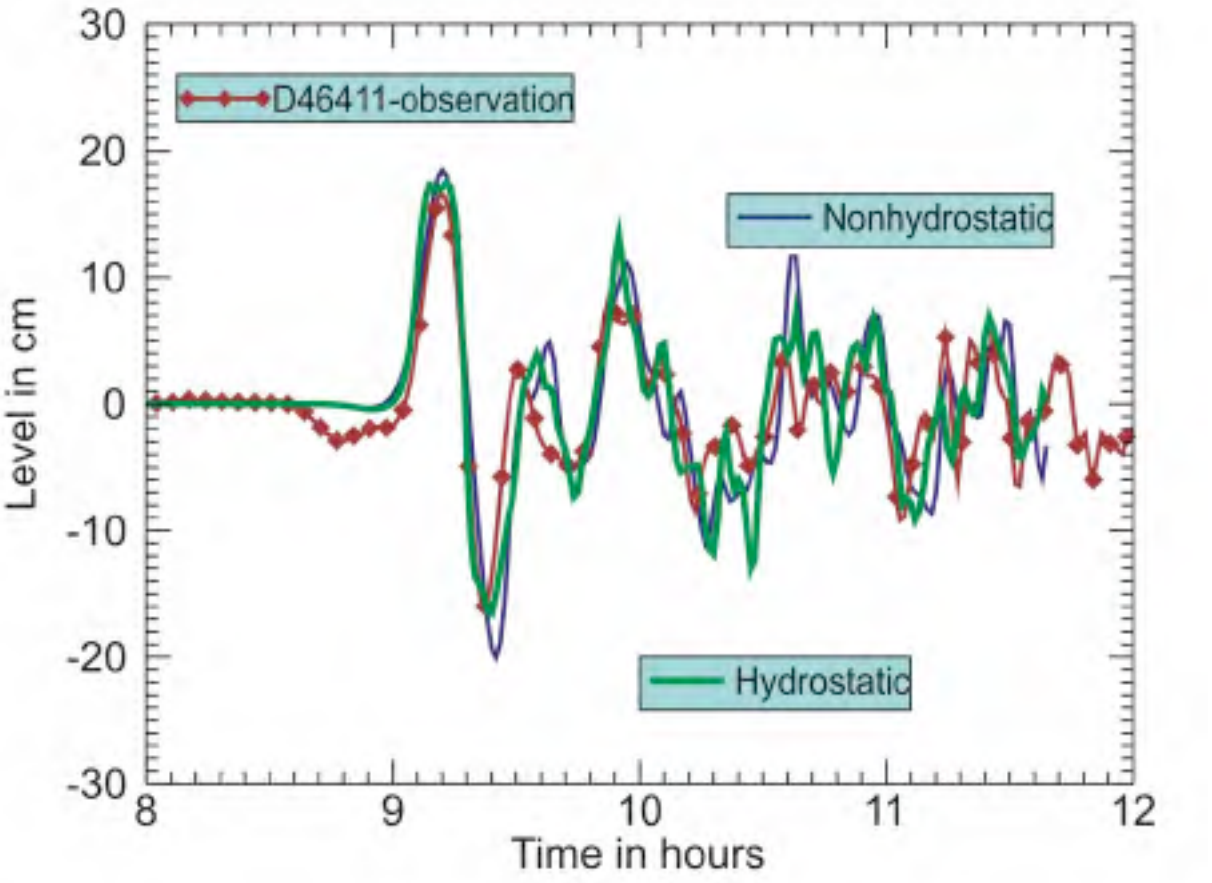

Figure 11. Sea level during Japan Tsunami of 11 March 2011 at the Dart Buoy 46411 (127 W, 39.94 N). Red color shows observation, blue denotes the dispersive and green non-dispersive computations. Time is given from the tsunami onset.

7. DISCUSSIONS AND CONCLUSIONS

The main purpose of the present study was to examine the trans-oceanic tsunami propagation for the KIT and JT where numerical simulation is done with the help of the nonlinear long wave equation and with the weakly dispersive gravity waves.

The results can be summarized as follows: (1) within the main energy lobe there exists a large difference between maximum dispersive and non-dispersive wave amplitudes, (2) in the far-field from the tsunami source the differences are small, (3) the transfer of the tsunami wave energy between the non-dispersive and dispersive modes is well confirmed by the energy flux, (4) temporal series from a few locations confirm the importance of dispersion in the main energy lobe as well. With the NHY

model and its HY counterpart, we are in a position to make careful comparisons between these model solutions. The solutions evolve quite uniformly in the region of the main energy lobe but it proves to be difficult to identify categoric differences between the NHY and HY model solutions and observations at the distances far-away from the main lobe. In summary in the region of the main lobe the 'classical' physics has been observed (Fig. 9), namely the amplitude of the first dispersive wave is smaller than the amplitude of the non-dispersive wave. Unfortunately, the computation depicted the large swath where inverse situation occurs, i.e., dispersive wave dominates over nondispersive waves. What is the source of this energy and why the energy fluxes organized such large and coherent areas the dispersive wave domination is difficult to conclude at the present time.

ACKNOWLEDGMENTS

This publication is the result in part of research sponsored by the Cooperative Institute for Alaska Research with the funds from the National Oceanic and Atmospheric Administration under cooperative agreement NA08OAR4320751 with the University of Alaska.

APPENDIX: ENERGY CONSERVATION

Tsunami transformation during generation, propagation and runup can be assessed through equation of energy and associated fluxes (Tinti and Bortolucci, 2000; Dutykh and Dias, 2008).
To consider energy fluxes for the vertically integrated equations we will start with simplified 2D case expressed by equations (11) and (13)

$$\rho D\frac{\partial}{\partial t}[\frac{w_s+w_b}{2}] = -(q_s-q_b) = q_b \qquad (A.1)$$

$$\rho D(\frac{\partial U}{\partial t}+\frac{U}{R_\circ\cos\phi}\frac{\partial U}{\partial\lambda}) = -\frac{g\rho D}{R_\circ\cos\phi}\frac{\partial\zeta}{\partial\lambda}-\frac{1}{R_\circ\cos\phi}[0.5q_b\frac{\partial}{\partial\lambda}(\zeta+\eta-H)+0.5D\frac{\partial q_b}{\partial\lambda}]-\tau_\lambda^b \qquad (A.2)$$

Denoting *ws 2+ wb 2* as *wa* , multiplying the (A.2) by *U* and (A.1) by *wa* we arrive at

$$\rho D\frac{\partial}{\partial t}[U^2/2]+\frac{1}{R_\circ\cos\phi}\frac{\partial[DU(\rho U^2/2]}{\partial\lambda} = -\frac{g\rho DU}{R_\circ\cos\phi}\frac{\partial\zeta}{\partial\lambda}$$

$$-U[0.5q_b\frac{1}{R_\circ\cos\phi}\frac{\partial(\zeta-H)}{\partial\lambda}+0.5D\frac{1}{R_\circ\cos\phi}\frac{\partial q_b}{\partial\lambda}-\tau_x^bU \qquad (A.3)$$

$$\rho D\frac{\partial}{\partial t}[\frac{w_a^2}{2}] = -(q_s-q_b)w_a = q_b\frac{(w_s+w_b)}{2} \qquad (A.4)$$

First we change the RHS of the above equation using definition of the surface and bottom vertical velocity

$$q_b\frac{(w_s+w_b)}{2}=0.5q_b(\frac{\partial\zeta}{\partial t}+\frac{U}{R_\circ\cos\phi}\frac{\partial\zeta}{\partial\lambda}-\frac{U}{R_\circ\cos\phi}\frac{\partial H}{\partial\lambda})=$$

$$0.5q_b(-\frac{1}{R_\circ\cos\phi}\frac{\partial DU}{\partial\lambda}+\frac{U}{R_\circ\cos\phi}\frac{\partial\zeta}{\partial\lambda}-\frac{U}{R_\circ\cos\phi}\frac{\partial H}{\partial\lambda})$$

and then adding side by side we arrive at energy equation

$$\rho D\frac{\partial}{\partial t}[U^2/2+w_a^2/2+g\frac{\zeta^2}{2}]+\frac{1}{R_\circ\cos\phi}\frac{\partial[DU(\rho U^2/2+\rho g\zeta+q_b/2)]}{\partial\lambda}=-\tau_x^bU \qquad (A.5)$$

The energy flux component along the N-S (φ) direction can be introduced in the analogous way, thus the energy flux along the E-W direction is

$$Fl_{E-W}=UD[\rho(U^2+V^2)/2+q_b/2+\rho g\zeta] \qquad (A.6a)$$

and along N-S direction

$$Fl_{N-S}=DV[\rho(U^2+V^2)/2+q_b/2+\rho g\zeta] \qquad (A.6b)$$

REFERENCES

Dunbar, D., P.Leblond and T.S.Murty. 1991. Evaluation of tsunami amplitudes for the Pacific Coast of Canada. Prog Oceanog. 26, 115-177.

Dutykh, D. and F. Dias. 2008. Tsunami wave energy. In : J. Locat, D. Perret, D. Turmel, D. Demers et S. Leroueil, (editors).

Proceedings of the 4th Canadian Conference on Geohazards: From Causes to Management. Presse de l'Université Laval, Québec, 594 p.

Gill, A.L. 1982. *Atmosphere--Ocean Dynamics.* Academic Press, Intl. Geophysical Series, Vol.30, 662 pp.

Grilli, S. T., Ioualalen, M., Asavanant, J., Shi, F., Kirby, J. T. and Watts, P., 2007, Source constraints and model simulation of the December 26, 2004 Indian Ocean tsunami, J. Waterway, Port, Coast. and Ocean Eng., 133, 414-428.

Horrillo J., Kowalik Z. and Y Shigihara. 2006. Wave dispersion study in the Indian Ocean Tsunami, Dec 26, 2004, Marine Geodesy, 29: 149-166.

Horrillo, J., Knight W. and Z. Kowalik. 2008. Kuril Island tsunami of November 2006: Part II. Impact at Crecent City by local enhancement, J. Geophys. Res., 113, C01021, doi:10.1029/2007JC004404

Imamura, F. and N. Shuto. 1989. Tsunami propagation simulation by use of numerical dispersion. International Symposium on Computational Fluid Dynamics pp.390-395.

Imamura, F., N. Shuto and C. Goto. 1990. Study on numerical simulation of the transoceanicpropagation of tsunamis. Part 2, Characteristics of tsunami propagation over the Pacific Ocean. Zisin (J, Seismol. Soc. Japan), 43:389-402.

Imamura F. 1996. Review of tsunami simulation with a finite difference method. In *Long-Wave Runup Models*, H.Yeh, P. Liu and C. Synolakis, Eds, World Scientific, 25--42.

Kirby, J. T., F. Shi, J. C. Harris and S. T. Grilli. 2012. Sensitivity analysis of trans-oceanic tsunami propagation to dispersive and Coriolis effects. Ocean Modeling, 42pps. (submitted).

Koshimura, S., Y. Hayashi, K. Munemoto and F. Imamura. 2008. Effect of the Emperor seamounts on trans-oceanic propagation of the 2006 Kuril Island earthquake tsunami. Geophysical Research Letters, vol. 35, L02611, doi:10.1029/2007GL032129.

Kowalik, Z. and Murty, T.S. 1993. *Numerical Modeling of Ocean Dynamics*, World Scientific, 481 pp.

Kowalik Z., W. Knight, T. Logan, and P. Whitmore, 2005. Numerical modeling of the global tsunami: Indonesian Tsunami of 26 December 2004. Science of Tsunami Hazards, Vol. 23, No. 1, 40- 56.

Kowalik, Z., J. Horrillo, W. Knight, and T. Logan. 2008. Kuril Islands tsunami of November 2006: 1. Impact at Crescent City by distant scattering, J. Geophys. Res., 113, C01020, doi:10.1029/2007JC004402.

Kulikov E. 2005. Dispersion of the Sumatra Tsunami Waves in the Indian Ocean detected by satellite altimetry.
http://www.pac.dfompo.gc.ca/science/oceans/tsunamis/documents/195610_0_merged_1107633516.pdf

Mader C. L. 1974. Numerical simulation of tsunamis. J. Phys. Oceanogr., 4, 74--82.

Mader C. L. 2004. Numerical Modeling of Water Waves, CRC Press, 274 pp.

Madsen, P. A., and H. A. Schaffer. 1999. A review of Boussinesq-type equations for surface gravity waves. In *Advances in Coastal and Ocean Engineering*, edited by P. L.-F. Liu, pp. 1-94 Volume 5. World Scientific, Singapore.

Okada, Y. (1985). Surface deformation due to shear and tensile faults in a half-space, Bulletin of the Seismological Society of America, v. 75, 1135-1154.

Ortiz, M., E. Gomez-Reyes, H.S. Velez-Munoz. 2001. A fast preliminary estimation model for transoceanic tsunami propagation. ITS 2000 Proceedings 723-739.

Proudman, J. 1953. *Dynamical Oceanography.* Methuen, J. Willey, London, 409 pp.

Rivera, P. C. 2006. Modeling the Asian tsunami evolution and propagation with a new generation mechanism and non-linear dispersive wave model. Science of Tsunami Hazards, Vol. 25, No. 1, page 18--33.

Saito, T. Y. Ito, D. Inazu, and R. Hino. 2011. Tsunami source of the 2011 Tohoku-Oki earthquake, Japan: Inversion analysis based on dispersive tsunami simulations, J. Geoph. Res., vol. 38, L00G19, doi:10.1029/2011GL049089.

Sato, S. 1996. Numerical simulation of 1993 southwest Kokkaido earthquake tsunami around Okushiri Island, Journal of Waterway, Port, Coastal, and Ocean Engineering, v 122, No. 5, 209--215.

Shigihara, Y. 2004. A study on application of non-linear dispersive wave theory to the numerical simulation of tsunami. PhD dissertation, Department. of Engineering, Tohoku University (in Japanese).

Stelling G.and M. Zijlema. 2003. An accurate and efficient finite-difference algorithm for non-hydrostatic free-surface fow with application to wave propagation. Int. J. Numer. Meth. Fluids, 43:1-–23.

Tinti, S., and Bortolucci, E. 2000. Energy of water waves induced by submarine landslides. Pure appl. Geophys., Vol. 157, pp. 281-318.

Yamazaki, Y., Z. Kowalik, and K. F. Cheung. 2008. Depth-integrated, non-hydrostatic model for wave breaking and runup. International Journal for Numerical Methods in Fluids, DOI: 10.1002/fld.1952.

Yoon, S. B. , Ch. H. Lim , and J. Choi. 2007. Dispersion-correction finite difference model for simulation of transoceanic tsunamis. Terr. Atmos. Ocean. Sci., Vol. 18, No. 1, 31-53.

Walters R.A. 2005. A simple-implicit finite element model for non-hydrostatic (dispersive) surface waves. Int. J. Numer. Meth. Fluids, 49, 721--737.

ISSN 8755-6839

SCIENCE OF TSUNAMI HAZARDS

Journal of Tsunami Society International

Volume 31 Number 3 2012

CATASTROPHIC FLANK COLLAPSE ON TA'U ISLAND AND SUBSEQUENT TSUNAMI: HAS THIS OCCURRED DURING THE LAST 170 YEARS?

Shaun Williams, Tim Davies, Jim Cole

Natural Hazards Research Centre
Department of Geological Sciences
University of Canterbury, PB 4800
Christchurch, New Zealand

ABSTRACT

Ta'u, the easternmost inhabited island in the Samoan Islands archipelago, exhibits a series of down-faulted benches on its southern flank, believed to be the remnant of ~30 km^3 catastrophic collapse. A historical map of Ta'u charted in 1839 during the United States Exploring Expedition, which did not show the benches, suggests that the event occurred less than 170 years ago. A collapse event of this magnitude would have generated a locally devastating tsunami, with possible impacts experienced at the regional level. However, no written or oral records of such an event exist. A number of key questions thus emerge, and formed the basis for this study. Did this event actually happen within the last 170 years, and if so, how and why could it have gone unnoticed? Or, is the event much older than the impression obtained from the literature? The catastrophic flank collapse was modeled using 100 m contour-resolution bathymetry data of the Ta'u region, coupled with rational assumptions made on the geometry of the failed mass. This enabled numerical landslide-tsunami simulation in the Cornell Multigrid Coupled Tsunami Model (COMCOT). The results indicate that if an event of this magnitude occurred in the last 170 years, it could not have gone unnoticed by local inhabitants. It thus seems likely that the initial survey conducted during the Exploring Expedition was inaccurate. Nevertheless, the well-preserved nature of the benches indicates collapse relatively recently and raises the possibility of future collapse.

Keywords: *Volcanic flank collapse, Ta'u Island volcano, tsunami,*

1. INTRODUCTION

Ta'u is the easternmost inhabited island in the Samoa Islands volcanic chain (Figure 1). It lies within the Manu'a Group of the Territory of American Samoa, and has three populated villages: Faleasao and Ta'u villages in the northwest, and Fitiuta village in the northeast. The total population of the island is just under 1000 (U.S. Census Bureau, 2000). The island has a total land area of ~46 km^2, with a summit ~925 m above mean sea level. It is located ~104 km east of Tutuila, the capital island of American Samoa.

Figure 1: Location map of the Samoan Islands (Map source: Google Earth).

Geologically the island is in a shield-building stage of volcanism (Macdonald and Abbott, 1970; Natland, 1980; Natland and Turner, 1985), although the nature of recent historical eruptions is uncertain. The island (and surrounding islands) have been inhabited for more than 3000 years (Nunn, 1994, 1998), but oral traditions only extend back a little under 1000 years (Linnekin et al, 1995), leaving no oral tradition regarding the ages of events before this time.

On the south flank of the island is apparently the remnant of a large-scale flank collapse with a total estimated volume of about 30 km^3 (Figures 2 and 3). Similar large-scale collapse features and resulting debris-avalanche deposits have also been recognized on the submarine slopes of Savai'i and Upolu (Hill and Tiffin, 1993; Keating and McGuire, 2000; Keating et al., 2000). The first internationally published map of the Samoa Islands was presented in Turner (1889), which depicts Ta'u as having a rounded, regular, dome-shaped morphology, with twice the present-day land area (Figure 4). All of the other islands along the chain look similar (morphologically) in the map as they do today; Ta'u is an obvious anomaly in this respect.

Figure 2: Photograph of the south flank of Ta'u (Photo by: Michael Tennant, Dec-2006).

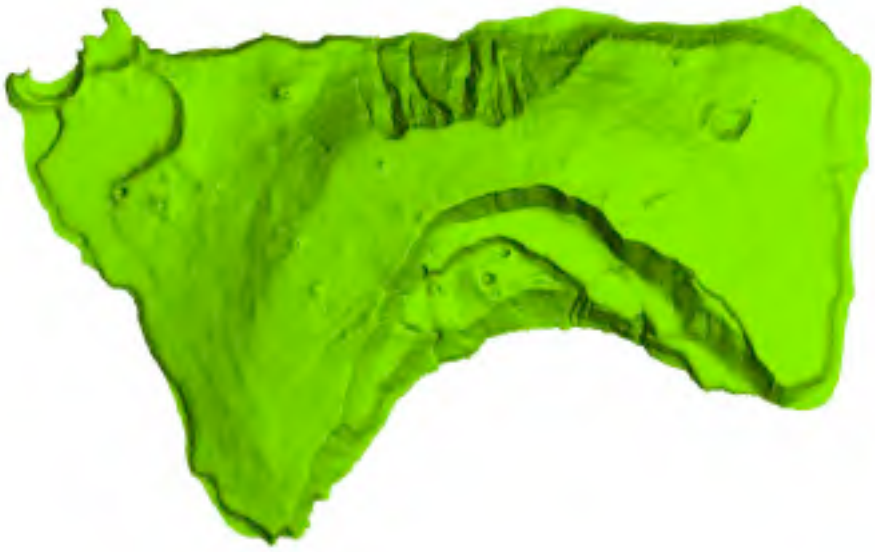

Figure 3: Digital elevation model of Ta'u Island showing the series of down-faulted benches on its southern flank.

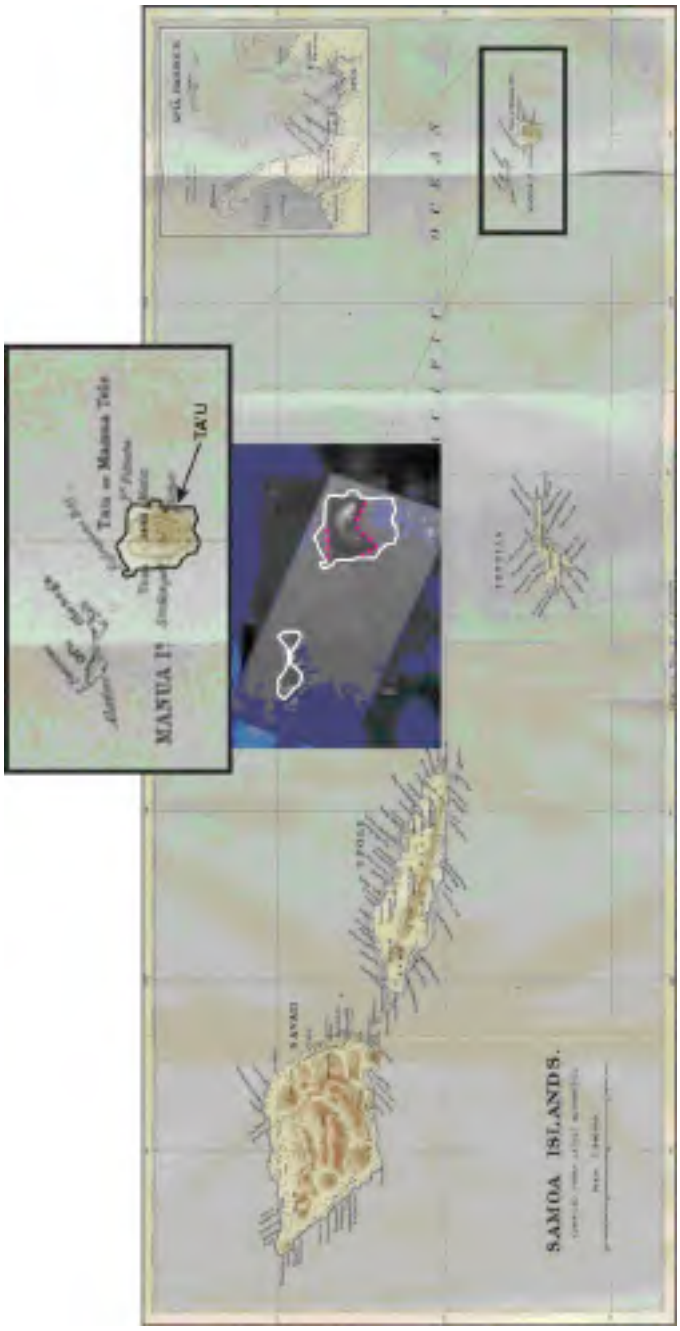

Figure 4: Historical map of the Samoa Islands presented in Turner (1889). A blow-up of the Manu'a group is given, and a simple map overlay to illustrate the obvious anomaly in the morphological depiction of Ta'u from its present shape. Ofu and Olosega Islands in the map-overlay illustrate an example of how other islands in the chain more or less looked the same then as they do today.

The map in Turner (1889) was based on the original survey charts of Charles Wilkes, who commanded the 1838 – 1842 U.S Exploring Expedition; the first United States government funded circum-navigational scientific exploring expedition. Wilkes reported that three days were spent accurately surveying the coasts of the Manu'a group. Ta'u was described as having the form of a regular dome (Figure 5), with an estimated land area of ~259 km^2. This strengthens the likelihood that large-scale collapse may have been recent. Given the oceanic environment in which collapse occurred, a large-scale local tsunami would have been generated with definite local catastrophic, and possibly regional, impacts. Interestingly, no written or oral documentation regarding such an event exists.

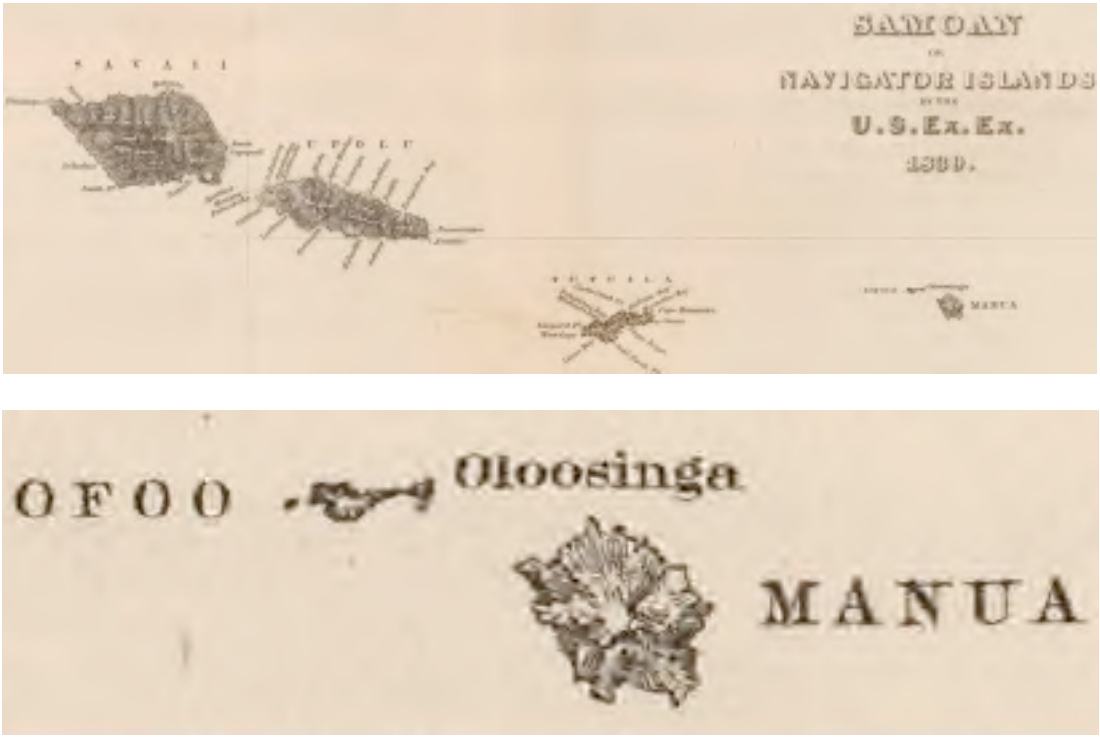

Figure 5: Map of the Samoa Islands charted in 1839 during the U.S.N. Charles Wilkes Expedition (from Wilkes, 1849). The bottom image is a blow-up of the eastern Manu'a Group from the top map; and depicts a rounded Ta'u morphology

Hence a number of questions emerge. On the one hand, there appears to be an obvious dilemma associated with the information described by Wilkes (1849), and later presented by Turner (1889). Were these early observations and resulting map indeed an accurate depiction of Ta'u in the mid to late 19th century? If so, why is there no written or oral account of the collapse? Is it possible that such an event went unnoticed? Or, could the map represent a significant cartographic error? If it does, it would raise serious debate regarding the reliability of the reported observations of Ta'u during the Charles Wilkes Expedition.

A review of the physical characteristics of Ta'u is presented here, including aspects of the island's geology and geomorphology with specific emphasis on evidence relevant to the nature and timing of the collapse, is followed by a tsunami modelling assessment. This involves numerical simulation of the flank-collapse using available data; the results have significant indirect implications for the timing of the event.

2. METHODS

A literature review combining geology and geomorphology was used to establish a solid information platform for understanding the relative timing and nature of physical processes in the area. Geomorphic analysis based on 10 m contour resolution topography data, 100 m contour resolution bathymetry data, and empirical observations were used to obtain a better understanding of significant morpho-structures in the area (Figure 6). It also enhanced understanding of the timing of formation of the collapse feature. Field observations in February and August 2008 were also undertaken to verify some of these features.

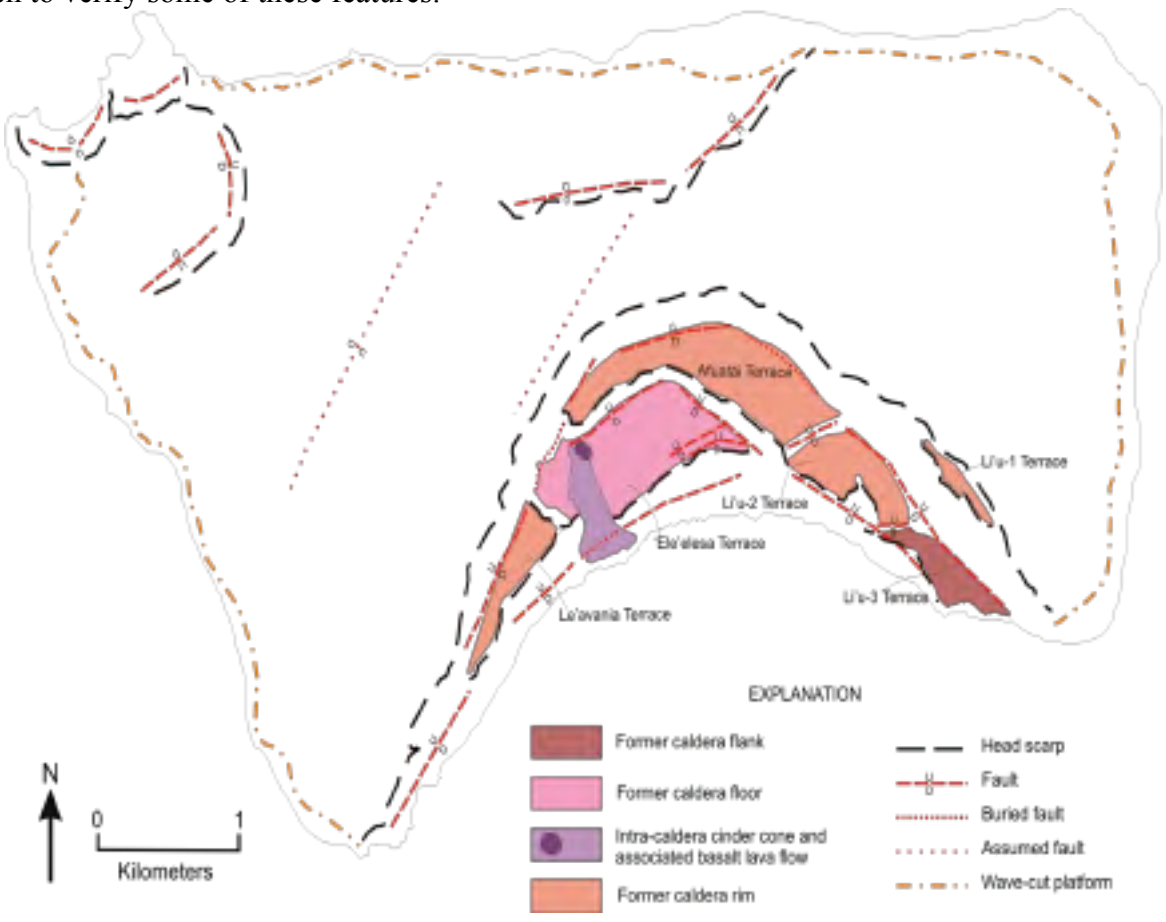

Figure 6: Main geomorphic features on the south flank of Ta'u; inferred using 10 m contour resolution data.

100 m contour resolution bathymetry data coupled with 3D analysis in the Vulcan 7.5 software was used to identify offshore features possibly associated with a collapse deposit, enabling rational assumptions to be made on the geometry of past collapse.

The Cornell Multi-grid Coupled Tsunami (COMCOT) model (version 1.7: Wang, 2009)) was used to model a range of landslide-induced tsunami scenarios; the landslides are hereafter referred to as submarine mass failures (SMF). COMCOT consists of a built-in set of complex algorithms that calculate and output ocean volume flux within a simulated grid, using bathymetry data as well as geometric characterizations of a failing mass. For this study, linear shallow water equations were used to describe water surface elevation and ocean flux in both spherical and Cartesian coordinate systems. An explicit leapfrog finite difference method was used to solve these equations in time and space for each grid cell within the simulation domain (Figure 7).

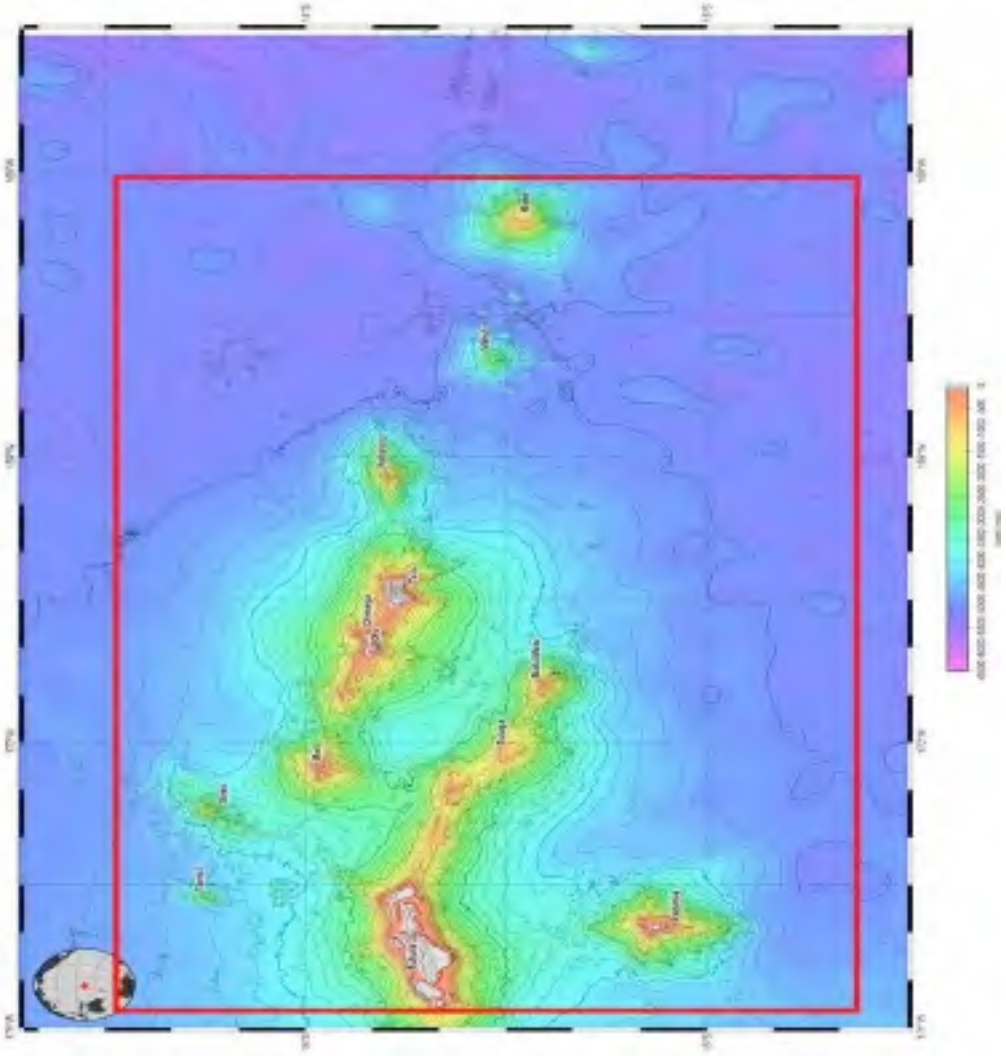

Figure 7: Merged bathymetry map of American Samoa; Region 14.3 S, 170.0 W (Source: http://earthref.org). Contour interval = 200 m. The red border indicates the numerical (simulation) domain.

Output data were visualized through post-processing using Matlab functions and scripts developed by Wang (2009). 100 m contour resolution multi-beam bathymetry data collected during the Alia Scientific Cruise Expedition in April 2005 was used in the simulations.

Using relationships established by Grilli and Watts (1999, 2001), Grilli et al (2002), Watts (1998 and 2000), and Watts et al (2003), an SMF was considered to be a wave maker whose shape and motion needed to be prescribed. The SMF was idealized as a mound (block) with elliptical cross-section translating along a straight incline at an angle θ to the horizontal. A maximum thickness T was defined in the middle of the mound, a total length b along the down-slope axis, a total width w along the cross-slope axis, and an initial vertical submergence d at the middle of the landslide. An elliptical platform, b by w, was also assumed for the SMF. The sliding mass was modeled as a rigid body moving along a straight incline with center of mass motion $s(t)$ parallel to the incline, and subject to external forces from added mass, gravity, and dissipation. COMCOT incorporates these relationships through the landslide tsunami source control files built into the system (Wang, 2009).

Assumptions were required for the volume and run-out distance of discharged SMF material. Volumetric estimations were based on contour interpolation of gravity data collected by Machesky (1965) - see Figure 8. The maximum volume of discharged material estimated from this reconstruction was 30 km^3. The maximum run-out distance of discharged material was estimated through 3D-exaggeration of bathymetry data in the Vulcan 7.5 software. Hummocky- type relief with 100 m amplitudes between troughs and peaks was noted approximately 30 km south of the island; these were assumed to represent the run-out maximum of the Ta'u SMF. Figure 9 and Figure 10 illustrates these assumptions.

A slide angle θ of 25^0 was used. The ratio of drop height to run-out distance h_0/x_c generally decreases with landslide volume (Ward and Day, 2003), and ranges from 0.05 to 0.15 for the Ta'u Island-sized (4 – 24 km^3) landslide. This implies a vertical mass drop height of about 1 – 3 km, and a run-out distance of about 20 - 30 km. A conservative volume of 4 km^3 was used in this study. The coefficient of basal friction μ, for low friction slides is approximately equal to h_0/x_c (Ward and Day, 2003). It was assumed here that $\mu \sim h_0/x_c$, hence a mean μ value of 0.1 was used. The mechanism inducing this low basal friction was assumed to be attributed to intense rock fragmentation that occurs in the basal region of large landslides (Davies & McSaveney, 2009; Davies et al, 2010), and has been inferred to act also in submarine mass movements. The Ta'u event appears to be similar to the 1884 Ritter Island collapse in Papua New Guinea (Ward and Day, 2003). A similar terrestrial analogy would be the debris avalanche of Mount St Helens volcano in 1980, where block-slides accelerated to speeds of over 50 ms^{-1} within 26 s and 700 m of the start time and location (Glicken, 1996; Voight et al, 1983; Ward and Day, 2003).

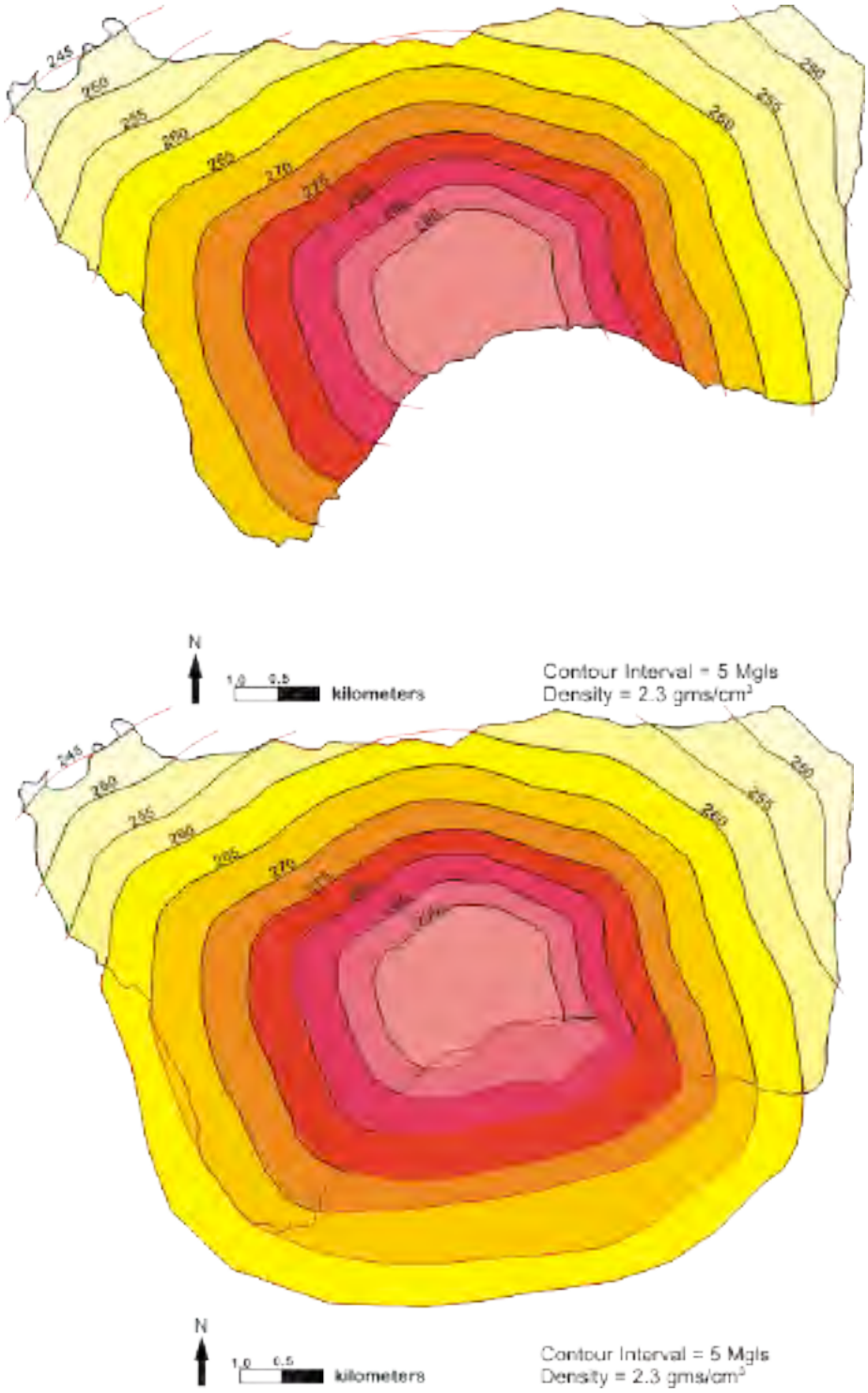

Figure 8: Gravity contour reconstruction using simple point interpolation, illustrating how the island may have looked in plan-view before (bottom image) and after (top image) to collapse.

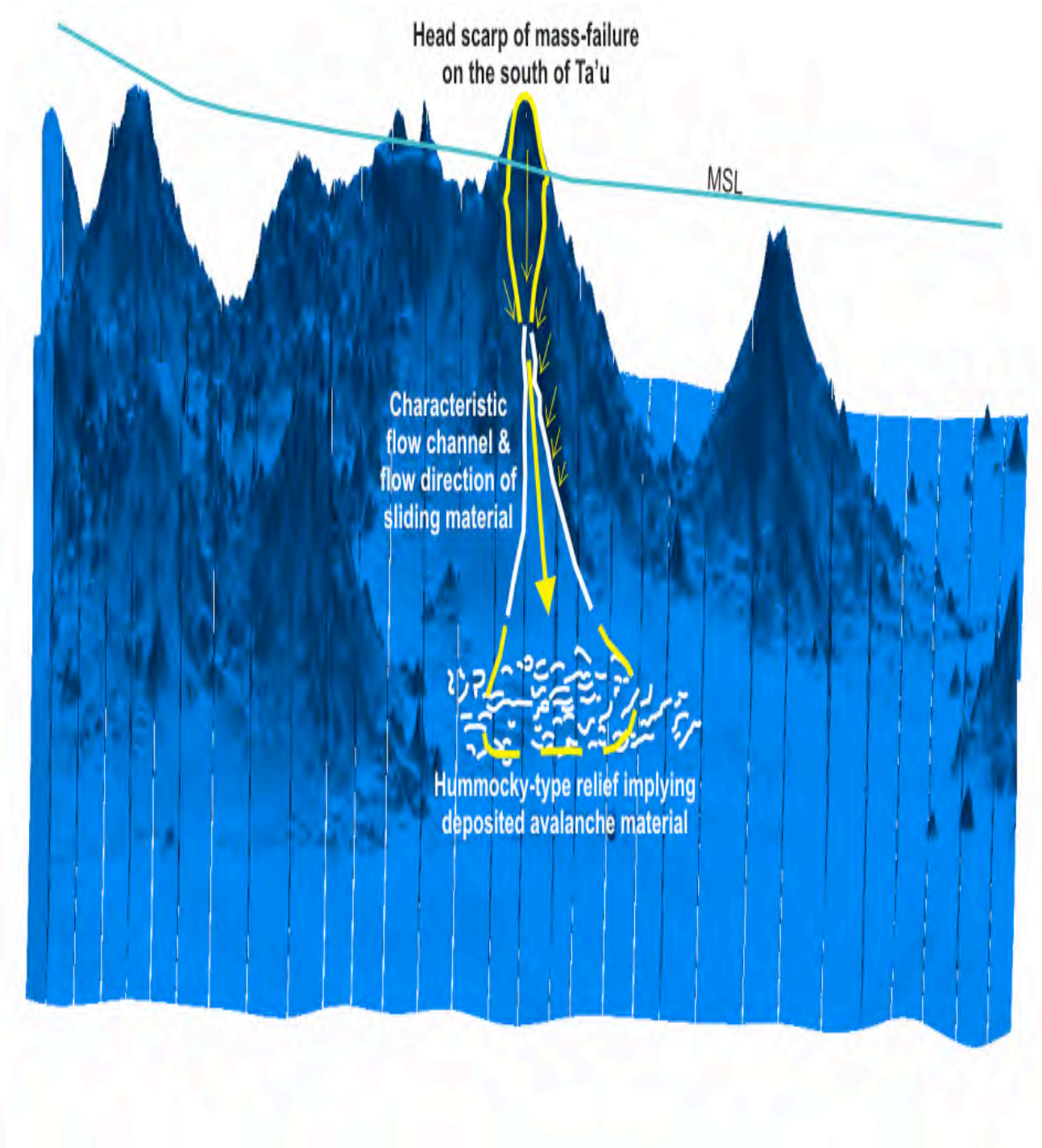

Figure 9: Exaggerated 3D-section view looking north at the southern flank of the Ta'u volcanic pile. Vertical lines shown across the N-S plane can be ignored. An offshore submarine flow channel and hummocky-type deposit are apparent south of the avalanche scarp.

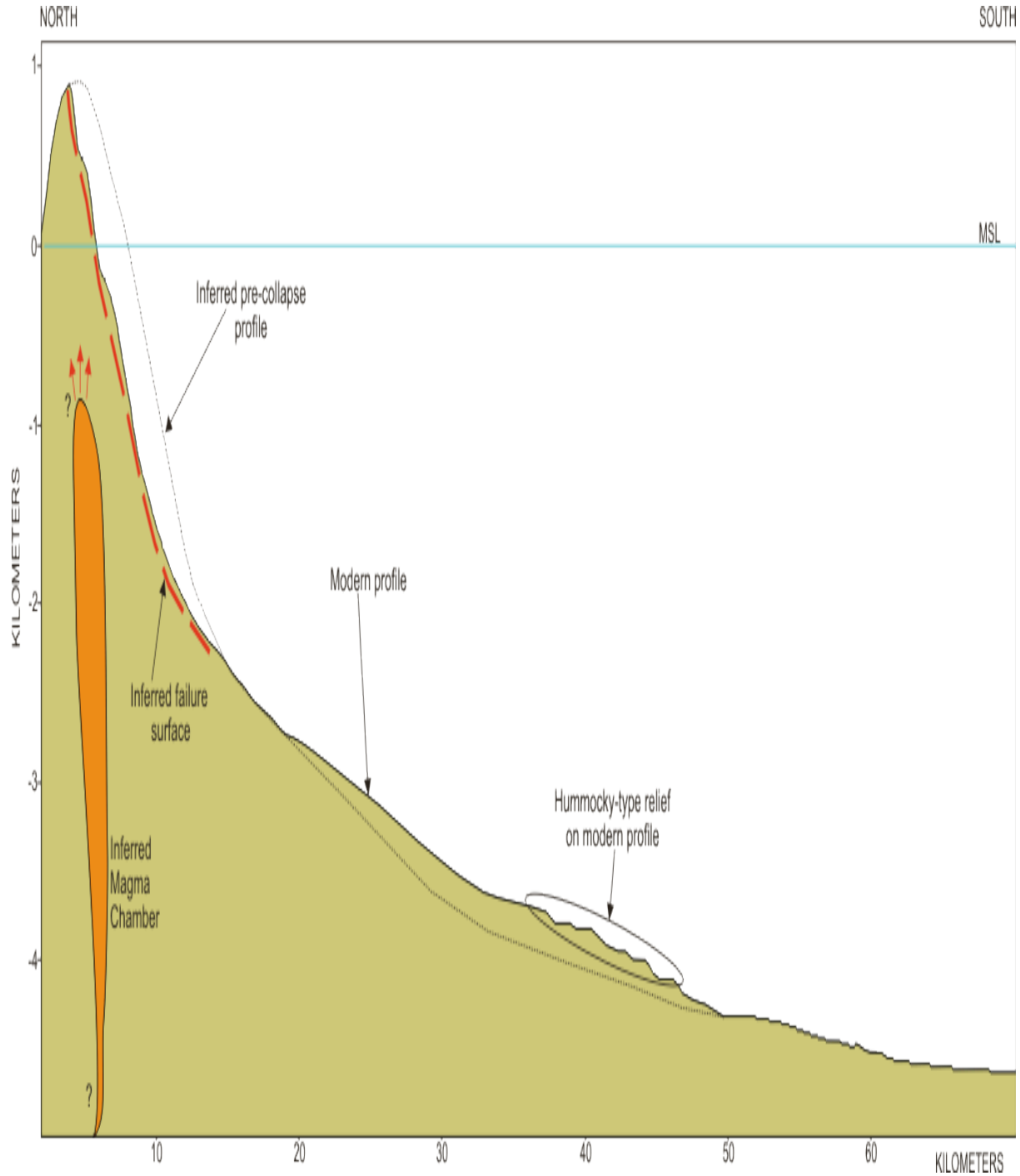

Figure 10: Cross-section of the south flank and offshore morphology of Ta'u. The inferred pre-collapse profile and failure surface are shown, as well as the inferred deposit denoted by the hummocky relief ~30km offshore.

3. RESULTS AND INTERPRETATIONS

3.1 Geomorphic and possible age interpretations

A geomorphic assessment of the south flank was undertaken to obtain a better understanding of the landscape features and processes on Ta'u, as well as their relative timing of formation.

The summit of Ta'u appears to be the northern caldera rim, which overlooks a series of down-faulted, approximately horizontal benches (Figures 2 and 3). Afuatai, the upper bench, is covered with thin-bedded horizontal flows of oceanite and olivine basalt, with a few small areas that are mantled by a 1 m bed of fine-grained tuff with laminate less than 1.3 cm thick. The lower bench, Ele'elesa, contains three large pit craters and a cinder cone, with a likely fault scarp marking the cliff-face down to the ocean. Lava flows exposed in the high fault-scarp bounding Afuatai bench to the summit of Lata mountain dip approximately 15^{o} away from the summit. Stice and McCoy (1968) suggested that the bench at Afuatai and the narrower benches to the southwest at Leavania, and to the southeast at Li'u, represent the former summit of the volcano, which has dropped approximately 450 m. They also suggested that the lower bench at Ele'elesa, the pit craters and the cinder cone, represent the original caldera of the volcano. The approximately horizontal bedding of flows comprising these benches relative to the average 15^{o} dip of flows in the southeast and west escarpments probably indicates a series of rotational slips along the fault-surface(s). Bathymetry and gravity data suggest that the caldera has no southern rim, as indicated by the steep drop of the seafloor to about 3000 m on the south side (Fenner et al, 2008).

Lava flows from the cinder cone eruption mapped separately in Figure 6 flow over the Ele'elesa scarp-face, indicating that it was deposited after collapse. This eruption may have been associated with the collapse, although any firm conclusions would be premature at this stage. If this were the case, it seems likely collapse was older than the 170 yr impression given by the map in Wilkes (1849). If the cinder cone eruption was historical and associated with the collapse, it would probably have been documented either through written or oral accounts. The absence of either of these leads to the belief that the eruption was pre-historic, probably $\geq$ 1 Ka; old enough to have disappeared from oral records (Linnekin et al, 1995). The young erosional gullies formed at the head of the north flank fault appear to be directly related to surface erosion. This flank also appears to be unbuttressed, meaning the likelihood of future collapse similar to the south flank could occur.

Erosional processes resulted in the formation of stream gullies and a 60 m sea cliff around most of the island, the northwestern portion being buried by the Faleasao formation. The sea-cliff here is thought to represent a wave-cut platform, formed during the sea level high-stand associated with the last interglacial maximum ~ 0.07 - 0.12 Ma. Bathymetry suggests that a submarine wave-cut platform encircles most of the island, and is assumed to have formed during the sea level low-stand associated with the last glacial maximum ~ 0.018 Ma. Large-scale catastrophic collapse or long-term slope failure (Stice and McCoy, 1968) resulted in the removal of the southern half of the original shield volcano - an estimated total volume of 4 – 30 km^3. This paper assumes the former. Both the sub aerial and submarine wave-cut platforms are absent on the south flank, leading to the belief that collapse occurred after their formation; i.e. < 0.018 Ma.

3.2 Modeling of the flank collapse and subsequent tsunami

The results discussed below assume the rapid collapse of a 4 km^3 mass along a slide angle θ of 25^0, with a run-out distance of 18.4 km. The length of the sliding mass = 3.2 km, width = 2.5 km, and thickness = 0.5 km. The 500 m drop of the present-day Afuatai bench from the Lata summit was assumed to be characteristic of the maximum thickness in the middle of the sliding block (Ward and Day, 2003). The specific density used was 2.2 (sliding mass density = 2300 kgm^{-3}: density of seawater = 1030 kgm^{-3}), and the coefficient of basal friction was 0.1. The simulated event run-time was 30 minutes (1800 s), and snapshots of ocean volume flux (flow per unit area) were recorded at 1-minute simulation intervals. Dispersion was ignored as shallow-water techniques were used. Figure 11 shows the simulated tsunami amplitudes and propagation at given times after landslide initiation. Figure 12 shows the main flux in the north-south and east-west directions.

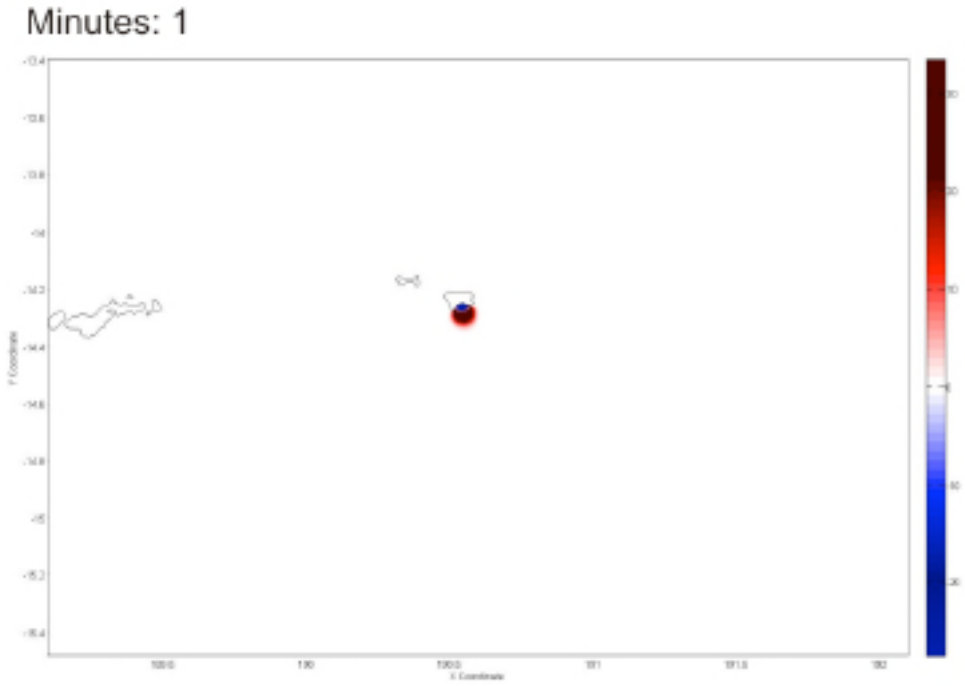

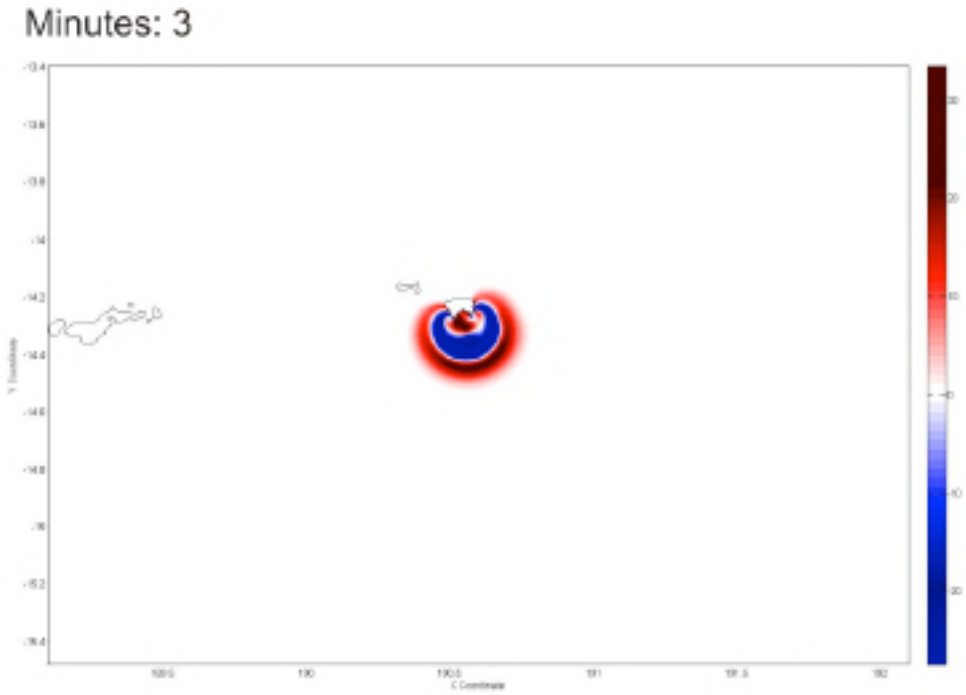
Minutes: 3

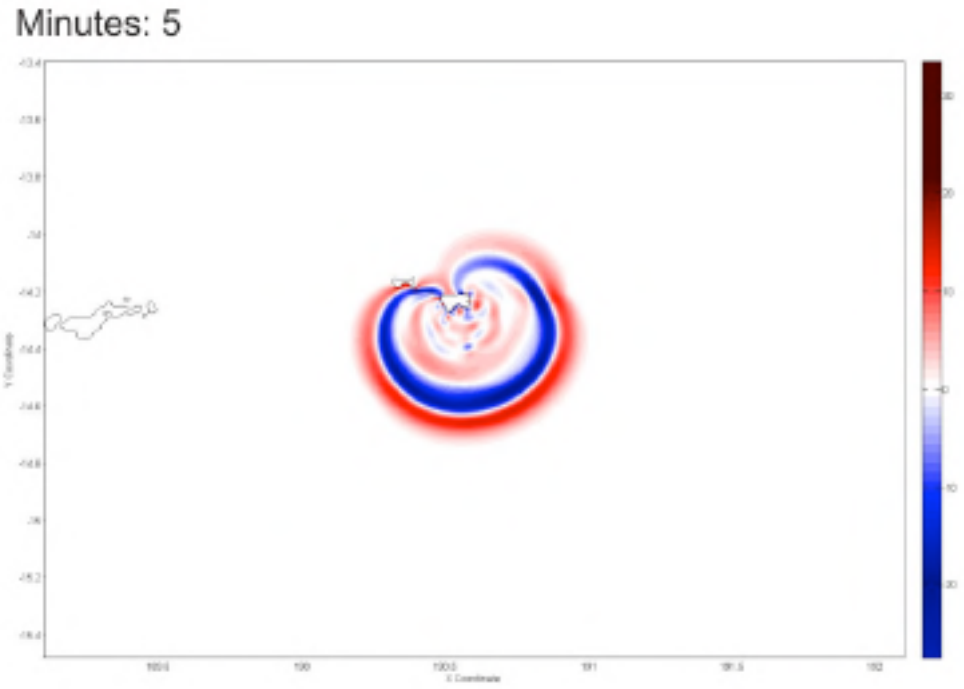
Minutes: 5

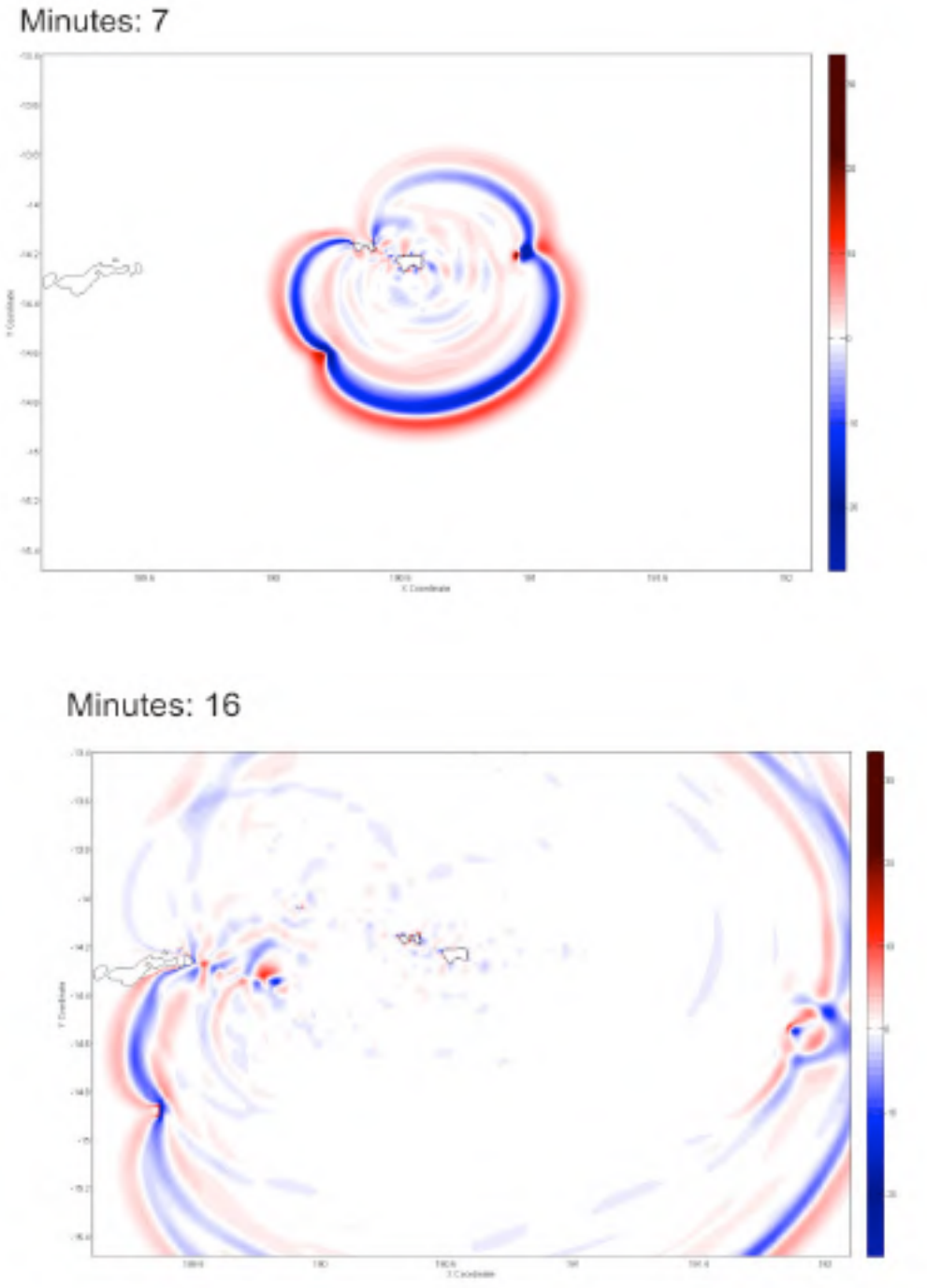

Figure 11: Simulated tsunami amplitude and flux ($m^3 \cdot m^{-2} \cdot s^{-1}$) predicted for the Ta'u collapse at 1, 3, 5, 7 and 16 minutes after initiation of the event.

The duration of the landslide determined in the idealized block-slide analysis was 7 minutes, with a peak slide velocity of 75.2 ms^{-1}. The average slide velocity was 43 ms^{-1}. Initial acceleration was 1.1 ms^{-2}, and deceleration of -0.1634 ms^{-2} began 1 minute after slide initiation; the mass slid for about 4.5 km before reaching the flat of the ocean floor at a depth of about 3 km. It slowed down for the remainder of the travel until it stopped approximately 18.4 km from source. The landslide generated a tsunami with amplitudes greater than 20 m propagating in all directions 5 minutes after slide initiation.

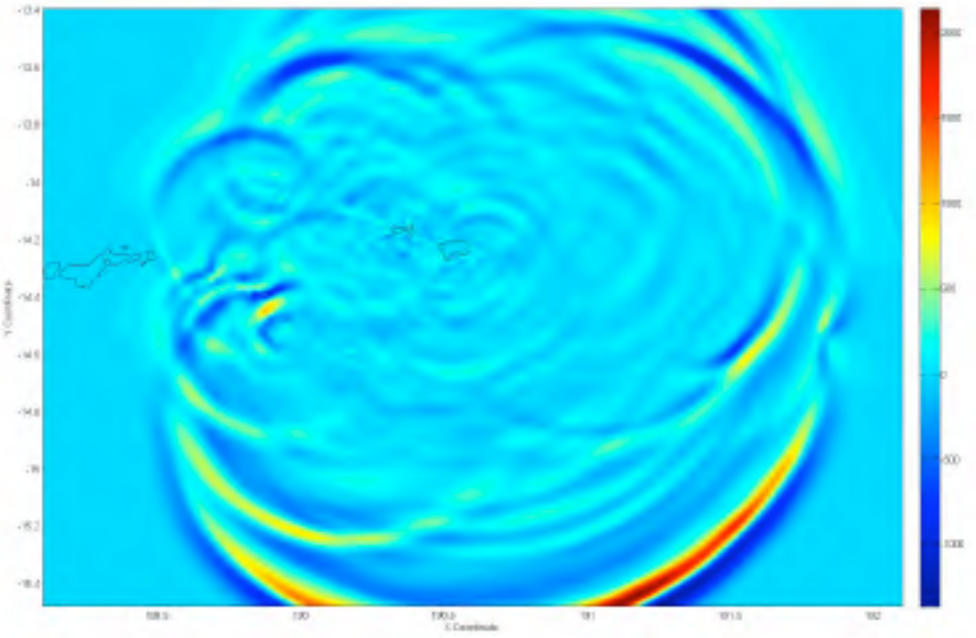

Figure 12: Direction of tsunami propagation in the X (north-south; top map) and Y (east-west; bottom map) axis. Main flux along the X-axis is southward, although sufficient wave diffraction around the island results in a northward propagating wave. Flux along the Y-axis is relatively proportional in both the east and west directions, respectively.

These effects are comparable with the Ritter Island collapse modelled by Ward and Day (2003). Their results showed a 4.6 km^3 landslide, which slid with an average velocity of 40 ms^{-1} (peak velocity near 70 ms^{-1}), and took about 5 minutes to run its course. The steep initial basal slope of 10 – 15^0 (peak of 25^0) in their model made for a short-lived acceleration phase. Having reached a decrease in basal slope, the slide spent much of the remainder of its movement travelling at a limiting speed. Friction coefficients used in their analysis ranged between 0.05 – 0.07. The simulation generated a tsunami with wave amplitudes of 20 m offshore of New Britain, compared to the actual 12 – 15 m elevation of inundation measured there. This difference was considered insignificant, and was

attributed to the short wave periods and loss of wave energy on the offshore reefs and in coastal trees as the wave approached and inundated the coast. The smaller debris avalanche of 0.05 – 0.09 km^3 which formed during the 26th December 1997 eruption of Soufrière Hills volcano on Montserrat, was immediately followed by an energetic pyroclastic density current that devastated 10 km^2 of the south-western volcano flank. The event generated local tsunamis which impacted Montserrat with maximum wave run-up heights > 10 m (Le Friant et al, 2006; Sparks et al, 2002; Voight et al, 2002).

The simulation results for the Ta'u block-slide seem consistent with the examples discussed above. The 0.1 coefficient of basal friction used was consistent with the h_0/x_0 ratio determined for the slide. This would have been sufficient to slow the sliding mass down to rest at about 18 km from its source. The rapid acceleration to a peak slide velocity of 75.2 ms^{-1} before slowing down was likely attributed to the steep initial basal slope of 20 - 25^0. Tsunami waves with amplitudes > 20 m were generated offshore. The main direction of tsunami propagation was southward. Wave diffraction around the island resulted in northward propagating waves.

The study showed that rapid flank collapse resulting in the present-day morphology of the south flank would have generated a tsunami propagating in all directions. Offshore wave amplitudes > 20 m would have reached the villages of Ta'u and Faleasao in the northwest, and Fitiuta in the northeast between 3 – 4 minutes after landslide initiation. Similar offshore waves would have reached the south coast of Ofu and Olosega islands about 5 minutes after initiation. Wave amplitudes between 10 – 15 m would have occurred offshore of Tutuila Island 104 km west of Ta'u at about 17 minutes after initiation. 10 – 15 m waves also propagated outside of the simulated numerical domain, possibly indicating that populated islands adjacent to, but outside, of the domain may have also experienced similar offshore tsunami amplitudes.

The island of Upolu, about 200 km west of Ta'u, may have experienced offshore wave amplitudes > 5 m in some areas, with smaller amplitudes experienced offshore of southeast areas on Savai'i, 100 km further west. Swains atoll about 380 km north-northwest may have experienced similar waves. Other places such as the high raised limestone island Niue 500 km south, the low-lying Pukapuka atoll in the northern Cook Islands > 500 km northeast, the Tokelau atolls > 500 km north, and Tafahi and Niuatoputapu islands in Tonga 480 km southwest, perhaps experienced waves < 2 m.

The likely elevation of inundation experienced at the northwest villages on Ta'u, and on Ofu and Olosega islands were probably several metres lower than the modeled offshore waves > 20 m. The village of Ta'u would most likely have experienced the greatest elevation of inundation (perhaps > 10 m), being the closest to the source and located < 10 m above mean sea level. The tidal range in the area is approximately 0.85 m (Izuka, 2005), meaning inundation would have occurred regardless of the time of the day. The fringing reef bounding the narrow lagoon about 100 m between the reef crest and the coastline would have induced short-period waves and loss of energy as the wave approached the coast. Limited coastal vegetation on the calcareous sedimentary unit < 10 m above mean sea level, would have meant probable inundation to the western base of the Tunoa shield between 100 – 400 m inland. Similar inundation impacts may have been experienced at Faleasao, and on Ofu and Olosega. The fringing reef surrounding Ofu and Olosega is greater than 200 m from crest to shoreline in most places, although > 95% of inhabited areas are situated < 10 m above mean sea level. The proximity of Fitiuta village in the northeast of Ta'u, > 25 m above mean sea level, would have meant that no inundation impacts were experienced at this site.

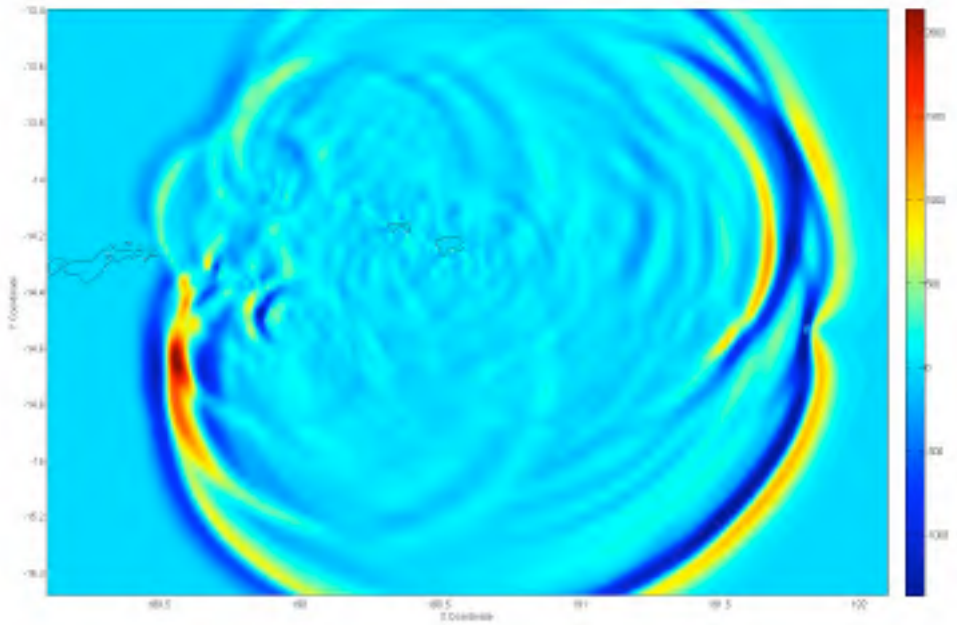

Figure 12: Direction of tsunami propagation in the X (north-south; top map) and Y (east-west; bottom map) axis. Main flux along the X-axis is southward, although sufficient wave diffraction around the island results in a northward propagating wave. Flux along the Y-axis is relatively proportional in both the east and west directions, respectively.

4. CONCLUSIONS

The modeled landslide-tsunami results demonstrate that if a historical collapse event occurred within the last 167 years resulting in the present day south flank morphology, the impacts could not have gone unnoticed by inhabitants of Ta'u and Faleasao villages on Ta'u Island, and inhabitants of Ofu, Olosega and Tutuila islands, respectively. It is likely that inhabitants on eastern and some southern areas of Upolu and Savai'i islands would have also noticed the impacts. There is no evidence of this in recorded history. This suggests that the depiction of Ta'u in Turner (1889), which was based on the original survey charts of Wilkes (1849), may have been incorrect, and the catastrophic collapse of the south flank and subsequent tsunami were much older.

The only alternative is that there were a series of smaller collapses requiring lower friction coefficients, and over a longer period of time. Smaller tsunami, which may have formed from these collapses, may not have had sufficient energy to diffract around the island and inundate exposed villages. However it seems unlikely that multiple collapses could have occurred in the last 170 years, without some record in the oral history.

ACKNOWLEDGEMENTS

We thank Dr. Gegar Prasetya and Dr. Xiaoming Wang of GNS Science NZ for their help regarding the use of the COMCOT numerical model. We acknowledge and thank NZAID and the Mason Trust, University of Canterbury for funding this research.

REFERENCES

Davies, T.R.H. and McSaveney, M.J., (2009). The role of rock fragmentation in the motion of large landslides. Engineering Geology. 109 (1-2): 67-79

Davies, T.R.H., McSaveney, M.J. and Kelfoun, K. (2010). Runout of the Socompa volcanic debris avalanche, Chile: a mechanical explanation for low basal shear resistance. Bulletin of Volcanology **72**:933–944 DOI 10.1007/s00445-010-0372-9

Fenner, D., Speicher, M., Gulick, S., (2008). The State of Coral Reef Ecosystems of American Samoa. In: Waddell, J.E. and A.M. Clarke (eds) 2008. The State of Coral Reef Ecosystems of the United States and Pacific Freely Associated States: 2008. NOAA Technical Memorandum NOS NCCOS 73. NOAA/NCCOS Center for Coastal Monitoring and Assessment's Biogeography team. Silver Spring, MD. 569 pp.

Glicken, H., (1996). Rockslide-Debris Avalanche of May 18, 1980, Mount St. Helens Volcano, Washington. Open-file Report 96-677. Cascades Volcano Observatory, Vancouver, WA 98661.

Grilli, S.T. and Watts, P., (1999). Modelling of waves generated by a moving submerged body: Applications to underwater landslides. Eng. Analysis with Boundary Elements. 23(8): 645-656.

Grilli, S.T. and Watts, P., (2001). Modelling of tsunami generated by an underwater landslide in a 3-D numerical wave tank. Proc. of the 11th Offshore and Polar Eng. Conf., ISOPE01, Stavanger, Norway. 3: 132-139.

Grilli, S.T., Vogelmann, S., Watts, P., (2002). Development of 3-D numerical wave tank for modeling tsunami generation for underwater landslides. Eng. Analysis with Boundary Elements 26(4): 301-313.

Hill, P.J. and Tiffin, D.L., (1993). Geology, sediment patterns and widespread deformation on the sea floor off Western Samoa revealed by wide-swath imagery. Geo-Marine Letters 13: 116-125.

Izuka, S.K., 2005, Reconnaissance of the Hydrogeology of Ta'u, American Samoa: U.S. Geological Survey Scientific Investigations Report 2004-5240, 20 p.

Keating, B.H., Helesley, C.E., Karogodina, I., (2000). Sonar studies of submarine mass wasting and volcanic structures off Savaii Island, Samoa. Pure and Appl. Geophys. 157: 1285-1313.

Keating, B.H., McGuire, W.J., (2000). Island Edifice Failures and Associated Tsunami Hazards. Pure and Appl. Geophys. 157: 899-955.

Le Friant, A., Boudon, G., Komorowski, J.-C., Heinrich, P., Semet, M.P., (2006). Potential Flank-Collapse of Soufrière Volcano, Guadeloupe, Lesser Antilles? Numerical Simulation and Hazards. Natural Hazards 39: 381-393.

Linnekin, J., Hunt, T., Lang, L., McCormick, T., (1995). Ethnographic Assessment and Overview: The National Park of American Samoa. Department of Anthropology, University of Hawaii.

Macdonald, G.A. and Abbott, A., (1970). Volcanoes in the Sea. University of Hawaii Press Honolulu, pp 137-147.

Machesky, L.F., (1965). Gravity Relations in American Samoa and the Society Islands. Pac. Sci. 19(3): 367-373.

Natland, J.H., (1980). The progression of volcanism in the Samoan linear volcanic chain. American Journal of Science 280-A: 709-735.

Natland, J.H. and Turner, D.L., (1985). Age progression and petrological development of Samoan shield volcanoes: Evidence from K-Ar ages, lava compositions and mineral studies. In: Brocker, T.M., (ed). Geological investigations of the northern Melanesian borderland: Houston, Texas, Council for Energy and Mineral Resources. Circum-Pacific Council for Energy and Mineral Resources Earth Science Series 3: 139-172.

Nunn, P.D., (1994). Oceanic Islands. Blackwell, Oxford.

Nunn, P.D., (1998). Pacific Island Landscapes: Landscape and Geological Development of Southwest Pacific Islands, especially Fiji, Samoa and Tonga. Institute of Pacific Studies, The University of the South Pacific, Fiji.

Sparks, R.S.J., Barclay, J., Calder, E.S., Herd, R.A., Komorowski, J-C., Luckett, R., Norton, G.E., Ritchie, L.J., Voight, B., Woods, A.W., (2002). Generation of a debris avalache and violent pyroclastic density current on 26 December (Boxing Day) 1997 Soufrière Hills Volcano, Montserrat. In: Druitt, T.H. & Kokelaar, B.P. (eds). The Eruption of the Soufrière Hills Volcano, Montserrat, from 1995 to 1999. Geological Society, London, Memoirs, 21: 409-434.

Stice, G.D., McCoy, F.W., (1968). The geology of the Manu'a Islands, Samoa. Pacific Sci. 22: 427-457.

Turner, G.A., (1889). Samoa. Scottish Geographical Magazine 5: 235 - 256.

U.S. Census Bureau, (2000). Census 2000 Data for American Samoa. Online at http://www.census.gov/census2000/americansamoa.html

Voight, B., Komorowski, J-C., Norton, G.E., Belousov, A.B., Belousova, M., Boudon, G., Francis, P.W., Franz, W., Heinrich, P., Sparks, R.S.J., Young, S.R., (2002). The 26 December (Boxing Day) 1997 sector collapse and debris avalanche at Soufrière Hills Volcano, Montserrat. In: Druitt, T.H., Kokelaar, B.P. (eds) 2002. The Eruption of Soufrière Hills Volcano, Montserrat, from 1995 to 1999. Geological Society, London, Memoirs, 21: 363-407.

Voight, B., Janda, R.J., Glicken, H., Douglass, P.M., (1983). Nature and mechanics of the Mount St. Helens rockslide-avalanche of 18 May 1980. Geotechnique 33: 243-273.

Wang, X., (February 2009). User Manual for COMCOT Version 1.7. Geological and Nuclear Sciences NZ, Wellington.

Ward, S.N., Day, S., (2003). Ritter Island Volcano - lateral collapse and the tsunami of 1888. Geophys. J. Int. 154: 891-902.

Watts, P., (1998). Wavemaker curves for tsunamis generated by underwater landslides. J. Wtrwy. Port, Coast, and Oc. Eng., ASCE 124(3): 127-137.

Watts, P., (2000). Tsunami features of solid block underwater landslides. J. Wtrwy. Port, Coast, and Oc. Eng., ASCE 126(3): 144-152.

Watts, P., Grilli, S.T., Kirby, J.T., Fryer, G.J., Tappin, D.R., (2003). Landslide tsunami case studies using Boussinesq model and a fully nonlinear tsunami generation model. Nat. Haz. Earth Sys. Sci. 3: 391-402.

Wilkes, C., (1849). Narrative of the United States Exploring Expedition during the years 1838, 1839, 1840, 1841, 1842, In five volumes with thirteen maps. Vol.1. U.S.N. Philadelphia.

ISSN 8755-6839

SCIENCE OF **TSUNAMI HAZARDS**

Journal of Tsunami Society International

Volume 31 **Number 3** **2012**

THE 2010 CHILEAN TSUNAMI: BEHAVIOR ON THE ECUADORIAN COAST AND THE GALAPAGOS ISLANDS

H. Moreano[1], P. Arreaga[2] and J. Nath[3]

[1]Instituto de Investigación Científica y Desarrollo Tecnológico, Centro de Estudios Integrales del Ambiente. Universidad Estatal Península de Santa Elena, Vía: La Libertad - Santa Elena, La Libertad.

[2]Laboratorio de Tsunamis. Instituto Oceanográfico de la Armada. Avda. de la Marina, Guayaquil.

[3]Departamento de Hidrografía, Sección Mareas. Instituto Oceanográfico de la Armada, Avda. de La Marina. Guayaquil.

E-mail: hmoreano@gye.satnet.net, parreaga@inocar.mil.ec, jnath@inocar.mil.ec

ABSTRACT

Available mareograms from ports of Ecuador and the Galapagos Islands made possible analysis and understanding of the tsunami generated by the great Chile earthquake of 27 February 2010. In general, all tidal gauges along the coastal zones at these localities begun to record sea level changes minutes after the predicted low water tide near 08:30 in the morning of February 27. The mareographic records showed waves with amplitudes ranging from 20 to 70 cm and periods of up to 2 hours. From then on the records indicated lower amplitude waves and rather short periods perhaps due to local conditions at each port. At Caleta, Aeolian and Baltra Island in the Galapagos, sea level changes begun just before low tide. Recorded waves in Academy Bay of Puerto Ayora (Santa Cruz Island) ranged at about 35 cm in amplitude and boats sat on the rocky bottom at around 07:30 (local time). Initial periods were less than 60 minutes but later were shorter - possibly because of the port's configuration. The water level fluctuations lasted for about 48 hours. Along the coast of Ecuador the tsunami wave amplitudes ranged between 20 and 70 cm the periods were longer but shorter in the Galapagos Islands. Based on initial sea level changes and the issuance of a tsunami warning at Puerto Ayora on Santa Cruz Island, there was evacuation of coastal inhabitants to safer, higher grounds.

***Keywords**: Tsunami Chile 2010, Impact on Ecuador and Galapagos Islands.*

Science of Tsunami Hazards, Vol. 31, No. 3, page 199 (2012)

1. INTRODUCTION

The great earthquake (Mw= 8.8) occurred at 03:34 (local Chilean time) on 27 February 2010, along the south central Nazca/South American plate boundary, just offshore Maule. Its epicenter was at 35.9 S and 72.7 W and had a focal depth estimated at 35 km. It occurred as thrust-faulting along a highly stressed coastal segment of Chile's central seismic zone - extending from about 33ºS to 37ºS latitude - where active, oblique subduction of the Nazca tectonic plate below South America occurs at the high rate of up to 80 mm per year. It was the 5th most powerful earthquake in recorded history and the largest in the region since the extremely destructive May 22, 1960 magnitude M_w9.5 earthquake near Valdivia (Pararas-Carayannis, 2010). Its rupture extended nearly 500-600 km in length and the area that was affected was estimated to be 130 km wide. The quake generated destructive tsunami waves that struck the Chilean coastline and also affected distant locations elsewhere in the Pacific Ocean Basin (Cienfuegos, 2010; Comte, 2010). The tsunami was responsible for the death of nearly 500 people and caused extensive destruction along the Chilean coastal zone. Maximum run-up reached a height of 19 meters on the cliffs near the generating area but there was also major impact on bays and river mouths - like that of Maule river - where local coastal villages were swept away by the giant waves (Lagos, 2010).

The Pacific Tsunami Warning Center (PTWC) in Honolulu, Hawaii issued a tsunami warning and countries like Ecuador, USA (Hawaii) and Japan - among others – and people were evacuated to higher ground. Because of the warning, there was not any loss of life elsewhere in the Pacific due to this tsunami, in contrast to the many deaths caused in Hawaii, Japan and elsewhere in the Pacific by the tsunami generated by the giant 1960 Chilean earthquake (Mw=9.5) when the warning system was still in its infancy.

Comparison of the 2010 and 1960 Chilean tsunamis indicated substantial differences in source mechanisms, energy release, ruptures, spatial clustering and distributions of aftershocks, as well as in geometry of subduction and extent of crustal displacements on land and in the ocean – which could also account for energy trapping and differences in far-field effects (Pararas-Carayannis, 2010).

Shortly after the earthquake the U.S. National Oceanic and Atmospheric Administration (NOAA) issued the map shown in Fig. 1, which shows the tsunami's propagation and arrival times in hourly increments as well as estimated wave amplitudes in centimeters. As shown, the tsunami's travel time to the Galapagos was 6 hours with estimated height of 40 cm and for the coast of Ecuador about 5 hours with a height estimated at 20 cm.

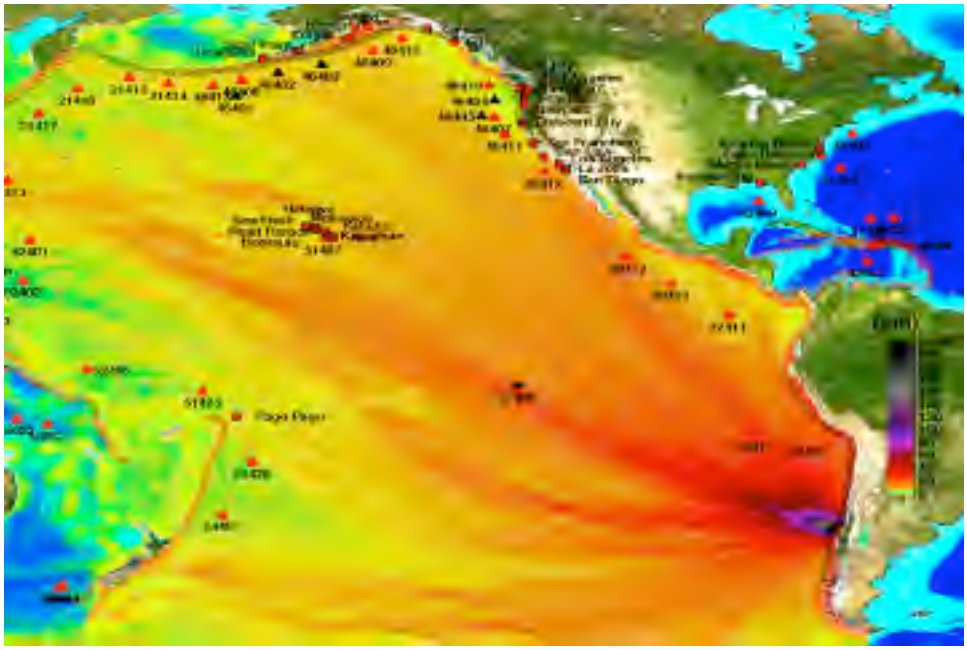

Fig. 1 Propagation map of the Chilean tsunami of 27 February 2010 across the Pacific Basin issued by U.S. - NOAA. The brown lines are travel times and the colors show energy focusing and estimated tsunami wave amplitudes.

2. OBJECTIVE

Given this background of the tsunami, the objective of the present study was to analyze the tide gauge records at five coastal ports along Ecuador and of two more records from the Galapagos Island in order to understand the behavior of the tsunami in both geographical areas and particularly for each port in order to arrive at conclusions that would allow the National Secretary for Risk Management (SNGR Spanish acronyms), the local governments and local universities to adopt prevention, and mitigation measures that would help reduce future casualties and property damage.

3. DATA COLLECTION AND FILTERING

The Instituto Oceanográfico de la Armada (INOCAR) of Ecuador maintains a network of tide gauges along its continental coast and in the Galapagos Islands. Specifically tide gauges exist at ports in Esmeraldas, Manta and La Libertad, as well at Bahia de Caraquez at the Chone River estuary and Puerto Bolivar at the Jambeli Archipelago. Tide stations in the Galapagos Islands are located at the Aeolian Inlet (Baltra Island) and at Academy Bay of Puerto Ayora (Santa Cruz Islands). Sea level records of the already mentioned ports are included in the present paper. Table 1 shows details on the locations of all these gauges that recorded the 27 February 2010 Chile tsunami.

Table 1. Tide gauges locations on the continental coast of Ecuador and at the Galapagos Archipelago

PORT	LATITUDE	LONGITUDE	CHARD/EDITION	COMMENTS
Esmeraldas	00-57-29 N.	079-38-46 W.	IOA-10010/2010	Main Pier (APE).
Bahía de Caráquez Chone Estuary	00-36-26 S.	080-25-22 W.	IOA-1031/2007	Río Chone Estuary County Pier
Manta	00-55-53 S.	080-43-18 W.	IOA-10401/2008	Main Pier (APM).
La Libertad	02-13-04 S.	080-54-23 W.	IOA.10520/2008	Main Pier (SUINLI).
Puerto Bolívar Jambeli Estuary	03-15-35 S.	080-00-05 W.	IOA-10811/2006	Jambelí Estuary, Estero Santa Rosa, Main Pier (APPB).
Baltra Island Galapagos.	00-26-06 S.	090-17-06 W.	IOA. 20213/2011	Aeolian Inlet, Navy Pier
Santa Cruz Island Galapagos.	00-44-48 S.	090-19-00 W.	IOA-20310/2009	Academy Bay, Navy Pier

Each record was statistically filtered and an assessment was made on astronomical effects, atmospheric pressure, Kelvin and storms waves that may have affected the recordings. Based on this assessment it was concluded that these had minimal or no effect. Neither the Chone estuary nor the Estero Santa Rosa had any significant inflow of fresh water to influence the recording. Furthermore there was no impact of spring tide such as the one which occurred a month later on March 28 when the moon was full. Therefore, the records of the above mentioned tide stations represented almost pure oscillations generated by the tsunami.

4. ANALYSIS

Table 2 shows the arrival time of the first tsunami crest at each tide gauge station and the time of low water for Saturday, 27 February 2012 for each of the seven ports - as predicted by the tide table issued by INOCAR. Also, the same table includes the amplitudes and periods of the tsunami generated oscillations as recorded by the mareographs (Figures 2 and 3). From the analysis of the records, it is established that the first tsunami wave crest at three stations along the Ecuadorian coast arrived after low water, while at Bahía de Caraquez and Puerto Bolívar; the first oscillation enters both estuaries before low tide. The time delay in arrival may be the result of natural hydraulic estuarine conditions.

Table 2. Details of the tsunami arrival. LW: Low water (Tide table 2010) R: Zone Time 5 S: Zone time 6.

PORT	ARRIVAL TIME	TIME LW	AMPLITUDE (cm.)	PERIOD (min.)
Esmeraldas	09H30 R	08H28R	20-30	120
Bahía de Caráquez	08H30 R	08H56R	30-50	60-120
Manta	10H00 R	08H35R	25-30	90-120
La Libertad	08H50 R	08H38R	35-70	120-150
Puerto Bolívar	09H00 R	O9H24R	35-50	60-110
Isla Baltra	07H00 S	07H28S	25-35	30-60
Isla Santa Cruz	07H00 S	07H28S	25-35	30-60

The first wave recorded at the port of Manta (located between Esmeraldas and La Libertad) shows arrival at 10:00, almost an hour later than at La Libertad to the south and half an hour later than at Esmeraldas to the north. However, all tide gauges at all ports recorded oscillations with periods ranging from 90 to 150 minutes and amplitudes ranging from 20 to 70 cm. The inconsistency in arrival times could be due to effects of refraction and diffraction, which can be attributed to local bathymetry and coastal geomorphology. Manta is located on an east – west trending coastline and faces north, while La Libertad is located in the interior of Santa Elena Bay. Therefore, waves coming from the south would have to refract considerably before arriving at both ports. Also, it should be noted that the tide gauge record at La Libertad of the 1960 Chilean tsunami showed amplitudes and periods of 1.54 m. and 36 minutes respectively (Rizzo 1977) and it also occurred at low water.

At Puerto Bolívar, the tsunami crest arrived at 09:00, before low water and had periods of 120 minutes and amplitudes of 35 cm. After mid-day, three additional peaks with shorter periods and amplitudes were recorded but it appears that these were in response to local conditions – since the estuary has a west and north mouth and waves can enter in and out from both sides. At Bahía de Caráquez, the initial crest is recorded at 08:30 with similar periods and amplitudes as in Puerto Bolivar, but they both decreases as the day goes on and this behavior may respond to the own estuarine hydraulics and morphology.

At the Galápagos Islands, the first tsunami peak occurred at 07:00, half an hour before low water. The oscillations were of shorter periods and amplitudes than those recorded along the coasts of

Continental Ecuador. However, at Academy Bay at Puerto Ayora on Santa Cruz Island in the Galapagos, in the next hour after the first tsunami wave arrived, there were sea level oscillations, which caused yachts and small boats to seat on the rocky bottom of the harbor (Tagle, 2010). When the third wave arrived at this port in the subsequent hour, all boats were once again floated and by 09:00 sea level oscillations were of shorter amplitudes and periods - probably due to the tsunami or to local resonance response of the bay or perhaps to both. By midnight sea level activity returned to normal at Academy Bay.

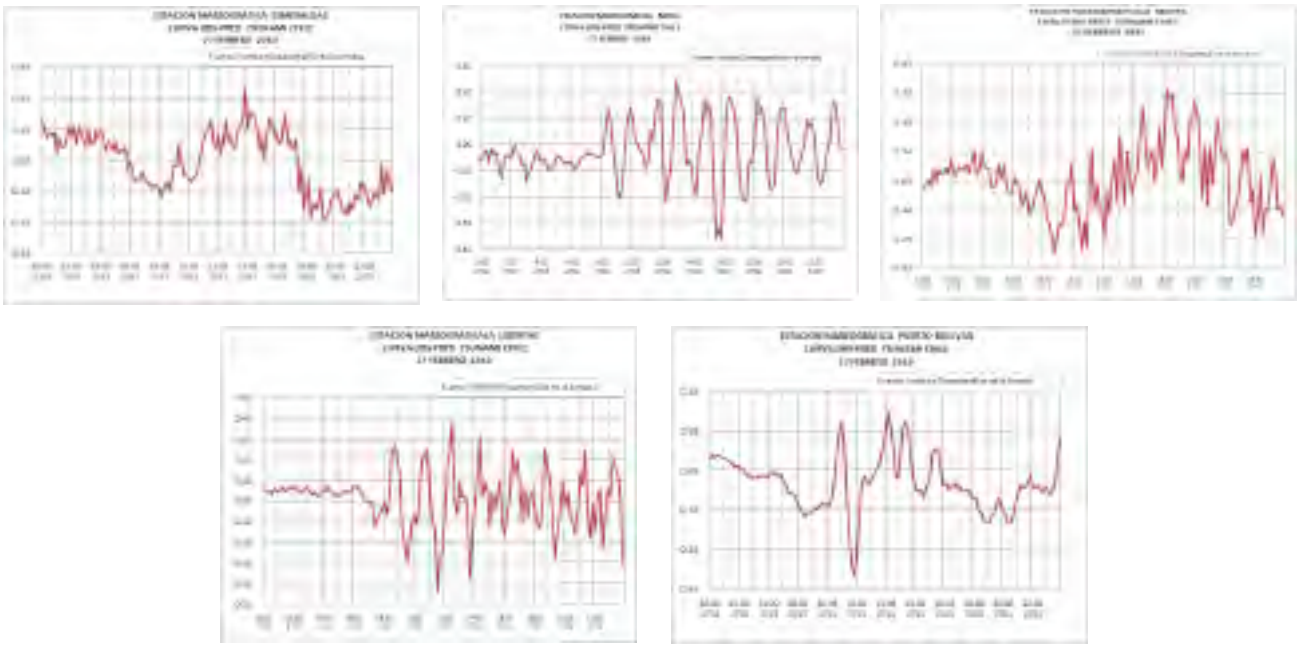

Figure 2. Mareograms from the continental ports of Ecuador where the astronomical tide has been filtered, thus records show tsunami oscillations only. Amplitudes and periods differ because of each port's geometry and morphology (for details see text).

From what is known, trained tsunami observes along coastal areas of continental Ecuador reported fairly accurately on the stage of the astronomical tide and distinguished the subsequent superimposed sea level variations after tsunami arrival. However, such superimposition on sea level by the tsunami may have gone unnoticed by amateur observers. This was not the case in ports of the Galapagos Islands, such as Academy Bay in Puerto Ayora, where shorter tsunami periods and wave amplitudes allowed better observations of strong incoming and outgoing currents to the extend that anchored boats just seated for a while on the rocky bottom. Fortunately, the prevailing low tide at the time prevented major flooding or property damage of the coastal zone. Also, proper evacuation of the people to higher ground ensured their safety.

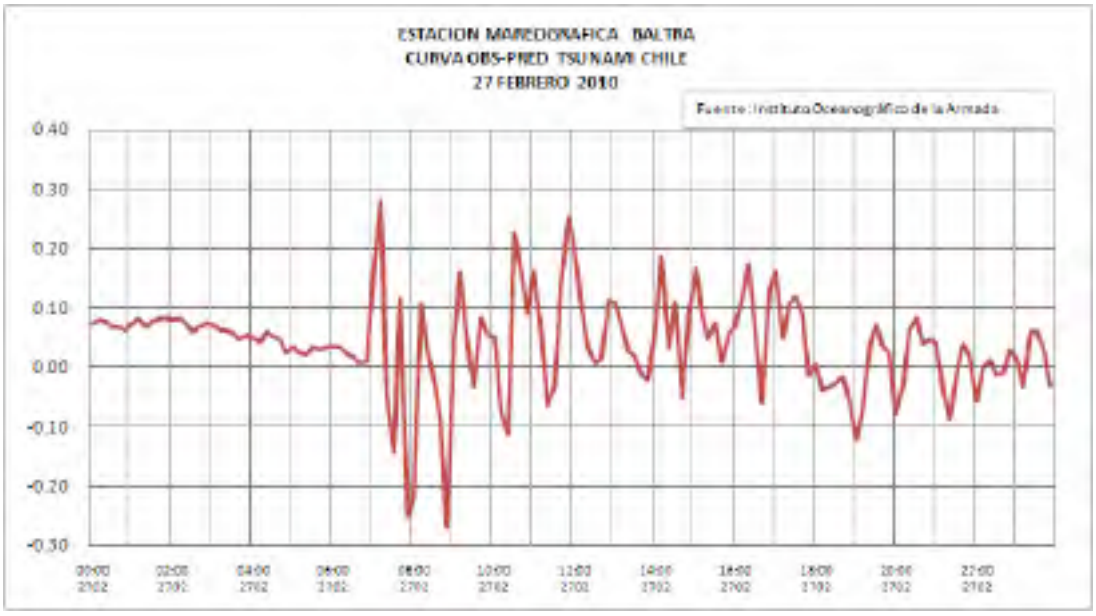

Figure 3: Mareogram of the Baltra Island tide gauge (at the Aeolian Inlet) in the Galapagos with astronomical tide filtered out. Note that amplitudes and periods are shorter from those recorded by tide stations on the continent. Stability of sea level was attained near midnight. For details see text.

5. DISCUSSION

Fortunately, the tsunami of 27 February 2010 generated in Chile did not have a major impact along the coasts of continental Ecuador and of the Galapagos Islands for the following reasons:

Because of the great distance from the source region, it took from 5 to 6 hours for the tsunami to reach the mainland Ecuadorian coast and the Galapagos Islands. Thus, there was sufficient time for officials of the National Secretary for Risk Management to adopt the necessary safety measures and issue a warning for evacuation of the people at Puerto Ayora (Santa Cruz Island in the Galapagos) to higher ground, while at the country's continental coast, the Comités de Operaciones de Emergencia (COE) kept a close watch as the event was evolving.

The timely regional tsunami warning issued by the Pacific Tsunami Warning Center (PTWC) based on data from coastal stations and DART buoys, helped the National Agencies for Risk Management to act promptly and effectively in Ecuador.

The United States Geological Survey (USGS) provided at its web page reliable data and seismic records that were useful in assessing the tsunami risk.

The fact that the tsunami struck the continentals Ecuadorian coast and the Galapagos Islands just before or after low water, limited damage to only a few boats at Academy Bay but no major damage or loss of life were reported anywhere.

In evaluating tsunami vulnerability, a point of concern is that water masses in bays, estuaries and inlets can be affected by tsunami oscillations, thus resulting in secondary undulations and energy trapping based on natural modes of oscillation (resonance effects), local bathymetry and coastal configuration in each case. Such interaction in enclosed or semi-enclosed bodies of water could have significant impact on run-up, particularly if the tsunami occurred during high tide. For such occasions where such interaction occurs, the risk of flooding and damage increases and a numerical simulation model may help understand wave behavior and potential impact – thus help in taking better mitigation measures. Such study showing tsunami transformation into a resonant oscillation or seiche was carried out for Monterey Bay (Breaker et al, 2011).

The tsunami of 27 February 2010 confirmed a conclusion by another study (Espinoza1990) that less dangerous tsunamis to the Ecuadorian maritime zone are those from distant sources and that the more dangerous are local tsunamis - such as the one generated by the great 31 January 1906 earthquake along the Esmeraldas coast near the Yaquina Transform Fault or the Manglares Basin (Collot, et al., 2009). Until recently the 1906 event was considered to be one of the six strongest earthquakes of the last century.

Great tsunamigenic earthquakes usually occur along certain regions along active subduction zones, characterized by great trenches. The tsunamis that are generated can have a destructive far-field impact in the entire Pacific Basin. Examples of such great tsunamigenic earthquakes are those of 1960 (Mw=9.5) and of 2010 (Mw=8.8) along the southern segment of the Perú-Chile trench, and of the 1964 Alaska earthquake (Mw=9.2) along the eastern end of the Aleutians trench (Ryan, Huene & Kirby. 2012). Other active subduction zones along the Japanese coast and the Mariana Islands are known to generate tsunamigenic earthquakes of varied magnitude. Ecuador is vulnerable to such great tsunamis of distant origin – particularly if they arrive during high tide or in conjunction with in-situ storm waves. In such cases, flooding and destruction would be much greater. Also, Ecuador vulnerable to local destructive tsunamis generated from earthquakes sources mostly located along the Peru-Chile trench, the Yaquina Transform Fault, the submarine canyons on the continental margin and at the Galapagos Hot spot.

The ocean bottom morphology of Ecuador's continental margin, the Galapagos Hot Spot and Platform and the Carnegie Ridge and their potential for the generation of tsunamigenic earthquakes have been reviewed and assessed (Goyes, 2009; Collot, et al., 2009). There is also the potential for tsunami generation from collapse such as that of the submarine volcano Roca Redonda near Isabela Island. Tsunami waves from such volcanic sources in the Galapagos Archipelago could reach coastal region within an hour or less after generation and may be more destructive to the islands than those generated from distant events along Ecuador's maritime zone. Obviously, there is a need to research to a greater extend such tsunami source areas and develop guidelines for warning as well as for educational programs of preparedness.

6. CONCLUSIONS

Earthquake epicenter, magnitude, tsunami propagation map and geometry of ports are parameters that determine tsunami wave periods and amplitudes recorded by tide gauges. Fortunately, both the 1960 and 2010 Chilean tsunamis occurred at low tide along the Ecuadorian coast and the Galapagos Islands. However, it is possible that the next tsunami from Chile or anywhere else may arrive at high tide or perhaps coincide with a higher sea level associated with the El Niño phenomenon. Therefore, it is important that a proper assessment is made for each port using detailed topographic data to evaluate under different scenarios, tsunami run-up/backwash and consequent collateral impacts.

For such assessment, it would be helpful to study tsunami wave behavior in enclosed water bodies using mathematical model simulation under different tide conditions. Such studies could help determine if the tsunami excites each particular basin – thus causing seiches, greater inundation and higher run-up. This is a challenge for researchers to undertake with the support of SNGR and local governments.

ACKNOWLEDGEMENTS

We thank Ing. Jimmy Candell Soto, Principal at the Universidad Estatal Península de Santa Elena (UPSE) and Captain Rafael Cabello Peñafiel, Director, Instituto Oceanográfico de la Armada (INOCAR), for their unconditional support for research and the enhancement of knowledge. Also, we thank Luis A. Burbano, César Barrionuevo and Jorge Briones of INOCAR's Hydrographic Department for their suggestions and comments. We thank Jorge Espinoza for his advise in making text changes, MAE's Martha Delgado de Lara for her kind revision of the English version and Maria Caza for her patience and worthy support in preparation of this document. Finally, the authors appreciate Dr. George Pararas-Carayannis' critical reading and careful editing.

REFERENCES

Breaker, L., Murty, T., Flora, S. and Hunter, C. (2011). The Response of Monterey Bay to the 2010 Chilean Earthquake. *Journal of Tsunami Society International. 30*(1), 1-23.

Breaker, L., Murty, T., Carrol, D.and Teague, J. (2011). The Response of Monterey Bay to the Great Tohoku Earthquake of 2011. *Journal of Tsunami Society International. 30*(3), 153-162.

Cienfuegos, R. (2010). Observations on morphological changes produced by the impact of the February 27 2010 tsunami along the coastline of V-VI-VII regions. *Book of Abstracts, American Geophysical Union* 18, Chapman Conference on Giant Earthquakes and their tsunamis.

Comte, D. (2010). The 2010. Chile earthquake – Variations in the rupture mode. *Book of Abstracts, American Geophysical Union* 20, Chapman Conference on Giant Earthquakes and their tsunamis.

Collot, J., Michaud, F., Alvarado, A., Mercaillou, B., Sosson, M., Ratzov, G., Migeon, S., Calahorrano, A. & Pazmiño, A. (2009). Vision general de la morfología submarina del margen convergente de Ecuador-Sur de Colombia: Implicaciones sobre la transferencia de masa y la edad de la subducción de la Cordillera de Carnegie. En *Geología y Geofísica Marina y Terrestre del Ecuador.*

Comisión Nacional del Derecho del Mar. Argudo & Asociados Impresores, Guayaquil. 47-74
Espinoza, J. (1990). Posibles efectos de un tsunami en las costas de la Península de Santa Elena – Ecuador. Instituto Oceanográfico de la Armada.

Goyes, P. (2009). Fondos marinos de soberanía y jurisdicción del Ecuador. En *Geología y Geofísica Marina y Terrestre del Ecuador.* Comisión Nacional del Derecho del Mar. Argudo & Asociados Impresores. Guayaquil. 1-8

Lagos, M. (2010). Magnitude and impact from the 2010 Chilean tsunami. *Book of Abstracts, American Geophysical Union* 29, Chapman Conference on Giant Earthquakes and their tsunamis.

Pararas-Carayannis, G. (2010). The Earthquake and Tsunami of 27 February 2010 in Chile – Evaluation of Source Mechanism and of Near and Far-field Tsunami Effects. Science of Tsunami Hazards (STH), Vol. 29, No. 2, 2010. (pages 96-126).

Rizzo, P. (1977). Catálogo de tsunamis en la costa ecuatoriana y su región insular. *Instituto Oceanográfico de la Armada*.

Ryan, H., Von Huene, R. and Kirby, S. (2012). Tsunami Hazards to U.S. Coast from Giant Earthquakes in Alaska. *EOS, Transactions, American Geophysical Union*. *93*(19), 185-186.
Tagle, P. (2010). Tsunami en Puerto Ayora. *La Revista* 24, El Universo, 21 de marzo.

ISSN 8755-6839

SCIENCE OF **TSUNAMI HAZARDS**

Journal of Tsunami Society International

Volume 31 **Number 3** **2012**

POTENTIAL OF TSUNAMI GENERATION ALONG THE COLOMBIA/ECUADOR SUBDUCTION MARGIN AND THE DOLORES-GUAYAQUIL MEGA-THRUST

George Pararas-Carayannis

Tsunami Society International
Honolulu, Hawaii, USA

ABSTRACT

The Colombia/Ecuador subduction zone is a region where high seismic stress is presently accumulating. Statistical probability studies and GPS measurements of crustal deformation indicate that the region has an increased potential to generate in the near future a major or great tsunamigenic earthquake similar to the 1979 or 1906. Although most of the major earthquakes along this margin usually generate local tsunamis, the recurrence of a great mega-thrust, inter-plate earthquake, similar in magnitude and rupture to the 1906 event (M_w=8.8, rupture 600 km.), can generate a tsunami with destructive near and far-field impacts. To understand the potential for such destructive tsunami generation in this region, the present study examines and evaluates: a) the controlling inter-plate coupling mechanisms of the tectonic regime of the margin – including lithospheric structure deformation, sea-floor relief and the subduction or accretion of highly folded, hydrated sediments along the seismogenic zone of southern Colombia/North Ecuador; b) the seismo-dynamics and role in tsunami generation as affected by the Carnegie Ridge's oblique subduction beneath the South American continent; and c) the seismotectonic extensional processes in the vicinity of the Gulf of Guayaquil-Tumbes Basin and how the northwestward movement of the North Andes block away from the South American continent along the Dolores Guayaquil mega-thrust and the resulting strain rotation may cause sudden detachment, décollement and deformation, with the potential for local tsunami generation that may affect the Gulf of Guayaquil and other coastal areas along southern Ecuador.

Keywords: *Colombia/Ecuador Trench, subduction, tsunami, earthquake, Carnegie Ridge, Guayaquil-Tumbes Basin, Dolores Guayaquil megathrust.*

1. INTRODUCTION

Both Colombia and Ecuador have high seismicity (Fig. 1). Major and great earthquakes along the Colombia/Ecuador margin have the potential of generating destructive local and Pacific-wide tsunamis. Several large tsunamigenic earthquakes (inter-plate events) have occurred in Ecuador's subduction zone with varied rupture mechanisms (Kanamori and McNally, 1982). Subduction of the Nazca plate beneath the Ecuador-Colombia margin has produced four mega-thrust tsunamigenic earthquakes during the 20th Century (Collot et al., 2004). A great earthquake with estimated moment magnitude Mw=8.8 and a rupture of about 600 km occurred on 31 January 1906 along the Colombia/Ecuador Trench in southern Colombia and northern Ecuador. The same segment of the Colombia/Ecuador subduction zone ruptured by this event was partially reactivated by a sequence of three lesser thrust events in 1942 (*Mw* = 7.8), 1958 (*M w* = 7.7) and 1979 (*Mw* = 8.2) (Collot et al., 2004). All four quakes generated destructive tsunamis. The 1906 tsunami, because of its greater generating area, had more significant far-field effects.

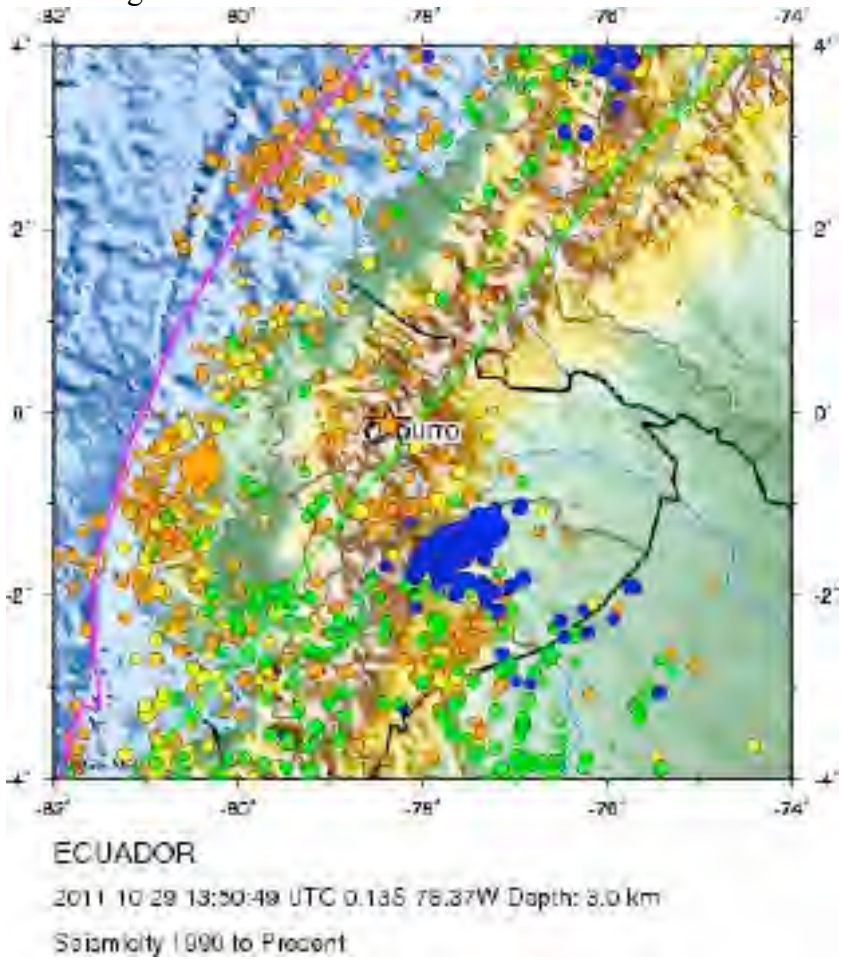

Figure 1. Seismicity of Ecuador from 1990 to present. USGS map showing the epicenter of the earthquake of 29 October 2011 near Quito, in relation to inter-plate and other intra-plate events.

The present paper provides an account of the 1906 tsunami based on a literature review and an account of the 1979 tsunamis - the latter based on an in situ survey immediately following this event (Pararas-Carayannis, 1979) and briefly discusses the 1942 and 1958 events. Subsequently, it evaluates the potential for tsunami generation along the Colombian/Ecuador margin by examining the overall controlling inter-plate coupling mechanisms of the tectonic regime along southern Colombia/North Ecuador, the seismo-dynamics and potential tsunami generation as affected by the Carnegie Ridge's oblique subduction beneath the South American continent along Central Ecuador and the seismotectonic processes in the vicinity of the Gulf of Guayaquil-Tumbes Basin that could result in an earthquake and a potentially destructive local tsunami in Southern Ecuador.

2. RECENT DESTRUCTIVE EARTHQUAKES AND TSUNAMIS

As indicated, four mega-thrust tsunamigenic earthquakes occurred in close sequence along the Colombia/Ecuador subduction margin in 1906, 1942, 1958 and 1979. More than 33 years have elapsed without another tsunamigenic earthquake in the region. Figure 2 illustrates the ruptures and focal mechanisms of these earthquakes on the inter-plate megathrust fault along the Colombia/Ecuador subduction zone.

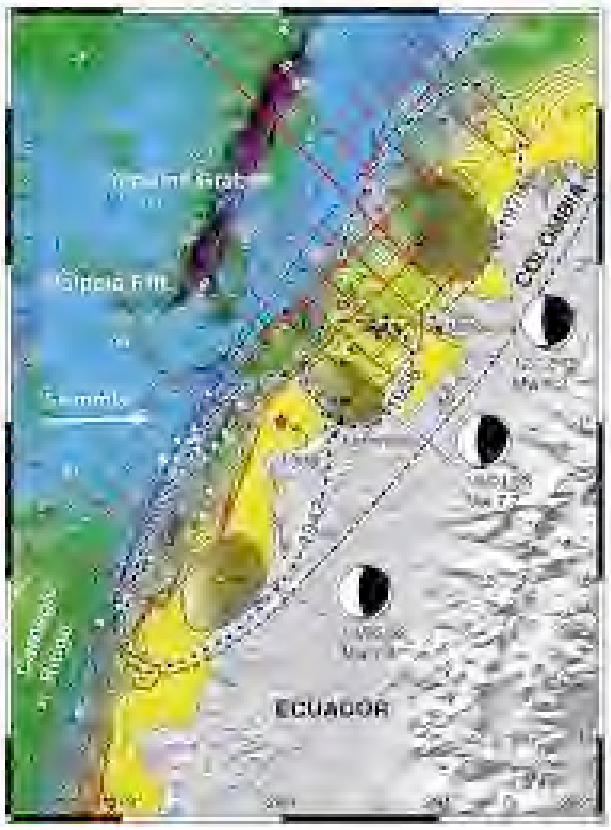

Figure 2. Tsunamigenic Earthquakes of 1906, 1942, 1958 and 1979 on inter-plate thrust faults along the Colombia/Ecuador subduction zone (after Collot et al. 2004)

Noticeable is the high rate and obliquity of subduction, the chronological sequencing of three historical events and the extent of limited ruptures due to local asperities following the great 1906 earthquake. The latter event ruptured for 600 km encompassing the ruptures of the three subsequent events (Collot et al. 2004) along the inter-plate megathrust. The following is a brief examination of these historical events and their impacts, for the purpose of evaluating future events along this complex subduction margin.

2.1 Earthquake and tsunami of 12 December 1979

This earthquake occurred at 07:59:4.3 (UT). Its epicenter was in the ocean at 1.584° North 79.386° West. Originally the magnitude was given as M=7.9 (Richter scale) but subsequently it was revised to a moment magnitude Mw 8.2. The earthquake and the tsunami were responsible for the destruction of at least six fishing villages and the death of hundreds of people in the State of Narino in Colombia Pararas-Carayannis, 1980).

Strong motions were felt in Bogota, Cali, Popayan, Buenaventura and other major cities and villages in Colombia and in Guayaquil, Esmeraldas, Quito and other parts of Ecuador. Tumaco and San Juan Island were the two areas that were mostly affected by both the earthquake and the tsunami. Esmeraldas, and other cities and villages of Ecuador close to the epicenter did not sustain much damage. Review of the structural geology indicates why the earthquake had far more severe effects in Colombia than in Ecuador. An offshore ridge in the vicinity of epicenter has an orientation in a northwest/southeast direction and may have acted as a barrier.

2.1.1 Effects of the 1979 Earthquake

The shock was felt from Bogota to the north to Quito and Guayaquil to the South. There were three major shock waves lasting from 0759 to 0804 UT. At least 10 major aftershocks were recorded subsequently. It was the strongest since 19 January 1958 when an event of 7.8 occurred in the same general area and the second large earthquake to occur in Colombia within a month. On 23 November 1979 an earthquake of magnitude M=6.7 (Richter) had occurred further north.

The quake caused most of the damage in the State of Narino in Colombia which borders Northern Ecuador. There were numerous dead and injured. Thousands of buildings were destroyed - principally in the State of Narino. Hardest hit in the State of Narino was Charco, a fishing village of 4,000 persons -- about 300 kilometers north of Ecuador. Most of the victims were women and children. Homes of at least 10,000 persons were destroyed. Electrical power and telephone lines were knocked out. The majority of casualties (at least 807) were the result of the tsunami rather than of the earthquake. Bogota and other major cities, tall buildings swayed, but damage was not significant. Preliminary reports estimated the number of persons killed in the hundreds with up to 2,000 people missing (Pararas-Carayannis, 1980).

The second populated area that was hardest hit by the quake was the town of Tumaco, only about 80

kilometers from the earthquake epicenter (Fig. 3). At least 40 persons were killed and 750 injured and approximately 10% of the houses and other buildings were destroyed. Tumaco is built on an island made up of alluvial deposits of Rio Mira and Rio Caunapi. Evidence of liquefaction was evident in many areas of the city where structures failed and particularly evident along the waterfront. Evidence of subsidence was found on either side of the bridge connecting the island where Tumaco is situated to the island where the airport is located.

Figure 3. Earthquake damage at Tumaco, Colombia (photo by G. Pararas-Carayannis**)**

The island dropped by as much as 60 centimeters. Evidence of subsidence of about 60 centimeters also was reported from the island of Rompido, offshore from Tumaco, and a good portion of that island was under water. Subsidence of approximately 50 centimeters was reported from Cascajal Island (Pararas-Carayannis, 1980). Surprisingly there was little damage at Ecuador either from the earthquake or the tsunami.

2.1.2 The 12 December 1979 tsunami

The rupture of the 12 December 1979 earthquake was about 200 km along the Northeastern inter-plate segment of the Colombia-Ecuador tectonic boundary – thus the generating area of the destructive local tsunami was at least that long and about 80 km wide as shown in Figure 2. As stated, this segment was the third to rupture in sequence along the megathrust and generate a tsunami, following the segments ruptured by the 1942 and 1958 earthquakes along the same fault. All three of these

quakes involved three different segments – all of which had been ruptured previously by the 1906 earthquake. Apparently, localized asperities had limited the ruptures of the 1942, 1958 and 1979 earthquakes and their size of the tsunami generating areas. However, the 1906 quake had packed a lot more energy and broke all three segments in succession for a total length of 600 km, thus generating a much more destructive tsunami locally - but also one with significant far field impact. Figure 4 is another illustration of the aftershocks and extent of ruptures of the tsunamigenic earthquakes 1906, 1942, 1959 and 1979.

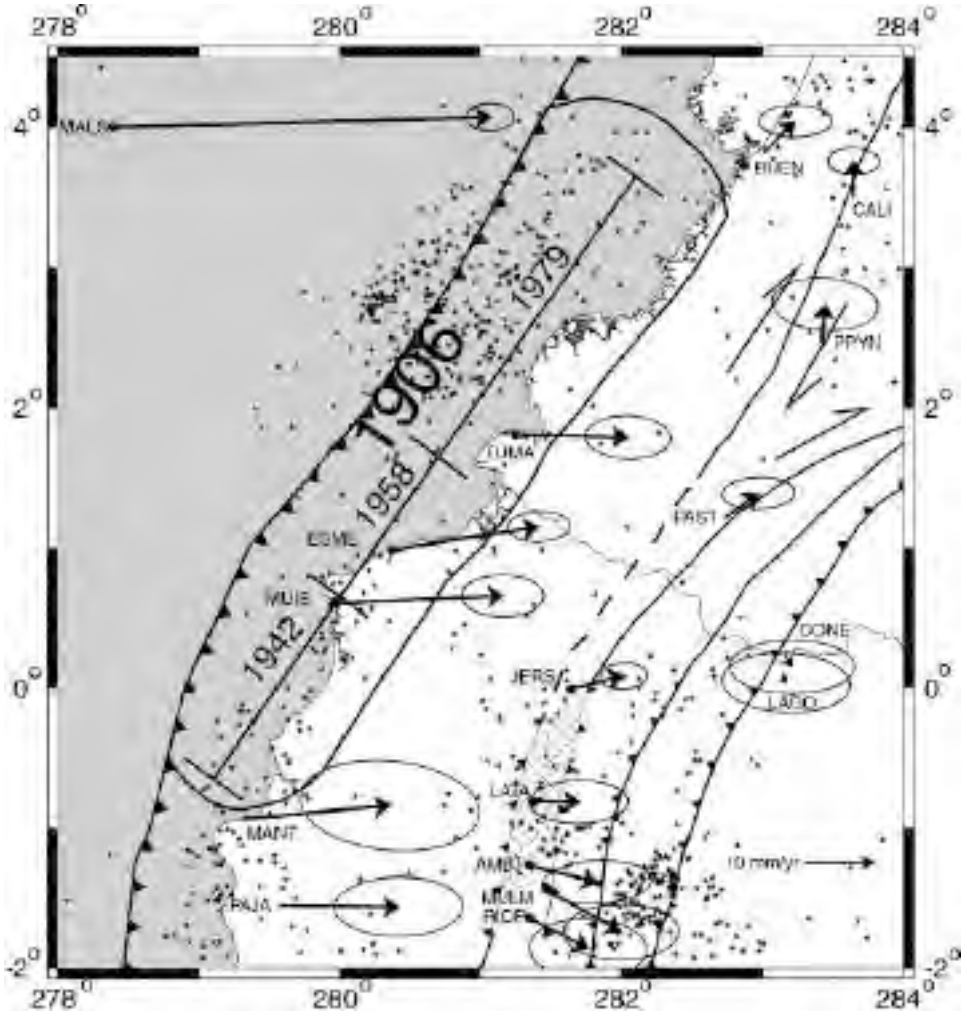

Figure 4. Ruptures of the Earthquakes 1942, 1959 and 1979 Earthquakes. Note that the 1906 earthquake rupture was over 500 km long and included those of the subsequent earthquakes (after Kanamori and McNally, 1982).

2.1.3 Near-field Effects of the 12 December 1979 tsunami

Approximately 30-35 kilometers of the coast were hardest hit by the tsunami, while the length of the area hardest hit by the earthquake was approximately 225 kilometers in length, from Guapi to Tumaco. Fishing villages that were destroyed were Curval, Timiti, San Juan, Mulatos and Iscuande. Most of the damage and deaths in these villages were the result of the tsunami (Pararas-Carayannis, 1980). Figure 5 shows tsunami damage at Tumaco.

A total of four waves were observed, the first wave arriving approximately 10 minutes after the main quake. The water recessed first to about 3 meters below the level of the sea. The third wave was largest. San Juan Island was approximately 5 meters above the level of the tide, which fortunately, was at its lowest at that time. The tsunami wiped out many villages. Most of the houses at Charco and Iscuande were destroyed. Hardest hit was the fishing village of San Juan, where the waves completely overran the island destroying just about everything in their path. Numerous deaths were reported from this area.

Figure 5. Tsunami damage at Tumaco (photo by G. Pararas-Carayannis**)**

Figure 6 is a hand trace of the tsunami as recorded by a tide gauge at the port of Esmeraldas in Ecuador, approximately 95 nautical miles to the south of the epicenter. The record confirms that the tsunami arrived at the lowest possible tide and that the first wave activity was a recession followed by approximately 3 to 4 waves. No major tsunami damage occurred in Tumaco (Colombia) or Esmeraldas (Ecuador), but had the wave occurred at high tide, it is believed that flooding and

considerably more tsunami damage would have occurred at these two cities. If the wave had occurred at high tide, its elevation would have been 1-3 meters higher than the one-meter wave observed in Tumaco and could have resulted in extensive tsunami damage of that city where the maximum elevation is only 3 meters above sea level.

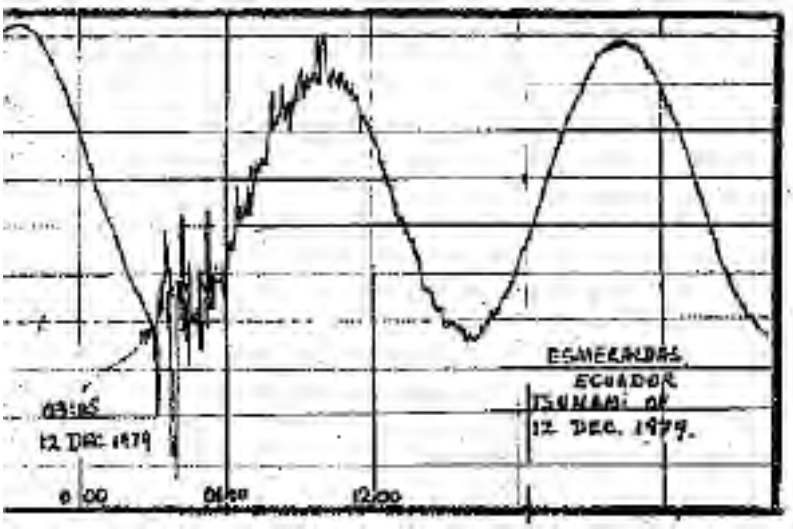

Figure 6. Hand-trace of the mareographic record of the 1979 tsunami as recorded at Esmeraldas, Ecuador. Based on this record, it appears that the travel time to that tide station was only 5-6 minutes after the quake (after Pararas-Carayannis, 1980).

At San Juan Island, where maximum waves were observed, the direction of approach of the waves was from the southwest, rather than from the west. The direction of wave approach was obtained by observing fallen palm trees, detritus material wrapped around objects and the way buildings had moved or structurally failed (Pararas-Carayannis, 1980).

2.1.4 Far-Field Impact of the 1979 Tsunami

The tsunami was observed or recorded in many places of the Pacific including the Hawaiian Islands. A deep gauge off the coast near Tokyo, Japan did not record any wave activity. However, at Johnston Island the recorded wave was only 8 cm. It took a little over 12 hours to reach the Hawaiian Islands. At Hilo and at Kahului, the maximum observed wave (trough to crest) was approximately 40 centimeters. At Nawiliwili the wave was only 10 cm.

2.2 The 31 January 1906 Earthquake and Tsunami

A great earthquake occurred at 15:36 UTC on 31 January 1906, off the coast of Ecuador and Colombia. Its epicenter was near the port town of Esmeraldas in Ecuador (Fig. 7). Its magnitude (Richter) was originally estimated at 8.2, but subsequently revised to a Moment Magnitude M_w=8.8.

A destructive tsunami was generated which destroyed 49 houses and killed at least 500 people on the coast of Colombia and perhaps as many as 1500 people.

The quake's rupture was estimated at 500–600 km long and – as reported earlier - encompassing the rupture segments of earthquakes which occurred subsequently in 1942, 1958 and 1979. The width of each affected block was estimated at about 80-90 km. The lack of overlap between the three subsequent events suggested the presence of minor barriers (asperities) to rupture propagation along the plate boundary. Although these three events ruptured the same area of the plate boundary overall, they released only a small fraction of the energy of the 1906 earthquake. The ground motions of the 1906 quake were felt along the coast of Central America, as far north as San Francisco and as far west as Japan. The quake was recorded at San Diego and San Francisco in California.

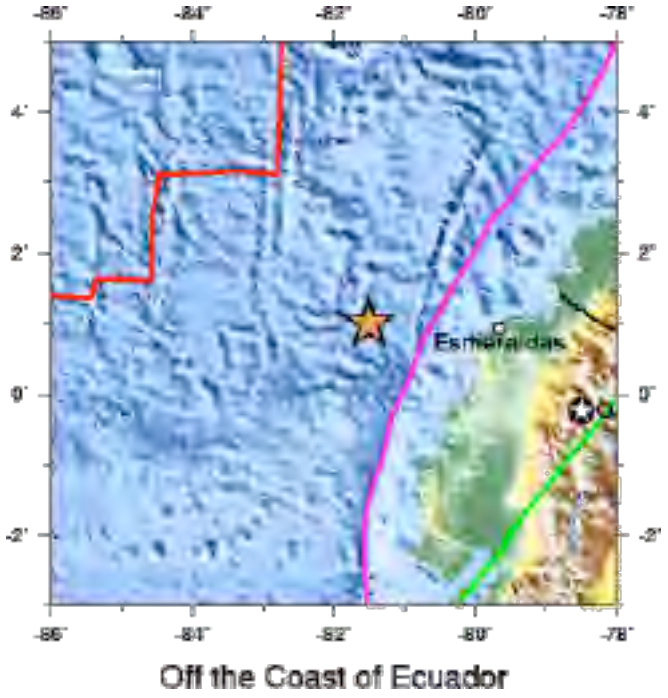

Figure 7. Epicenter of the 31 January 1906 earthquake off the coast of Ecuador near the city of Esmeraldas (modified USGS map).

2.2.1 Near and Far-field Effects of the 1906 Tsunami

Near Field Impact - The maximum recorded run-up height was 5 m in Tumaco, Colombia. The greatest damage from the tsunami occurred on the coast between Rio Verde, Ecuador and Micay, Colombia. Estimates of the number of deaths caused by the tsunami vary between 500 and 1,500.

Far-field impact – The tsunami was observed in Costa Rica, Panama, Mexico, California and Japan. However, there were no reports of tsunami damage from Central America or Mexico. At Acapulco, the recorded maximum tsunami height was .25 meters.

In the Hawaiian Islands the first tsunami wave arrived in Hilo, Hawaii, about 12.5 hours after the earthquake. It flooded the floor of the old wharf at the end of Waianuenue Street and the railroad tracks between there and Waiakea. The wave oscillations ranged up to 3.6 m (1.8 m. run-up height) and had average periods of 30 minutes. The channels of the Wailuku and Wailoa Rivers alternately dried up, then were flooded. In Kahului, Maui, three waves were observed with an average period of about 20 minutes. The second wave was larger and the third even larger. Sea level rose about 0.30 m above the mean sea level mark. According to other sources, the water surface rose to the level of the old steamship pier and the road running along the coast. In Honolulu, Hawaii, the tide gauge began registering water level oscillations at 3:30 UTC on 1 February - about 12 hours after the earthquake. The first wave appeared to be positive. At 4:15 UTC there was an extremely great ebb of the sea. The highest of the waves was the fourth reaching 0.25 m. The period of the tsunami waves ranged from 20-30 minutes. Three separate trains of oscillations were registered. (Pararas-Carayannis, 1980; Lander and Lockridge, 1989).

3. SEISMODYNAMICS OF THE ECUADOR-COLOMBIA SUBDUCTION MARGIN

Seismic investigations of lithospheric structures associated with subduction megathrusts are critical to understanding the mechanics of the inter-plate seismogenic zone, where very destructive, tsunamigenic earthquakes occur. Several factors have been proposed as controlling inter-plate coupling and tectonic regime of the Ecuador-Colombia margin, including sea-floor relief and the subduction or accretion of high-fluid content sediments which, when suddenly displaced, can enhance the height of tsunamis.

Furthermore, the length of earthquake ruptures and the dimensions of tsunamigenic sources are affected by buoyancy forces of bounding and migrating oceanic ridges and fractures, subducting obliquely with the South American continent. For example, in central and southern Peru, from about 15^0 to 18^0 South, the Mendana Fracture Zone (MFZ) to the North and the Nazca Ridge to the South, have created a narrow zone of considerable geologic and seismic complexity - characterized by shallow earthquakes that can generate destructive tsunamis of varied intensities. The obliquity of convergent tectonic plate collision in this region, as well associated buoyancy, may be the reason for the shorter rupture lengths of major earthquakes and the generation of only local destructive tsunamis (Pararas-Carayannis, 2012). The seismotectonics of the Ecuador-Colombia boundary margin are analogous in that they are affected also by the buoyancy forces of the obliquely subducting Carnegie Ridge under central Ecuador. These forces have created fault heterogeneities that affect tsunami source dimensions and mechanisms of generation to the north and to the south of Carnegie Ridge's region of subduction.

Before discussing the localized earthquake mechanisms that generate tsunamis along the megathrust north of the Carnegie Ridge – the region which parallels the Ecuador-Colombia trench - we must first review how the larger tectonic kinematics affect the North-Western region of the South American

continent. The overall seismo-dynamics along the coasts of Ecuador and Colombia are affected by the active seismicity and kinematics of the northernmost segment of the Andes - which is divided into a Western Cordillera and an Eastern Cordillera (including the Merida Andes) (Fig. 8). This wedge is referred to as the ‘‘North Andes block’’ and inferred from geologic and seismicity data.

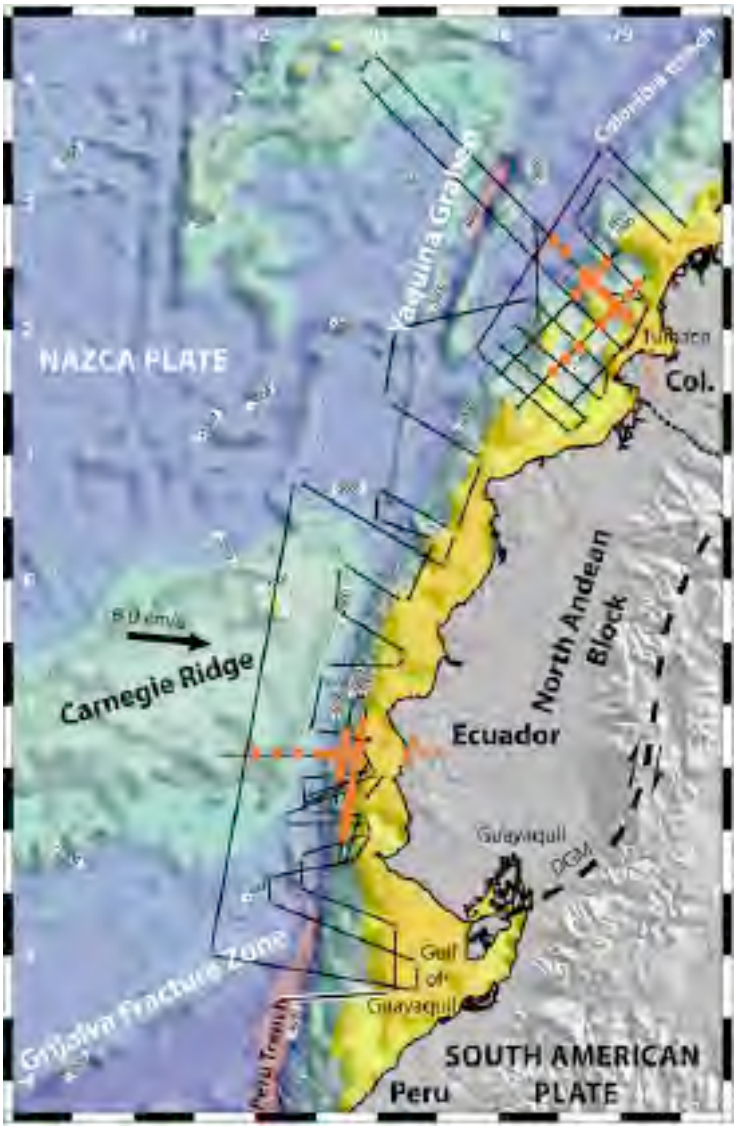

Figure 8. Yaquina Graben, Colombian Trench, Carnegie Ridge, the Grijalva Fracture Zone, the North Andean Block and the Dolores Guayaquil megathrust (DGM). Epicenters of the 1979 earthquakes on the North Andean Block coastal intra plate region (after Collot et al. 2004).

This wedge appears to move at about 10 mm/year toward 055 with respect to South America (SA), or at about 17–19 mm/year northwestward with respect to Caribbean tectonic plate (CA). The boundary

between the North Andes plate (ND) and the South America plate (SA) is the Dolores Guayaquil mega-thrust (DGM), which is apparently reactivated in an oblique dextral-normal sense. DGM transverses the Gulf of Guayaquil and has created a pull-apart basin and resulting strain rotation which may cause sudden crustal detachment, deformation and décollement, with the potential for local tsunami generation that may affect the Gulf of Guayaquil and other coastal areas along southern Ecuador.

To understand the tsunami generation mechanisms along the Colombia/Ecuador subduction margin north of the Carnegie Ridge, we must first review the seismo-dynamics of the region from latitude 1^0 to 4°N and longitude 77^0 to 80°W, where the highest seismicity has been observed in recent years, as well as the impact of oblique subduction of larger tectonic features. As indicated, several large tsunamigenic earthquakes (all inter-plate events) occurred in 1906, 1942, 1958 and 1979 along the Ecuador/Colombia subduction zone, north of the subducting Carnegie Ridge.

3.1 Examination of Sequential Ruptures Associated with Recent Historical Earthquakes along the Colombia-Ecuador Coast – Implications for Future Events.

As reported, subsequent earthquakes to the 1906 event along the same zone, on 14 May 1942, 19 January 1958 and 12 December 1979, ruptured consecutive segments, apparently limited in length by asperities cutting across the mega-thrust fault that parallels the Colombia/Ecuador trench. Figure 9 is another illustration of the ruptures of these tsunamigenic earthquakes.

The epicenter of the 1942 Ecuador earthquake was in close proximity to the northern flank of the Carnegie Ridge. This quake's moment release occurred in one simple pulse near the epicenter in 22 seconds. The relocated aftershocks distributed over an area parallel to the trench that was approximately 200 km long and 90 km wide. The majority of the aftershocks occurred north of the epicenter. The seismic moment as determined from the *P* waves was $6–8\times10^{20}$N·m, corresponding to a moment magnitude of 7.8–7.9. The reported location of the maximum intensities (IX) for this event was south of the main epicenter (Sennson & Beck, 1996). The 1958 earthquake occurred immediately north of the 1942 event and was also tsunamigenic and destructive in both southern Colombia and Ecuador.

The nature of fault heterogeneities that controlled the northward propagation of plate-boundary rupture from the source region of the earthquake of 1942 to the source region of the 1958 earthquake and eventually to the source region of the earthquake of 1979, were examined with the method of Joint Hypocenter Determination (Mendoza & Dewey, 1984). This examination determined that the relocated hypocenters lie on the same plane to within the approximately 20-km uncertainty of the focal depths. Also, the main shocks apparently nucleated at nearly the same distance from the Ecuador-Colombia trench. Based on such observations, it was suggested that the heterogeneities between the 1942 and 1958 ruptures and between the 1958 and 1979 ruptures do not correspond to a major distortion of the down-going crustal slab but rather to either minor distortions of the slab or to regions of high friction or low available strain energy on a continuous fault surface.

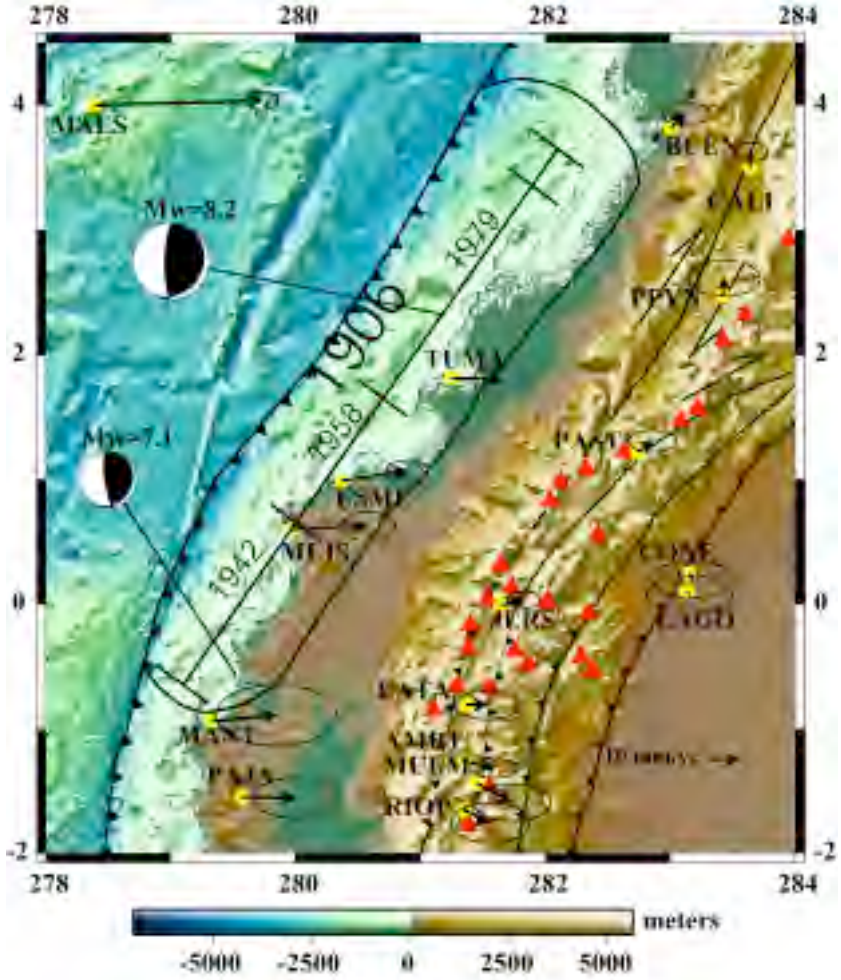

Figure 9. Ruptures of the 1906, 1942, 1958 and 1979 tsunamigenic earthquakes (after Trenkamp et al. 2002)

More specifically it was observed that the heterogeneity between the 1958 and 1979 rupture zones seemed to have been a high-strength barrier (asperity) with dimensions much smaller than the dimensions of either of the rupture zones. Both the 1942 and 1958 earthquakes had source dimensions no larger than the 1979 main shock, but had stronger aftershock sequences than the 1979 event. Based on this observation it has been suggested that the stoppage of the earthquake rupture in 1979 left the plate-boundary segment that had ruptured in 1906 in a state of lower stress than it had been following the 1942 and 1958 earthquakes. Long-term seismicity in the decades preceding the 1979 earthquake occurred mostly outside or on the boundaries of the rupture area defined by the distribution of 1979 aftershocks. The intense aftershock activity that followed the 1958 main shock within tens of kilometers of the eventual 1979 hypocenter was attributed to a long-term precursory seismic swarm for the 1979 earthquake (Mendoza & Dewey, 1984).

Similarly, recent results from Global Positioning System (GPS) measurements show deformation along the coast of Ecuador and Colombia that can be linked to the rupture zone of the 1979 earthquake in 1979 (White et al., 2003; Trenkamp et al., 2002). The observed wide plate boundary deformation in Ecuador - as determined by the GPS measurements - has been explained by 50% apparent locking on the subduction interface. Although there have not been any historic large earthquakes (Mw >7) south of the 1906 earthquake rupture zone, 50% apparent elastic locking is necessary to model the deformation that has been observed there (White et al., 2003).

In Colombia, only 30% apparent elastic locking is occurring along the subduction interface in the 1979 earthquake rupture zone (Mw 8.2), and no elastic locking is necessary to explain the crustal deformation observed at two other GPS sites (White et al., 2003). There is no evidence from seismicity or plate geometry that plate coupling on the subduction zone is reduced in Colombia. However, simple visco-elastic models suggest that the apparent reduction in elastic locking can be explained entirely by the response of a viscous upper mantle to the 1979 earthquake. These results suggest that elastic strain accumulation is occurring evenly throughout this region, but post-seismic relaxation masks the true total strain rate (White et al., 2003). In other words, the total strain accumulating in the region since 1979 is difficult to estimate and indeed may be reaching a critical stage. The earthquake strain accumulation along the Ecuador/Colombia Trench has been estimated to be in the order of -26 ± 4 mm/yr due to shortening since 1991 at the coastal sites at Muisne and Esmeraldas, Ecuador, hypothesized to reflect three modes of deformation roughly parallel to the convergence direction (Trenkamp et al., 2002).

The asperities, shorter ruptures and offsets of the 1942, 1958 and 1979 earthquakes can also be supported by results of multichannel seismic reflection and bathymetric data acquired during the SISTEUR cruise (Collot et al., 2004)). This data shows evidence that the margin wedge is segmented by transverse crustal faults that potentially correlate with the limits of the earthquake co-seismic slip zones. Subduction of the buoyant Carnegie Ridge – as it will be discussed further – apparently controls some of the seismo-dynamic processes south of the margin where the 1906, 1942, 1958 and 1979 tsunamigenic earthquakes occurred.

3.3 Seismo-dynamics of the Carnegie Ridge

In between the two major tectonic regimes of Ecuador's tectonic margin - specifically between latitude 1°N and 2°S - the Carnegie Ridge collides against the South American continent in an E-W direction and subducts under central Ecuador at a relative plate velocity of 5 cm/yr (Pilger, 1983). The formation of the Carnegie Ridge and other aseismic ridges started at about 20 Ma when the Galapagos volcanoes were generated by a mantle plume hotspot, formed following the break-up of the Farallon Plate and the formation of the separate Cocos and Nazca Plates (Fig. 10). At about 19.5 Ma, the Galapagos spreading center moved so that most of the hotspot magmatism affected the Nazca Plate, forming the combined Carnegie and Malpelo Ridges. At about 14.5 Ma the spreading center jumped south, such that most of the magmatims affected the Cocos Plate and caused the Malpelo Ridge to rift

away from the Carnegie Ridge (Salares et al., 2005). The Galapagos Rise moved north again at about 5 Ma, leaving the hotspot activity within the Nazca Plate – the current situation.

It has been estimated that the subduction of the Carnegie Ridge under the South America plate started about 2 or 3 million years ago (Lonsdale 1978), while Pennington (1981) estimated an even earlier beginning. The seismicity of Ecuador and South Colombia - and therefore tsunami generation - are influenced by the Carnegie Ridge subduction under central Ecuador.

In summary, the Carnegie Ridge extends eastward over 1,000 km from the Galapagos Islands to the Colombia-Ecuador trench and continues beneath northern Ecuador for about 700 km. It consists of thickened oceanic crust. Wideangle seismic reflection and refraction data acquired over the central and eastern part of the ridge give crustal thicknesses of 13 km and 19 km respectively for crust that has estimated ages of about 11 Ma and 20 Ma.

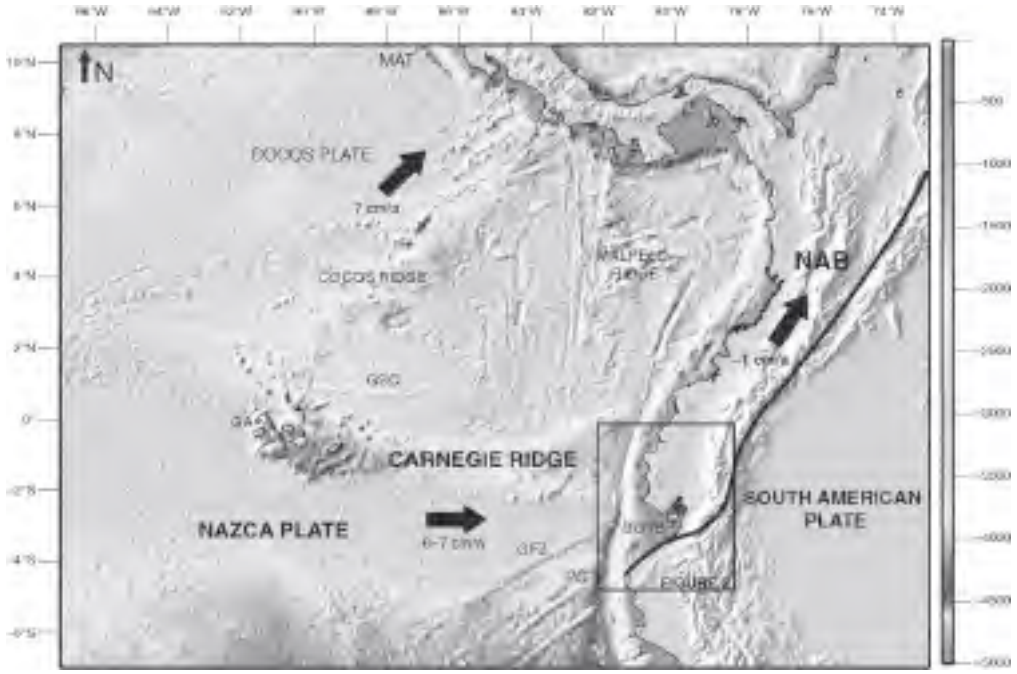

Figure 10. Subduction of the Carnegie Ridge beneath Ecuador. Convergence rates of the Cocos and Nazca plates and rate of movement of the North Andean Block along the Dolores Guayaquil megathrust (DGM) (after: Collot et al., 2004; Witt and Bourgois, 2009)

3.3.1 Influence of the Carnegie Ridge subduction.

The buoyancy of the subducting Carnegie Ridge appears to have an influence on the lithosphere of the Nazca Plate which, in its northern part, has a gentle angle of subduction and a non-uniform geometrical configuration. Where the subduction of the Carnegie Ridge takes place along central Ecuador, the trench is shallow and the coastal region is being uplifted (Fig. 11). Also, the ridge

appears to partially lock the plate interface and to limit the incidence of tsunamigenic earthquakes along central Ecuador south of 1^0 latitude. The mode of faulting and seismicity of this region may be related to the subduction of the Carnegie Ridge (Gutscher et. al., 2005). The buoyancy of the Ridge is inferred to partially lock the plate interface along central Ecuador. For example, co-seismic slip during the 1942 and 1906 earthquakes terminated against the subducted northern flank of the Carnegie ridge. Similarly, at about 2^0 North latitude, the Manglares fault which cuts transversally through the margin wedge, correlates with the limit between the 1958 and 1979 tsunamigenic earthquake rupture zones (Collot et al., 2004).

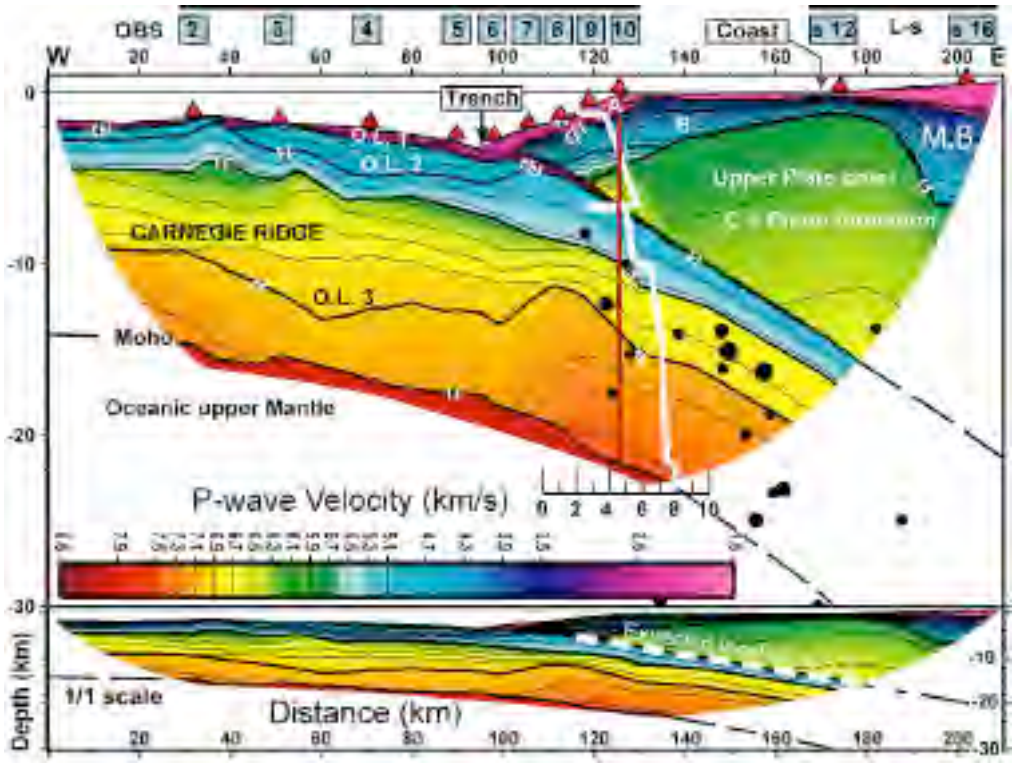

Figure 11. Subduction of the Carnegie Ridge under the continental crust along central Ecuador (from Graindorge et al. 2004 in Collot et al. 2004).

According to a recent study (Collot et al., 2004), the transversal cutting along the Colombia/Ecuador mega-thrust fault zone seems to be associated with high-stress concentration on the plate interface. Accordingly, an outer basement high, which bounded the margin seaward of the 1958 earthquake rupture zone, may also act as a deformable structure that limits seaward propagation of co-seismic slip along the mega-thrust splay fault. The cause of the 1958 tsunami is attributed to possible co-seismic uplift of the basement high. Furthermore, even weak transverse faulting reduces coupling between adjacent margin segments, together with a splay fault and an asperity along the plate interface - which presumably controlled the seismogenic rupture of the 1958 earthquake.

3.4 Seismo-dynamics of the Gulf of Guayaquil-Tumbes Basin – Potential for tsunami generation

Apparently, the collision of the Carnegie Ridge with central Ecuador has altered also the tectonic stress distribution along the southern convergent margin, resulting in the creation of numerous faults with NW-SE and NE-SW orientations. Between latitudes 2^0 and 4°S, the ocean bottom in front of the Ecuador Trench is a fractured and complex seismogenic zone, estimated to be about 230 kms in width. This region is cut by several oceanic fracture zones which have a NE-trending orientation (Fig. 12). Best known are the Grijalva, Alvarado, and Sarmiento fractures. It has been suggested that since this region is subducted under the South American continent, it may behave as a separate microplate independent of the adjacent major tectonic plates (Pennington, 1981; Hall and Wood, 1985).

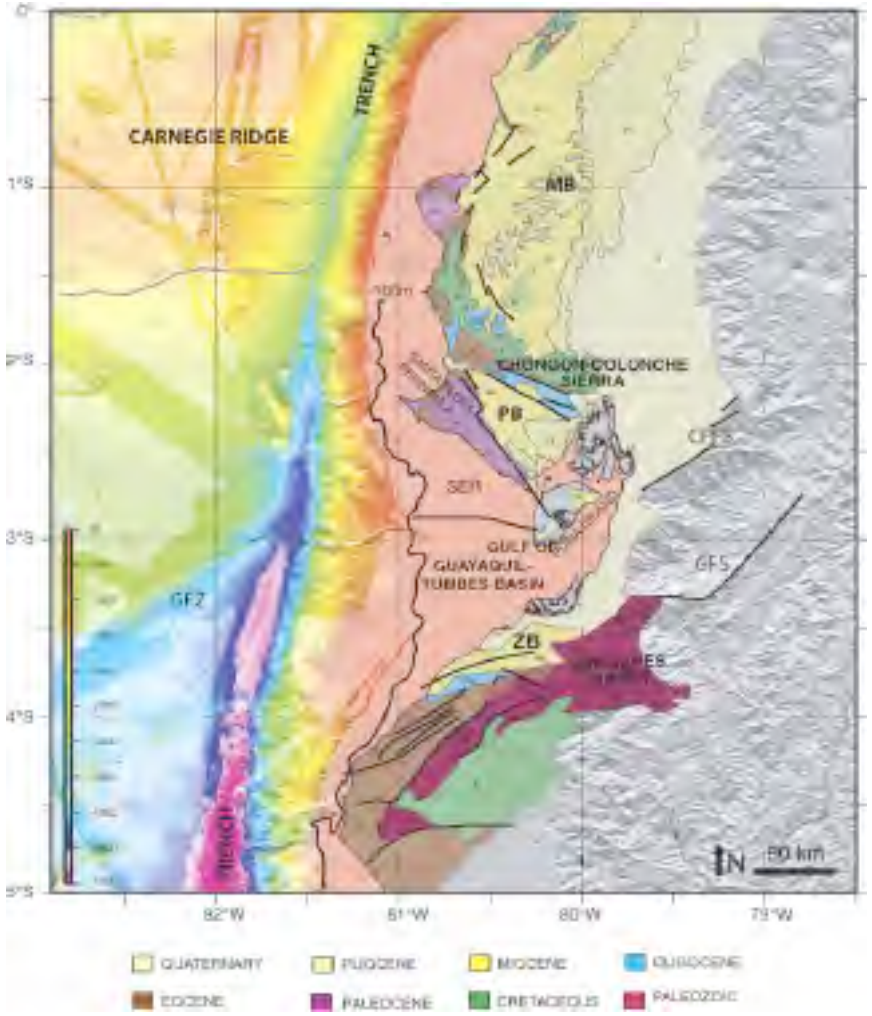

Figure 12. Faults on the southern region of the Guayaquil-Tumbes basin. Plate coupling along the subduction décollement, which controls the inward segmentation of deformation. Potential source of local tsunamis (map: Witt and Bourgois, 2009).

Such well-known fault systems with NE-SW orientation include those transversing the Gulf of Guayaquil, such as La Pallatanga and the Alausi-Guamote Valley faults, among others. Several destructive earthquakes which occurred in Ecuador – the Riobamba in 1797 and the Alausi in 1961, among others - have been correlated with these NE-SW trending faults. Major lineaments and faults with such NW-SE orientations have been also identified (Hall & Wood, 1985) as delimiting regions of tectonic segmentation, the most important being the Esmeraldas-Pastaza and the Rio Mira-Salado lineaments. Two tectonic regimes - which show different styles and ages - controlled the evolution of the southern Ecuador and northern Peru continental margin and shelf and thus the potential for the generation of tsunamigenic earthquakes. The N-S extensional regime along the shelf area is related to North Andean block drift, whereas the E-W extensional regime along the continental margin results from apparent tectonic erosion at depth.

Also, trench-parallel extensional strain resulting from the northward drift of the North Andean block – as described earlier - has controlled the tectonic evolution of the Gulf of Guayaquil-Tumbes Basin for the past ~1.8–1.6 Ma (Witt & Bourgois, 2009). Multichannel seismic and well data document that E-W to ENE, low-angle detachment normal faults, the Posorja and Jambelí detachment systems to the north and the Tumbes detachment system to the south, accommodated the main subsidence step along the shelf area during late Pliocene-Quaternary times (1.8–1.6 Ma to present) (Witt & Bourgois, 2009).

Strain rotation takes place along a major N-S–trending transfer system formed by the Inner Domito fault and the Inner Banco Peru fault, which bound the detachment systems to the west. The strike-slip component along this transfer system, roughly located at the continental margin-shelf break, evolved in response to slip along the detachment systems bounding the basin to the north and to the south.

Finally, according to recent studies (Witt & Bourgois, 2009), the Tumbes detachment system is the master fault which controlled the evolution of the basin and may represent the shallower manifestation of a reactivated subduction megathrust. This megathrust connects landward with the continental structures assumed to be part of the eastern frontier of the North Andean block. For the past ~2 Ma, the total lengthening calculated along a complete N-S transect of the Gulf of Guayaquil-Tumbes Basin ranges between 13.5 and 20 km (Witt & Bourgois, 2009). Such extend of lengthening can be justified with the documented drift of the North Andean block. However, the same studies (Witt & Bourgois, 2009) have also shown that the Gulf of Guayaquil-Tumbes Basin is not a typical pull-apart basin, but rather a certain type of basin controlled by detachments extending downward across the crust and plate coupling along the subduction décollement surface – which control the segmentation of deformation inward. Local tsunamis can be generated from such pull-apart, shallow, décollement processes in the Gulf of Guayaquil-Tumbes Basin.

3.5 Potential Tsunamis along the Colombia/Ecuador Subduction Margin

Global Positioning System (GPS) data from southern Central America and northwestern South America collected during 1991, 1994, 1996, and 1998 in Ecuador, Colombia and elsewhere (Trenkamp et al, 2002; White et al. 2003), indicate wide plate boundary deformation and escape

tectonics occurring along an approximately 1400 km length of the North Andes, locking of the subducting Nazca plate (Fig. 13). Rapid subduction of the Nazca plate and of the Carnegie aseismic ridge (67 ± 6 mm/yr) at the Ecuador trench relative to the stable South America continent, are oblique to the Colombia-Ecuador margin - thus resulting in shortening perpendicular to the North Andean margin and in lateral "escape" (6 ± 2 mm/yr) to the northeast. The GPS data from northwestern South Ecuador and Colombia indicates a wide plate boundary deformation and strain accumulation along the Ecuador-Colombia fore-arc.

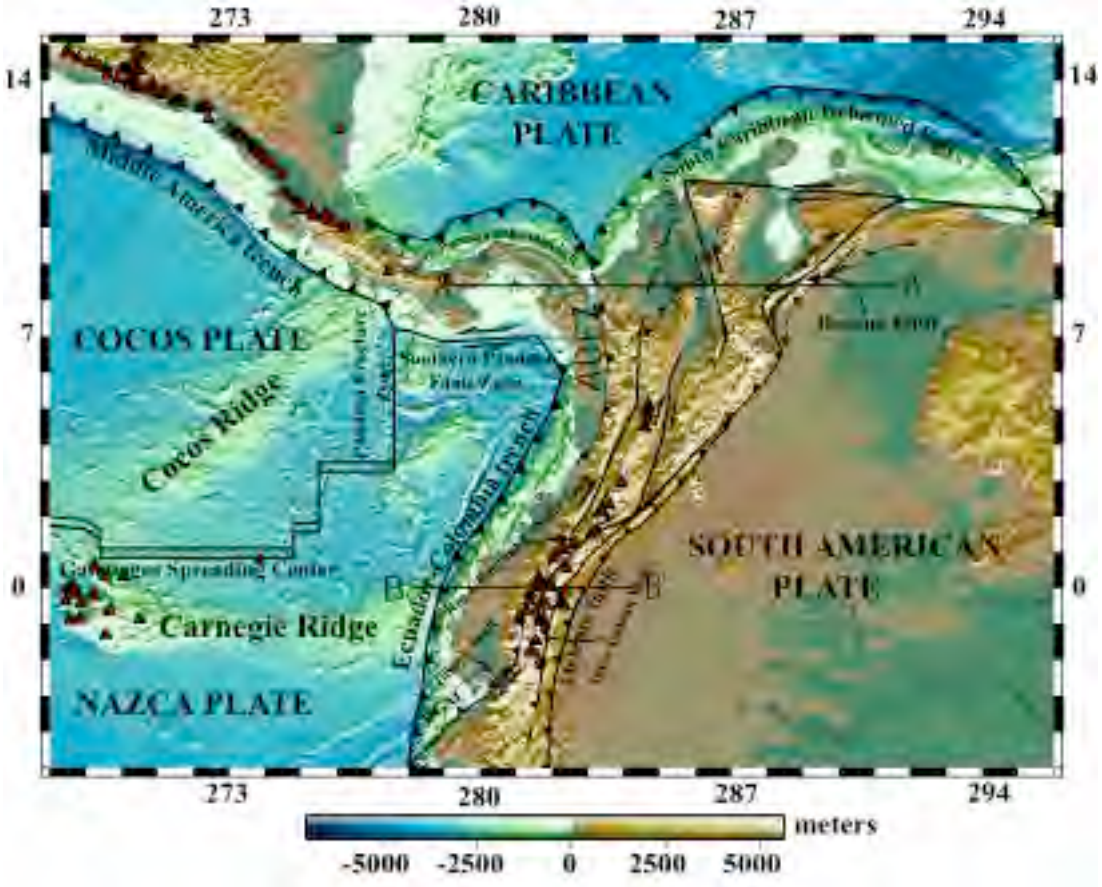

Figure 13. Major Tectonic Features along northwestern South America parallel to the convergence direction (after Trenkamp et al. 2002).

The same data indicates that elastic modeling of observed horizontal displacements in the Ecuador forearc is consistent with partial locking (50%) in the subduction zone and partial transfer of motion to the overriding South American plate. The deformation is assumed to reflect elastic recoverable strain accumulation associated with past seismicity of the area and active faulting associated with permanent shortening of 6 mm/a. (Trenkamp et al. 2002). Thus, substantial strain increase along the Ecuador-Colombia mega-thrust region since the 1979 earthquake will result in a major or great

tsunamigenic earthquake – perhaps in the near future. A major earthquake cold rupture a short segment similar to the 1942, 1958 and 1979 events, or a great earthquake will have a longer rupture and larger tsunami generation area, as that of 1906. It is also possible that the next earthquake along the Colombia-Ecuador margin will rupture a segment of the mega-thrust to the north of where the 1979 rupture terminated.

In summary, although the historical record is short and poorly documented for this tectonic regime of the Colombia-Ecuador margin, studies of earthquake potential using conditional probability estimates, had indicated a 66 percent probability for a major earthquake (M_s = 7.7) to take place along the subduction zone in the recurrence period of 1989-1999. However, no such earthquake occurred during this period, thus indicating that the probability of a major or great earthquake in this margin region has greatly increased. Furthermore, because the sequence of the three earthquakes that ended in 1979 did not release as much energy as the 1906 event, it has been suggested that an earthquake of similar magnitude to that of 1906 was likely in the near future.

Further evaluation of the amount of slip associated with the three subsequent events (1942, 1958 and 1979), suggests that they have released most of the accumulated displacement across the plate boundary since 1906. However, this is not consistent with the recent GPS data which indicates a wide plate boundary deformation and strain accumulation along the Ecuador-Colombia fore-arc. Thirty-three years have elapsed since 1979 without a major earthquake, thus there must be substantial strain accumulation in this region. Based on the 1948, 1952 and 1979 earthquakes, it can be concluded that a local destructive tsunami is likely to be generated in the near future from an earthquake with shorter length of rupture, while a local and Pacific-wide tsunami is likely to be generated if a greater earthquake strikes that has a rupture of 400 or more kms - as that of 1906. Also, south of the Carnegie subduction zone, there is potential for tsunamigenic earthquakes of lesser magnitude on faults of the southern region of the Guayaquil-Tumbes basin. Plate coupling along the subduction décollement, which controls the inward segmentation of deformation – as discussed earlier - could result in earthquakes and local tsunamis that would impact Southern Ecuador and the Gulf of Guayaquil.

3.5 Potential Impact of Future Tsunamis on Coastal Communities in Colombia and Ecuador

Given the observed strain accumulation along the Colombia/Ecuador subduction margin, there is high probability that a large tsunamigenic earthquake is going to occur in the same vicinity as that of 1906 and that it may have a similar long rupture and large tsunami generating area. A major tsunamigenic earthquake is also very possible along the Colombia/Ecuador mega-thrust. The tsunami that will be generated may be as great as that of 1906 and will be destructive – particularly if it occurs near high tide. Tumaco and coastal villages in southern Colombia and northern Ecuador are extremely vulnerable. For example, Tumaco is located on a coastal island sand bar with maximum elevation of 3 meters above sea level. If the tsunami is 5 meters high as in 1906 and occurs at high tide, the entire city will be completely inundated. Since the population density has greatly increased along coastal areas of Ecuador and Colombia, the death toll will be great. For example, the population of Tumaco in 1979 was about 80,000 people. Presently the population has increased to120,000.

REFERENCES

Collot, J.-Y., B. Marcaillou, F. Sage, F. Michaud, W. Agudelo, P. Charvis, D. Graindorge, M.-A. Gutscher, and G. Spence, 2004. Are rupture zone limits of great subduction earthquakes controlled by upper plate structures? Evidence from multichannel seismic reflection data acquired across the northern Ecuador–southwest Colombia margin, *J. Geophys. Res.*, *109*, 2004.

Gutscher, M.-A.; Malavieille J., Lallemand S. & Collot J.-Y., 1999. Tectonic segmentation of the North American margin: impact of the Carnegie Ridge collision. *Earth and Planetary Science Letters* **168**: 255–270.

Kanamori, H., and McNally, K.C., 1982, Variable rupture mode of the subduction zone along the Ecuador-Colombia coast: Bull. Seismol. Soc. Am., v. 72, p. 1241-1253.

Mendoza, C., 1986. Source mechanisms of Colombia aftershocks using digital surface-wave data. Bulletin of the Seismological Society of America December 1986 vol. 76 no. 6 1597-1613

Mendoza, C.; Dewey J.W., 1984. "Seismicity associated with the great Colombia-Ecuador earthquakes of 1942, 1958, and 1979: Implications for barrier models of earthquake rupture". *Bulletin of the Seismological Society of America* **74** (2): 577–593. Retrieved 2010-03-07.

Ortiz, M., Quiceno, A., and M. Fernandez-Arce, 2001. Regional and Far field effects of Colombian Tsunamis in the Pacific Ocean.

Pararas-Carayannis, G. 1980. The Earthquake and Tsunami of December 12, 1979, in Colombia. Intern. Tsunami Information Center Report, Abstracted article in Tsunami Newsletter, Vol. XIII, No. 1, January 1980. Also: http://www.drgeorgepc.com/Tsunami1979Colombia.html

Pararas-Carayannis, G., 2012. Geodynamics of Nazca Ridge's Oblique subduction and Migration - Implications for tsunami generation along Central and Southern Peru: Earthquake and Tsunami of 23 June 2001, Science of Tsunami Hazards, Vol.31, No. 2, 2012.

Pennington, W.D., 1981. Subduction of the eastern Panama basin and seismotectonics of northwestern South America: Journal of Geophysical Research, v. 86, p.10, 753-10,770.

Sallarès, V.; Charvis P., Flueh E.R., Bialas & the SALIERI Scientific Party, 2005. Seismic structure of the Carnegie ridge and the nature of the Galapagos hotspot. *Geophysical Journal International* 161: 763–788.

Sennson, L.J. and Beck, L.S., 1996. Historical 1942 Ecuador and 1942 Peru subduction earthquakes and earthquake cycles along Colombia-Ecuador and Peru subduction segments. Pure and Applied Geophysics. Vol . 146, Number 1 (1996), 67-101.

Trenkamp, R., Kellogg, J. N. Jeffrey T. Freymueller, Hector P. Mora', 2002. Wide plate margin deformation, southern Central America and northwestern South America, CASA GPS observations, Journal of South American Earth Sciences, Volume 15, Issue 2, June 2002, Pages 157-171.

White, S.M., Trenkamp, R., J. N. Kellogg, 2003. Recent crustal deformation and the earthquake cycle along Ecuador-Colombia subduction zone. Earthw and Planetary Science Letters 216, 231-242.

Witt C. & J. Bourgois, 2009. Forearc basin formation in the tectonic wake of a collision-driven, coastwise migrating crustal block: The example of the North Andean block and the extensional Gulf of Guayaquil-Tumbes Basin (Ecuador-Peru border area) Geological Society of America Bulletin, January 2010, v. 122, no. 1-2, p. 89-108.

ISSN 8755-6839

SCIENCE OF **TSUNAMI HAZARDS**

Journal of Tsunami Society International

Volume 31 **Number 3** **2012**

TSUNAMI SOCIETY INTERNATIONAL, 1741 Ala Moana Blvd. #70, Honolulu, HI 96815,USA.

WWW.TSUNAMISOCIETY.ORG